Coherent Control and Ground State Cooling of a Single $^{88}Sr^{+}$ Ion

Thesis submitted in partial fulfilment
of the requirements of the degree of
Doctor of Philosophy
of the
University of London

Valliappan Letchumanan

Imperial College London

Experimental work carried out at the
National Physical Laboratory

May 2004

Abstract

This thesis describes experiments using a single $^{88}Sr^{+}$ ion. The ion is confined in a radio-frequency end-cap trap and laser cooled on the strong 5s $^2S_{1/2}$ – 5p $^2P_{1/2}$ cooling transition. Spectroscopic investigations are performed on the narrow 5s $^2S_{1/2}$ – 4d $^2D_{5/2}$ quadrupole transition.

A precision measurement of the $^2D_{5/2}$ state lifetime has been made. The decay times of an ion prepared in the $^2D_{5/2}$ state are measured using Dehmelts electron shelving technique and analysed using several different fitting and estimation methods. A comparison of the these complementary techniques is made and systematic effects are discussed.

By driving the quadrupole transition, the electronic state of the ion has been coherently manipulated to create superpositions of the $^2S_{1/2}$ and $^2D_{5/2}$ states and Rabi oscillations observed. The rate of dephasing of these oscillations has been used to determine the mean motional quantum numbers of the Doppler cooled ion. High motional quantum numbers after Doppler cooling have been observed in the first endcap trap used. A second endcap trap has been constructed in which cooling to lower motional quantum numbers has been achieved.

Ramsey spectroscopy has been performed on a Zeeman component of the quadrupole transition. The first demonstration of Ramsey and Silsbee's phase modulation techniques in the optical domain is presented. With this method, increased signal to noise fringes and dispersion shaped curves have been observed and stabilisation of the laser to the transition demonstrated. To simulate these experiments, optical Bloch equations describing the Ram-

sey oscillatory field method have been set up and solved numerically.

Sub-Doppler cooling may be achieved by resolved-sideband cooling on the quadrupole transition. To realise an acceptable cooling rate, the $^2D_{5/2}$ state is quenched using a laser tuned close to the $^2P_{3/2}$ – $^2D_{5/2}$ transition. The resulting ac-Stark shift of the quadrupole transition has been characterised. Resolved-sideband cooling of the ion using the lower axial sideband of the $m_j = -1/2$ – $m_j = -5/2$ component of the quadrupole transition has been demonstrated.

Contents

Chapter 1

Introduction

The ion trap, when combined with laser cooling techniques, provides a most powerful experimental apparatus with which to conduct investigations of fundamental physics. A single trapped ion is well isolated from external perturbations and begins to approach the ideal of a particle held at rest. As such, it has long been recognised that a narrow transition in a trapped ion makes an ideal atomic frequency reference. A number of species are under investigation for this use in standards laboratories worldwide. In the last 10 years, it has been observed that these same properties make ion traps a highly attractive candidate experimental system for the realisation of a quantum computer. It is the aim of the work presented in this thesis to investigate techniques which will prove useful in both atomic frequency standards and quantum information processing work.

1.1 Atomic Frequency Standards

An atomic frequency standard consists of three main elements: a local oscillator, a quantum absorber and a servo system. The local oscillator provides short-term frequency stability and is stabilised by the servo system to a reference transition in a quantum absorber to provide long-term stability and reproducibility. The desire to construct stable atomic frequency standards is driven by their use in realising the S.I. units of length and time. Presently, the S.I. unit of time is defined in terms of 9.2 GHz microwave transition in ^{133}Cs. Accuracies of 1 part in 10^{15} are now achieved using laser-cooled caesium atoms in atomic fountains [1, 2, 3].

The stability of an atomic frequency standard, is dependent on the signal-to-noise ratio with which the reference transition is interrogated, the averaging time of the measurement and the Q-value of the reference transition. Using quantum absorbers with transitions of higher Q will therefore lead to a higher stability. The Q of caesium fountain systems is limited to $\sim 10^{10}$ by the maximum interrogation time available due to the time of flight of atoms in the fountain. In contrast, trapped ions may be stored for much longer periods. While microwave transitions in trapped ion systems may serve as reference quantum absorption, a number of narrow optical transitions in ions with intrinsic Q-values of greater than 10^{14} are far more attractive.

The accuracy of an atomic frequency standard is limited by how well externally induced shifts of the reference transition can be characterised. The velocity and spatial extent of single trapped ion may be reduced by laser-cooling so that Doppler broadening of a narrow reference transition is elimi-

nated. The external fields experienced by the ion may be also be controlled to a high order. By using a single trapped ion as the quantum absorber, the collisional shift present in standards using many quantum absorbers can be eliminated altogether. It is informative to note that collisional shifts are the largest source of uncertainty in caesium fountain standards [1, 4, 2, 3].

A laser-cooled single trapped ion closely approximates a particle held at rest, effectively indefinitely, in an environment almost free from external perturbations and as such makes an ideal reference quantum absorber in an atomic frequency standard. Currently being investigated as optical atomic frequency standards are narrow quadrupole transitions in $^{199}Hg^{+}$ [5], $^{88}Sr^{+}$ [6, 7], $^{171}Yb^{+}$ [8], an intercombination line in $^{115}In^{+}$ [9] and the extremely narrow octupole transition in $^{171}Yb^{+}$ [10]. Further details of trapped ion atomic frequency standards may be found in ref. [11] and references therein.

1.2 Quantum Information Processing

1.2.1 Background

In a quantum computer, information is encoded in the states of a *register* of two-level quantum mechanical systems known as quantum bits or *qubits*. Denoting the two pure states of a qubit by $|0\rangle$ and $|1\rangle$, each qubit may exist in a superposition of the form $\alpha|0\rangle + \beta|1\rangle$. This should be contrasted with a classical computer in which information is encoded in bits which may take only the values 0 and 1. Each qubit is, in some sense, able to store both logical values 0 and 1 at the same time. The information stored in

this quantum register may then be processed using unitary transformations which act upon both states $|0\rangle$ and $|1\rangle$ of each qubit simultaneously. By processing a superposition of many different input states in parallel, it might be possible for a quantum computer to carry out a calculation much more efficiently than a classical computer.

While the input state of such a quantum computer may be a superposition state, the final output state of the register which is then read out will be projected onto the basis set of states $|0\rangle$, $|1\rangle$ of the qubits. Since this projection process is probabilistic, any useful quantum computation must result in an interference of quantum amplitudes to produce a final answer which is composed of the pure states of the qubits. A number of such quantum information processing algorithms have been devised which are more efficient than any alternative classical algorithms known.

The Deutsch-Josza algorithm was the first efficient quantum information processing algorithm discovered and is capable of determining whether a function is constant (always outputs the same value, regardless of the input) or balanced (gives true for one of the two possible inputs and false for the other) with a single evaluation of the function. Other quantum algorithms of note are Shor's algorithm for factorising integers [12] and Grover's algorithm for searching unsorted databases [13], both of which are much more efficient than classical algorithms. Feynman has also pointed out that a quantum computer could be used to simulate any other quantum system [14], a task which also cannot be carried out efficiently by a classical computer.

1.2.2 Trapped ion quantum computing

With the theory of quantum information processing already well developed, there is a need for experimental work to determine whether such systems are physical realisable. The challenge of constructing a system that evolves unitarily and is also controllable is well described by DiVincenzo's criteria [15] which state the need for

1. A scalable physical system with well characterised qubits
2. The ability to initialise the register to a simple fiducal state, such as $|000\ldots\rangle$
3. Long relevant decoherence times, much longer than the gate operation time
4. A 'universal' set of quantum gates (from which any unitary operation may be constructed)
5. A qubit-specific measurement capability

There are many physical systems in which quantum mechanical phenomena are apparent and as such, it is not a surprise that there are a variety of candidate architectures have been proposed for the purpose of quantum information processing. These include trapped ions [16, 17, 18, 19], cold atoms [20, 21], linear optics [22], cavity quantum electrodynamics [23], liquid state NMR [24, 25], quantum dots [26], Josephson junctions [27] and the nuclear spins of dopants in silicon [28] to name but a few schemes.

Quantum information processing was first demonstrated experimentally using the NMR architecture. This technique uses the nuclear spins of atoms in a molecule as qubits. In order to prepare and measure such states, a bulk sample must be used, and the average state used. These states decohere and dephase slowly enough that the average state may be used as an effective quantum computer. The bulk nature of an NMR based approach to quantum information processing leads to limitted scalability and due to the fact that individual nuclear spins cannot be measured, greatly restricts the application of quantum error correction schemes which will be required in any useful quantum computer (see ref. [29] and references therein).

Cirac and Zoller have proposed that a quantum computer may be implemented using cold trapped ions [16]. In this implementation of a quantum computer, long-lived internal states of the ion act as the qubits and may be independantly manipulated using laser which can address the individual ions. Gates are implemented between (not necessarily neighbouring) ions by coupling through the collective quantized motional modes of the ions, which may also be excited using a laser. This method may be used to implement the controlled-NOT gate, and combined with single qubit rotations forms a set of universal gates [30]. A number of other gate implementations have also been proposed, such as Sørenson and Mølmer's gate employing virtual vibrational excitations [17] and the geometric phase gate described by Leibfried *et al.* [31].

1.2.3 Review of experimental progress

The realisation of Cirac and Zoller's scheme for an ion trap quantum computer requires ions cooled to the ground state of the trap. Ground state cooling of single trapped ions has been demonstrated with single $^{199}Hg^{+}$ [32], $^{40}Ca^{+}$ [33] and $^{115}In^{+}$ [34] ions and using resolved sideband cooling, $^{9}Be^{+}$ [35] ions using Raman sideband cooling and $^{40}Ca^{+}$ [36] by exploiting electromagnetically induced transparancy effects. Resolved sideband cooling of $^{88}Sr^{+}$ to the motional ground state is described in chapter 9.

After ground state cooling, single ions are in an almost pure motional state. This has allowed the quantum state engineering of both the ion's internal and external state [33] and the generation of non-classical states [37]. The first demonstration of a controlled-NOT gate operating on initialised states was also demonstrated using a single ion, using the ion's electronic state and motional state as the two qubits [38]. Entanglement of the internal and external states of an ion to produce 'Schrödinger cat' states has also been achieved [39]. More recently, a single $^{40}Ca^{+}$ ion has been used to implement the Deutsch-Josza algorithm [40]. Single ions have also been used to study decoherence of quantum superpositions in ion traps [41, 42].

Ground state cooling has been extended to two ions stored in linear traps in both $^{40}Ca^{+}$ [43] and $^{9}Be^{+}$ [44]. Following this feat, the Cirac and Zoller controlled-NOT gate has been demonstrated by F. Schmidt-Kaler *et al.* [45] using the internal states of two $^{40}Ca^{+}$ ions as the register of qubits and the collective motional degree of freedom as the 'bus' qubit. At around the same time, an alternative two-qubit universal gate was demonstrated by

Leibfreid *et al.* [31]. This work implemented a geometric phase gate in which the register of qubits was formed by the internal states of two $^{9}Be^{+}$ ions. The deterministic entanglement of two and four trapped ions has also been achieved [46].

1.3 Thesis structure

This thesis describes work carried out within the Fundamental and Wavelengths Standards group at the National Physical Laboratory, U.K. towards achieving the complete control of the quantum state of a single trapped $^{88}Sr^{+}$ ion. The $^{88}Sr^{+}$ ion has a strongly allowed transition suitable for efficient laser cooling, and a narrow transition which may be used as a frequency reference. The upper state of this narrow transition is long lived and combined with the ground electronic state may be used to form a long lived qubit. Readout of this qubit may also be carried out with almost unit detection efficience using Dehmelt's electron shelving method [47]. Thus $^{88}Sr^{+}$ is an ideal candidate for both optical atomic frequency standards and quantum information processing. The narrow quadrupole transition at 674 nm is already under investigation within the group as an optical atomic frequency standard. Indeed, this transition is already a recommended radiation for the realisation of the metre [48].

This thesis is organised a follows. Firstly, chapter 2 gives a brief theoretical background relevant to experiments using trapped ions. In particular, a model of coherent laser-ion interactions is outlined that includes the effects of the tight confinement of the ion, the laser phase and the decoherence

mechanisms of a finite laser coherence time and spontaneous emission.

Chapter 3 details the apparatus used for the work described in this thesis. During the course of this thesis, a number of improvements were made to the apparatus. This chapter describes the final set up after these improvements had been made. The basic experimental techniques for trapping and laser cooling a single ion are discussed in chapter 4.

Chapters 5 – 9 contain the main experimental results of this thesis. Chapter 5 presents a precession measurement of the lifetime of the metastable 4d $^2D_{5/2}$ state. Chapter 6 describes the coherent excitation of the quadrupole transition, resulting in the observation of high contrast Rabi oscillations. Chapter 7 presents time-domain Ramsey spectroscopy of the quadrupole transition and in particular, presents the first demonstration of Ramsey and Silsbee's phase modulation techniques in the optical domain. Chapter 8 describes the implementation of a scheme for frequency stabilisation of a laser to a narrow reference transition using Ramsey and Silsbee's phase modulation technique to provide the frequency discriminant. The final experimental chapter (Chapter 9) describes the resolved sideband cooling of one of the motional modes of a $^{88}Sr^+$ ion to its ground state.

Chapter 2

Theory

2.1 Introduction

The experiments described in this thesis employ a single $^{88}Sr^{+}$ ion confined in a radio-frequency trap. The ion is laser-cooled and its internal state interrogated and manipulated using lasers. This chapter gives an overview of the theory of radio-frequency traps and laser cooling and gives a description of the atom-laser interaction.

This chapter is organised as follows. First, Section 2.2 briefly describes the relevant energy levels of the $^{88}Sr^{+}$ ion. The principle of operation of the RF trap is then outlined in section 2.3. The time-averaged force exerted on the ion by the RF electric field of the trap results in a harmonic 'psuedopotential' in which the ion is confined. When the ion is laser-cooled, its kinetic energy may be reduced to the extent that its motion becomes quantised.

The interaction between a classical electromagnetic field and a bound two-level atom is described in section 2.4. The coherent oscillations in a

two-level atom driven by an intense field are discussed for the case of a free atom including both the effects of spontaneous emission from the atom's excited state and the finite coherence time of the driving field. When the ion is bound within dimensions small compared to the wavelength of the interrogating radiation (the Lamb-Dicke regime), its motion becomes quantised. The atomic (internal) states of the ion become dressed by the motional (external) states of the ion. The effect of the ion's motion on its absorption and emission spectra are discussed. The thermal distribution of the ion over the motional energy levels of the trap leads to an apparent dephasing of any coherent oscillations. This effect is also discussed.

The final section of this chapter deals with laser cooling of a $^{88}Sr^{+}$ ion. Doppler-cooling of an $^{88}Sr^{+}$ ion is described and typical Doppler cooling limits are calculated.

2.2 Energy levels of $^{88}Sr^{+}$

The $^{88}Sr^{+}$ ion has an alkali-like electronic structure, with ground state electronic configuration identical to that of neutral atomic rubidium ($1s^2 2s^2 2p^6 3s^2 3d^{10} 4s^2 4p^6 5s\ ^2S_{1/2}$). Figure 2.1 shows the lowest lying energy levels of the ion, with the wavelengths of the transitions used for laser-cooling, state manipulation and state detection. The ion has the convenient property that these transition wavelengths may all be produced by solid state laser sources. The lowest lying excited states are the $4d\ ^2D_{5/2}$ and $4d\ ^2D_{3/2}$ states. These states are metastable as they may only radiatively decay back to the $5s\ ^2S_{1/2}$ ground state via weak quadrupole transitions. The transition wavelengths

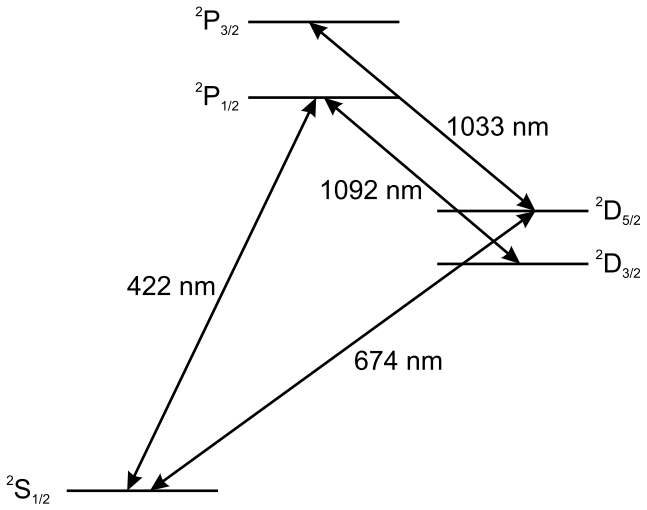

Figure 2.1: Lowest lying energy levels of $^{88}Sr^+$.

and decay rates and lifetimes for decay between the various electronic states are given in table 2.1.

The trapped ion is Doppler cooled (see section 2.5) on the 5s $^2S_{1/2}$ – 5p $^2P_{1/2}$ transition at 422 nm. The 5p $^2P_{1/2}$ state decays with a branching ratio of 1:13 to the metastable 4d $^2D_{3/2}$ state. Radiation at 1092 nm is therefore required to prevent optical pumping into this dark state and maintain efficient Doppler cooling.

Sub-Doppler cooling may be achieved by the technique of resolved sideband cooling (see chapter 9) on the narrow quadrupole transition at 674 nm. For resolved sideband cooling on the quadrupole transition, radiation at 1033 nm is used to 'quench' the $^2D_{5/2}$ state by coupling it to the $^2P_{3/2}$ state. Light at 1033 nm is also used to return an ion in the $^2D_{5/2}$ state to the electronic ground state.

Throughout this thesis, the $^2S_{1/2}$ – $^2P_{1/2}$ at 422 nm transition is referred to

Transition	Wavelength		$\Gamma/2\pi$	$\tau = 1/\Gamma$	
$^2S_{1/2} - {}^2P_{1/2}$	421.6706 nm	[49]	20.22 MHz	7.87 ns	[50]
$^2S_{1/2} - {}^2P_{3/2}$	407.886 nm	[49]	22.77 MHz	6.99 ns	[50]
$^2S_{1/2} - {}^2D_{3/2}$	687.0066 nm	[49]	0.37 Hz	435 ms	[50]
$^2S_{1/2} - {}^2D_{5/2}$	674.02559 nm	[48, 7, 6]	0.41 Hz	390.3 ms	†
$^2D_{3/2} - {}^2P_{1/2}$	1091.7860 nm	[49]	1.52 MHz	105 ns	[50]
$^2D_{3/2} - {}^2P_{3/2}$	1003.94 nm	[49]	176.6 kHz	901 ns	[50]
$^2D_{5/2} - {}^2P_{3/2}$	1033.01 nm	[49]	1.38 MHz	115 ns	[50]

Table 2.1: Wavelengths, decay rates and decay times of selected transitions in $^{88}Sr^+$. † Value determined in this work, see chapter 5

as the 'cooling' transition and the $^2D_{3/2} - {}^2P_{1/2}$ at 1092 nm transition as the 'repumper' transition. The $^2D_{5/2} - {}^2P_{3/2}$ transition at 1033 nm is referred to as both the 'quencher' transition in the context of resolved sideband cooling and the 'clearout' transition otherwise.

2.3 The RF trap

The radio-frequency (Paul) trap [51] grew out of work on linear quadrupole mass spectrometers [52]. In the RF trap, a dynamic trapping potential is created using oscillating electric fields. Such traps have been used to confine clouds of ions, and as is commonly the case now, single ions. The use of single ions has relaxed the requirement for a quadrupolar field of high purity over a large volume, as only the field at the point of the ion is important. As a result, rather than using the hyperbolic electrodes of the ideal Paul trap, other trap electrode structures [53, 54, 34, 55, 56], have be used for work employing single ions. Nevertheless, the basic principle of operation of the RF trap

remains the same in all these cases, with the time averaged electric field being used to produce a harmonic 'pseudopotential' suitable for confining an ion. A detailed overview of RF traps and the physics of trapped ions may be found in one of the many review articles on the subject [57, 58, 51].

A harmonic trapping potential is described by

$$\Phi = \Phi_0(\alpha x^2 + \beta y^2 + \gamma z^2) \tag{2.1}$$

where α, β and γ are constants. Laplace's equation, $\nabla\Phi^2 = 0$, requires that $\alpha + \beta + \gamma = 0$. It is therefore impossible to construct an electrostatic potential with constant Φ_0 which will trap an ion in all three dimensions simultaneously (Earnshaw Theorem), as this would require α, β and γ to all be negative. Instead, in an RF trap, a dynamic trap is formed by choosing

$$\Phi_0 = U + V cos(\omega_{\mathrm{RF}} t). \tag{2.2}$$

with α and β negative and γ positive. The potential Φ_0 alternates between being positive and negative, with the ion bound in the 'radial' xy-plane but unbound in the 'axial' z-direction for the one half of the RF cycle, and bound in the axial direction but unbound in the radial plane during the next half of the RF cycle. As the RF electric field is inhomogeneous, the time averaged force it exerts on the ion is not zero. The range of values of U, V and ω_{RF} for an ion of mass M, which produce a trapping potential which is both radially and axially stable may be determined by solving the equation of motion of the ion (a Mathieu equation) as outlined, for instance, by Leibfried *et al.* [31].

The regions of trap stability have also been mapped out experimentally [59].

An important result from the solution of the ion's equation of motion is that the ion's motion may be decomposed into a slow harmonic motion known as the secular motion and a driven motion at the RF trap frequency known as the micromotion. For an ion placed at the centre of the trapping potential, the micromotion typically has a much smaller amplitude than that of the secular motion. If the ion's micromotion is neglected, a fictional harmonic potential

$$q\Phi_p = \frac{1}{2}M(\omega_x^2 x^2 + \omega_y^2 y^2 + \omega_z^2 z^2) \tag{2.3}$$

commonly called the pseudopotential can be thought of as producing the ion's secular motion at frequencies ω_x, ω_y and ω_z in the x, y and z directions.

A laser-cooled atom may have its kinetic energy reduced to the extent that it is comparable with $\hbar\omega_x$, $\hbar\omega_y$ and $\hbar\omega_z$. Since the ion is bound in a harmonic potential, it may be described by the usual expressions for a quantum mechanical SHO, with the Hamiltonian

$$\hat{H}_{\text{trap}} = \hbar\omega_{\text{sec}}(\hat{a}^\dagger\hat{a} + \frac{1}{2}) \tag{2.4}$$

describing the ion motion along each of the axes of secular motion, where $\hat{a}^\dagger$ and $\hat{a}$ are the creation and destruction operators [60]. The ion's energy is therefore quantised according to

$$E_{\text{trap}} = \left(n + \frac{1}{2}\right)\hbar\omega_{\text{sec}} \tag{2.5}$$

where n is the vibrational quantum number of the ion.

2.4 Atom-field interactions

2.4.1 Coherent excitation of a two-level atom

If a two-level atomic transition is driven by radiation of sufficiently high coherence and intensity, coherent oscillations in the excited state population (Rabi oscillations) will be observed [60]. These oscillations will be damped due to the effects of spontaneous decay from the excited state and the finite coherence time of the driving radiation.

Consider a two level atom, with transition frequency ω_{atom} between the ground state $|S\rangle$ and excited state $|D\rangle$. The excited state decays to the ground state via spontaneous emission at the rate Γ_{SD}. The atom is driven by a laser of frequency ω_{laser} and linewidth Γ_{laser} with a pulse of duration τ and atom-laser coupling strength ω_0.

The density matrix for a two-level atom with ground state labelled S and upper state D is defined as

$$\hat{\rho} = \sum_{i,j} \rho_{ij} |i\rangle\langle j| \qquad \text{for } i,j \in \{S, D\} \tag{2.6}$$

or

$$\hat{\rho} = \begin{pmatrix} \rho_{SS} & \rho_{SD} \\ \rho_{DS} & \rho_{DD} \end{pmatrix} \tag{2.7}$$

in the matrix representation. The diagonal matrix elements $|\rho_{SS}|$ and $|\rho_{DD}|$ are the ground and excited state populations while the off diagonal elements ρ_{SD} and ρ_{DS} represent the coherence between the two states. The density matrix formalism allows the representation of both coherent states and sta-

tistical mixtures. The dynamics of the system are described by the master equation

$$\frac{\mathrm{d}}{\mathrm{d}t}\hat{\rho} = -\frac{i}{\hbar}[\hat{H}, \hat{\rho}] \tag{2.8}$$

where the Hamiltonian is split into two parts

$$\hat{H} = \hat{H}_{\mathrm{atom}} + \hat{V}(t) \tag{2.9}$$

the first representing the internal energy of the ion and the second representing the energy of interaction between the ion and the laser field. The matrix representation of the internal state Hamiltonian is simply

$$\hat{H}_{\mathrm{atom}} = \begin{pmatrix} E_S & 0 \\ 0 & E_D \end{pmatrix} \tag{2.10}$$

where the E_S and E_D are the energies of the ground and excited state and satisfy $\hbar\omega_{\mathrm{atom}} = E_D - E_S$. In general, the atom-field interaction energy in the dipole approximation is given by

$$\hat{V}(t) = \begin{pmatrix} 0 & \frac{1}{2}\Omega_0 \exp(i[\omega_{\mathrm{laser}}t + \phi]) \\ \frac{1}{2}\Omega_0 \exp(-i[\omega_{\mathrm{laser}}t + \phi]) & 0 \end{pmatrix} \tag{2.11}$$

where ϕ is the phase of the field and Ω_0 the laser-atom coupling strength.

The population decay due to spontaneous emission and the rate of dephasing of the coherences due to the finite laser linewidth are modelled phenomenologically as outlined, for example, by Boyd [61]. The decay of population from the $|D\rangle$ state to the $|S\rangle$ state due to spontaneous emission is

described by the following changes to the diagonal terms

$$\frac{\mathrm{d}}{\mathrm{d}t}\rho_{SS} = -\frac{i}{\hbar}[\hat{H},\hat{\rho}]_{SS} + \Gamma_{DS}\rho_{DD}, \quad (2.12)$$

$$\frac{\mathrm{d}}{\mathrm{d}t}\rho_{DD} = -\frac{i}{\hbar}[\hat{H},\hat{\rho}]_{DD} - \Gamma_{DS}\rho_{DD}, \quad (2.13)$$

where $[\hat{H},\hat{\rho}]_{ij}$ denotes the element of the matrix $[\hat{H},\hat{\rho}]$ having indices i,j . The decay of coherences due to the limited coherence of the laser is described by changes to the off diagonal terms

$$\frac{\mathrm{d}}{\mathrm{d}t}\rho_{SD} = -\frac{i}{\hbar}[\hat{H},\hat{\rho}]_{SD} + (\Gamma_{\mathrm{laser}} + \frac{1}{2}\Gamma_{DS})\rho_{SD}, \quad (2.14)$$

$$\frac{\mathrm{d}}{\mathrm{d}t}\rho_{DS} = -\frac{i}{\hbar}[\hat{H},\hat{\rho}]_{DS} - (\Gamma_{\mathrm{laser}} + \frac{1}{2}\Gamma_{DS})\rho_{DS}. \quad (2.15)$$

Incorporating the damping terms of equations 2.12 – 2.15 into the master equation 2.8 and making the substitution

$$\tilde{\rho}_{SD} = \exp(-i\omega_{\mathrm{laser}})\rho_{SD}, \quad (2.16)$$

$$\tilde{\rho}_{DS} = \exp(i\omega_{\mathrm{laser}})\rho_{DS} \quad (2.17)$$

gives the optical Bloch equations for the system:

$$\dot{\rho}_{DS} = \left[i(\omega_{\mathrm{laser}} - \omega_{\mathrm{atom}}) - (\Gamma_{\mathrm{laser}} + \tfrac{1}{2}\Gamma_{DS})\right]\tilde{\rho}_{DS} - i\tfrac{\Omega_0}{2}e^{-i\phi}\left(\rho_{DD} - \rho_{SS}\right) \quad (2.18)$$

$$(\dot{\rho}_{DD} - \dot{\rho}_{SS}) = -\Gamma_{DS}\left[1 + (\rho_{DD} - \rho_{SS})\right] + i\Omega_0\left(e^{-i\phi}\tilde{\rho}^*_{DS} - e^{i\phi}\tilde{\rho}_{DS}\right) \quad (2.19)$$

Solving equations 2.18 and 2.19 numerically over the period of the pulse

duration τ (subject to the boundary conditions $\rho_{SS} = 1$, $\rho_{DD} = 0$ at $t = 0$) describes Rabi oscillations of an atomic system driven by a single pulse of radiation.

The resulting Rabi oscillations in a free two-level atom are shown for different laser detunings $\delta = \omega_{\text{laser}} - \omega_{\text{atom}}$ and decoherence rates in figure 2.2 over a time scale much shorter than the lifetime of the upper state. As the detuning is increased, the amplitude of the Rabi oscillations decreases, and as the decoherence rate is increased, the oscillations decay more rapidly. With the laser field tuned to resonance, the coherent oscillations occur at the frequency Ω_0 known as the Rabi frequency.

2.4.2 The Lamb-Dicke Regime

The fact that the absorption and emission spectra of an atom are modified when the atom is bound was recognised as long ago as 1953 by Dicke [62]. The total Hamiltonian for a two-level atom in a 1-D harmonic potential interacting with a classical laser field is

$$\hat{H}_{total} = \hat{H}_{\text{atom}} + \hat{H}_{\text{trap}} + \hat{H}_{\text{laser}} \tag{2.20}$$

where $\hat{H}_{\text{atom}}$ and $\hat{H}_{\text{trap}}$ are defined by equations 2.4 and 2.10 and the energy of interaction between the atom and field is now given by [63, 64]

$$\hat{H}_{\text{laser}} = \frac{1}{2}\hbar\Omega_0(\hat{\sigma}^+ + \hat{\sigma}^-)(e^{i\eta(\hat{a}^\dagger + \hat{a})}e^{-i\omega_L t} + e^{-i\eta(\hat{a}^\dagger + \hat{a})}e^{i\omega_L t}). \tag{2.21}$$

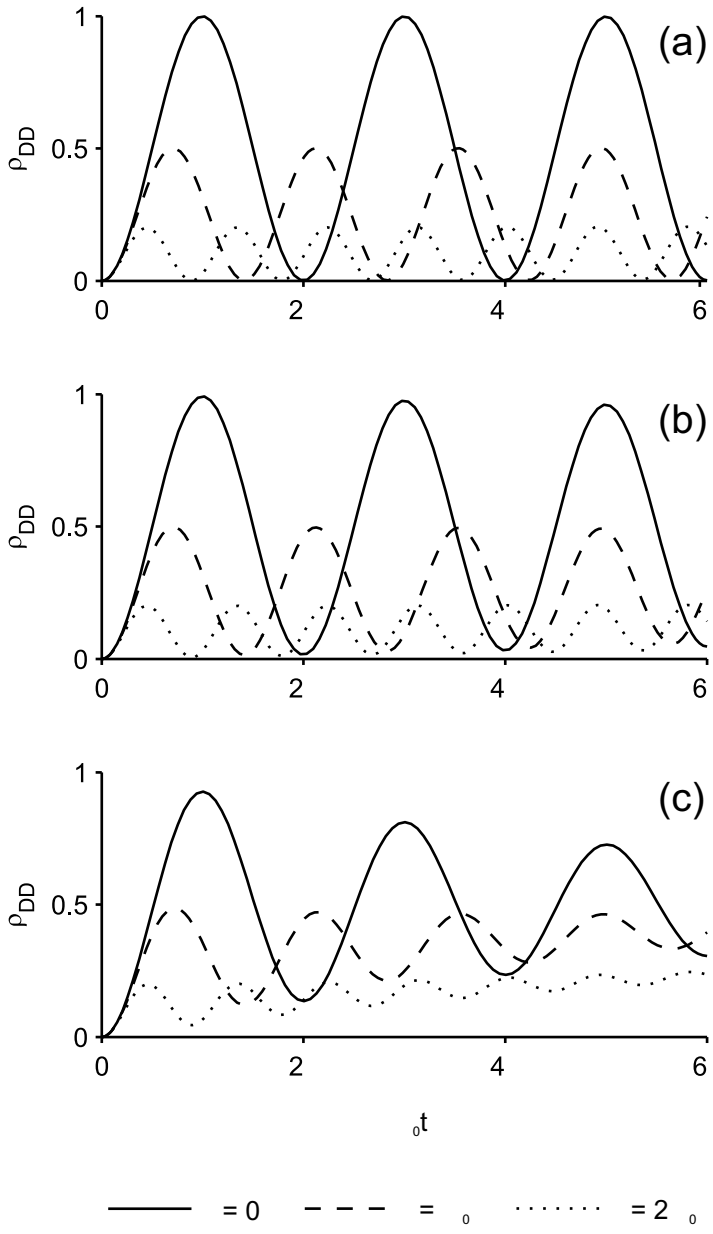

Figure 2.2: Rabi oscillations in a two-level atom driven by a field with coupling strength Ω_0 given by numerically integrating equations 2.18 and 2.19. Figure (a) shows the time evolution of the excited state population for the case of no decoherence or spontaneous emission with the field tuned to resonance (solid line) and detunings of $\delta = \Omega_0$ (dashed line) and $\delta = 2\Omega_0$ (dotted line). Figures (b) and (c) show the oscillations expected when the decoherence rate is increased to $\Gamma_{\text{laser}} = \Omega_0/100$ and $\Gamma_{\text{laser}} = \Omega_0/100$ respectively.

The terms $\hat{\sigma}^+$ and $\hat{\sigma}^-$ are the Pauli matrices, Ω_0 is the laser-ion coupling strength (or Rabi frequency) and η is the Lamb-Dicke parameter. The Lamb-Dicke parameter for a bound atom interacting with light of wavevector k making an angle θ with the atom's motional mode is defined as

$$\eta = k\cos\theta x_0 = \frac{2\pi}{\lambda}\cos\theta\sqrt{\frac{\hbar}{2M\omega_{\text{sec}}}}. \tag{2.22}$$

The Lamb-Dicke parameter is therefore a measure of $x_0 = \sqrt{\hbar/2M\omega_{\text{sec}}}$ the spatial extent of motional ground state wavefunction of the ion in terms of the wavelength of the laser light λ. A further insight into the meaning of the Lamb-Dicke parameter may be gained by noting that η^2 is simply the recoil energy of the ion when absorbing a photon $\hbar^2k^2/2M$ in terms of the energy associated with one vibrational quantum of energy $\hbar\omega_{\text{sec}}$.

The total Hamiltonian has been solved by making the rotating wave approximation and working in the interaction picture, see for instance [63, 64]. The solution to the total Hamiltonian predicts that the transition between the ion's internal states at ω_{atom} is dressed by the ladder of harmonic oscillator levels separated by ω_{sec}. The resulting spectrum therefore consists of a carrier transition at ω_{atom} with sidebands at $\omega_{\text{atom}} \pm m\omega_{\text{sec}}$ (see figure 2.3). Driving the ion on the carrier transition, will result in a change of internal state without affecting the motional state of the ion. However, driving the ion on the mth blue (red) sideband will result in an increase (decrease) of the ion's motional quantum number by m vibrational quanta. The laser-ion coupling strength is dependant on the ion's motional quantum number. For a resonant transition between the n'th and nth motional states the laser-ion

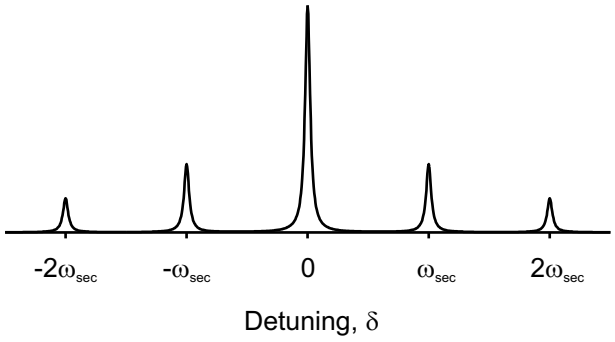

Figure 2.3: The absorption and emission spectra of a bound atom consist of a carrier and sidebands spaced by the secular frequency.

coupling on the mth sideband (where $m = n' - n$) is given by [63, 64]

$$\Omega_{n',n} = \Omega_0 e^{-\eta^2/2} \sqrt{\frac{n_<!}{n_>!}} \eta^{|m|} L_{n_<}^{|m|}(\eta^2) \tag{2.23}$$

where $n_>$ ($n_<$) is the larger (smaller) of n' and n and L_n^m the generalised Laguerre polynomial [65]

$$L_n^m(x) = \sum_{k=0}^{n} (-1)^k \frac{(n+m)!}{(n-k)!(m+k)!k!} x^k. \tag{2.24}$$

In the Lamb-Dicke regime, the the amplitude of the ions motion in the direction of the radiation is much less than $\lambda/2\pi$. When this is the case, the laser-ion coupling strengths to second and higher order sidebands are negligible and only transitions on the carrier and first lower (red) and first upper (blue) sidebands are important. These processes are shown in figure 2.4. It should be noted that while absorbtion on the red sideband reduces the ion's motional quantum number by one vibrational quantum or phonon, emission on the red sideband increases it by one phonon. Similarly, emission on

the blue sideband also reduces the ion's motional quantum number by one phonon.

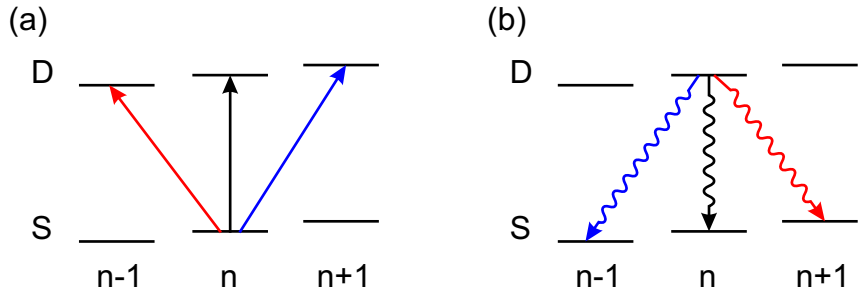

Figure 2.4: Absorption on the red sideband, carrier and blue sideband are shown in (a) and emission is shown in (b). Transitions on the red and blue sidebands result in a change in the ion's vibrational quantum number. In the Lamb-Dicke regime transitions on higher order sidebands may be neglected.

In the Lamb-Dicke limit, the coupling strength on the carrier given by equation 2.23 may be simplified to second order in η to give

$$\Omega_{n,n} = \Omega_0 \left[1 - \left(n + \frac{1}{2}\right)\eta^2\right]. \tag{2.25}$$

Similarly, the coupling strengths to first order in η on the red and blue sideband are

$$\Omega_{n,n-1} = \eta\sqrt{n}\Omega_0 \tag{2.26}$$

and

$$\Omega_{n,n+1} = \eta\sqrt{n+1}\Omega_0 \tag{2.27}$$

respectively.

Exciting the atom on the red sideband will reduce the motional quantum number by one quantum, however for an atom in the ground state of the

trap, no lower energy motional states exist. As a consequence, the coupling strength on the red sideband tends to zero as the atom's motional quantum number is reduced to zero (see equation 2.26).

2.4.3 Coherent excitation of a bound two-level atom

Describing the coherent excitation of an bound atom is complicated by the fact that the coupling strength of the laser-atom interaction is dependent on the atom's motional state as described in section 2.4.2. For example, Rabi oscillations observed in a bound atom will exhibit an apparent damping which is dependent on the atom's distribution over motional states of the trap. This section outlines a model of a trapped two-level ion with finite excited state lifetime interacting with a near-resonant laser of limited coherence.

A Doppler-cooled trapped ion may occupy any one of a number of vibrational energy states $|n\rangle$ of the trap. The probability of finding the ion in a particular vibrational state of the trap is given by thermal distribution

$$P_n(\bar{n}) = \frac{\bar{n}^n}{(1+\bar{n})^{1+n}} \tag{2.28}$$

where $\bar{n}$ is the average vibrational quantum number.

The coherent excitation of a Doppler-cooled trapped ion with mean vibrational quantum number $\bar{n}$ may therefore be modelled as follows. The optical Bloch equations 2.18 and 2.19 for each vibrational state, given by replacing the total atom-laser coupling strength Ω_0 in these equations with the n-dependent atom-laser coupling of $\Omega_{n',n}$ given by equation 2.23 must first be solved. These solutions are then summed with a weight given by the

occupation probability of the motional state (see equation 2.28). Since each of the motional states has a different Rabi frequency $\Omega_{n',n}$, the contributions from each state cause the observed oscillations to wash out. This is illustrated for the case of coherent excitation of the carrier transition resulting shown in figure 2.5.

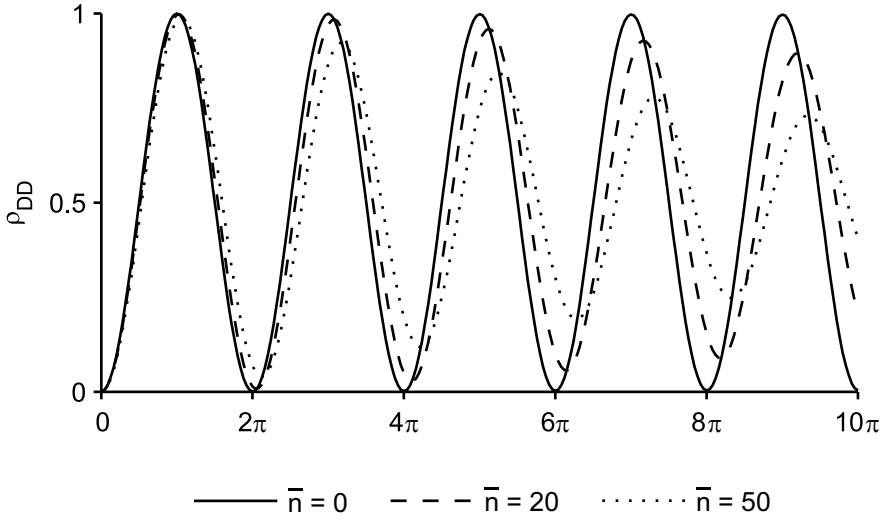

Figure 2.5: Rabi oscillations in a two-level atom bound in a 1-D harmonic potential with mean vibrational occupation number $\bar{n} = 0$ (solid line), $\bar{n} = 20$ (dashed line) and $\bar{n} = 50$ (dotted line) and driven by a resonant monochromatic field. As the atom-laser coupling strength is a function of the vibrational state of the atom, the time evolution of the excited state population is calculated by solving equations 2.18 and 2.19 for each vibrational state and summing the solutions according to the occupation probability each state. The oscillations 'wash out' since each vibrational state has a different Rabi frequency.

2.5 Doppler cooling

In order to fulfil the Lamb-Dicke criterion, the trapped ion must be prepared with a small mean vibrational quantum number. This is equivalent to saying

that the ion must be cooled to a low temperature. This feat may be achieved by using laser cooling techniques.

Laser cooling was first proposed by Hänsch and Schawlow [66] for free atoms and independently by Wineland and Dehmelt [67] for bound atoms in 1975 and has since become a common tool in atomic physics.

Doppler cooling may be understood as follows. For a two level atom, with an atomic resonance at ω, absorption of light detuned by δ below the transition is favoured when the atom is moving towards rather than away from the light source, due to the Doppler effect. The absorption of a photon results in a reduction of the ions momentum by $\hbar k = \hbar(\omega - \delta)/c$. The dipole pattern of the subsequent spontaneous emission process is spatially symmetric and on average causes no net increase in the atom's momentum. Over a number of emission/absorption cycles, the ion's velocity towards the light source is reduced, leading to cooling.

The discrete nature of the emission/absorption process imposes a limit to the final temperature realisable by this method. On each spontaneous emission the ion receives a momentum kick of $\hbar k$ in a random direction. The minimum achievable energy is calculated by considering the ion to be performing a random walk in momentum space due to the recoil from spontaneous emission In the weak binding limit where the secular frequency of the ion is much smaller than linewidth of the atomic transition ($\omega_{\text{sec}} \ll \Gamma$), the lowest temperature attainable per motional degree of freedom is [68]

$$kT_{\text{min}} = \hbar\Gamma/2 \tag{2.29}$$

occurring at a detuning of $\delta = -\Gamma/2$. Equation 2.29 is known as the Doppler limit. Equating this minimum energy to the ion's average kinetic energy $(\bar{n} + 1/2)\hbar\omega_{\text{sec}}$ yields [69]

$$\bar{n}_{\text{min}} = \frac{1}{2}\left(\frac{\Gamma}{\omega_{\text{sec}}} - 1\right) \tag{2.30}$$

as the mean vibrational quantum number at the Doppler limit.

In $^{88}Sr^{+}$, the most suitable transition for Doppler cooling is the $^{2}S_{1/2}$ – $^{2}P_{1/2}$ dipole transition at 422 nm which has a linewidth $\Gamma = 20.2$ MHz [49]. The ion may be cooled by a single laser beam with components along all three trap axes. The Doppler limit for typical axial and radial secular frequencies of 3.8 MHz and 2.2 MHz expressed in terms of axial and radial mean vibrational quantum numbers is $\bar{n}_r = 4.3$ and $\bar{n}_z = 2.1$.

Chapter 3

Experimental Setup

3.1 Introduction

This chapter describes the apparatus used to trap and laser cool a single $^{88}Sr^{+}$ ion and probe and manipulate it on the weak $^{2}S_{1/2}$ – $^{2}D_{5/2}$ quadrupole transition (see figure 2.1). The ion is confined in a radio-frequency endcap trap and Doppler-cooled on the $^{2}S_{1/2}$ – $^{2}P_{1/2}$ transition at 422 nm. The $^{2}P_{1/2}$ state decays with a branching ratio of 1:13 to the metastable $^{2}D_{3/2}$ state. Radiation at 1092 nm is therefore required to prevent optical pumping into this dark state and maintain efficient Doppler cooling. Spectroscopic investigations of the narrow quadrupole transition are conducted using a laser at 674 nm. If the ion is excited to the metastable $^{2}D_{5/2}$ state, it may be returned to the electronic ground state using the quencher a laser at 1033 nm. For resolved sideband cooling on the quadrupole transition (see chapter 9), this laser is also used to 'quench' the $^{2}D_{5/2}$ state by coupling it to the $^{2}P_{3/2}$ state.

This chapter is organised as follows. The geometry and main design features of the two endcap trap used in this thesis are detailed in Section 3.2, as are different atomic strontium sources used to load the traps. The trap drive system is described in section 3.3. In section 3.4, the arrangement of the various laser beams required for laser cooling, optical pumping, driving the quadrupole transition and returning the ion to the electronic ground sate is given, followed by the setup used for fluorescence detection on the cooling transition. Sections 3.6 –3.9 describe the 'cooling' laser at 422 nm, the 'repumper' laser at 1092 nm, the 'probe' laser at 674 nm the 'quencher/clearout' laser at 1033 nm. Finally, the setup used for data acquisition and control of the experiment is described in section 3.10.

3.2 The endcap trap

An endcap trap [70] consists of two sets of coaxially arranged electrodes as shown in fig. 3.1. A radio-frequency trapping voltage is applied to the upper and lower inner endcaps while the concentric outer endcaps are grounded (or held at small DC potentials to compensate for stray electric fields). Although this electrode structure departs significantly from the hyperbolic electrode shape of the ideal Paul trap [51], the endcap trap still yields a highly harmonic trapping potential at the position of the ion. In addition, the removal of the ring electrode allows for much improved optical access in the xy-plane.

Two different ion traps, both of the endcap design and constructed by A.G. Sinclair, have been used during the course of this work. The first trap was used only for the measurement of the 4d $^2D_{5/2}$ state lifetime and

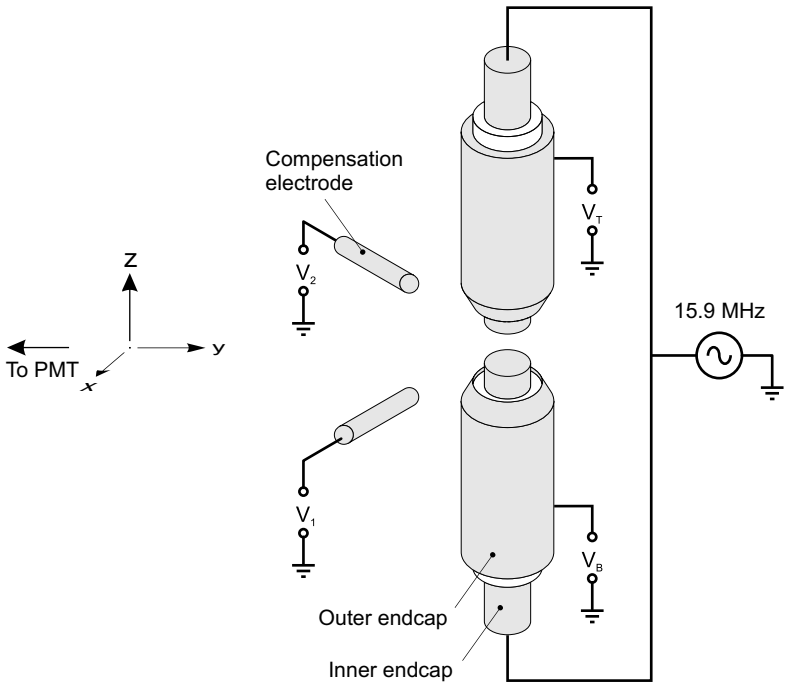

Figure 3.1: Experimental arrangement of the endcap trap

initial investigations of coherent excitation of the quadrupole transition (see chapters 5 and 6), and was replaced by the second, more recently constructed trap, before the work described in the remainder of this thesis.

3.2.1 Trap 1

Trap 1 was identical in design geometry to that constructed by Schrama *et al.* [70]. The inner endcap electrodes were 0.5 mm in diameter and separated by 0.56 mm. The outer electrodes had inner diameter of 1 mm and outer diameter of 2 mm. The inner and outer electrodes were constructed of tantalum and separated by an alumina spacer.

DC potentials could be applied to each outer endcap independently. Ap-

plying a common potential to both outer endcap electrodes allows the sphericity of the trapping potential to be varied while a potential difference across between the electrodes is used to null stray electric fields along the z-axis. A further two compensation electrodes in the xy-plane were used to null the other components of any stray electric fields.

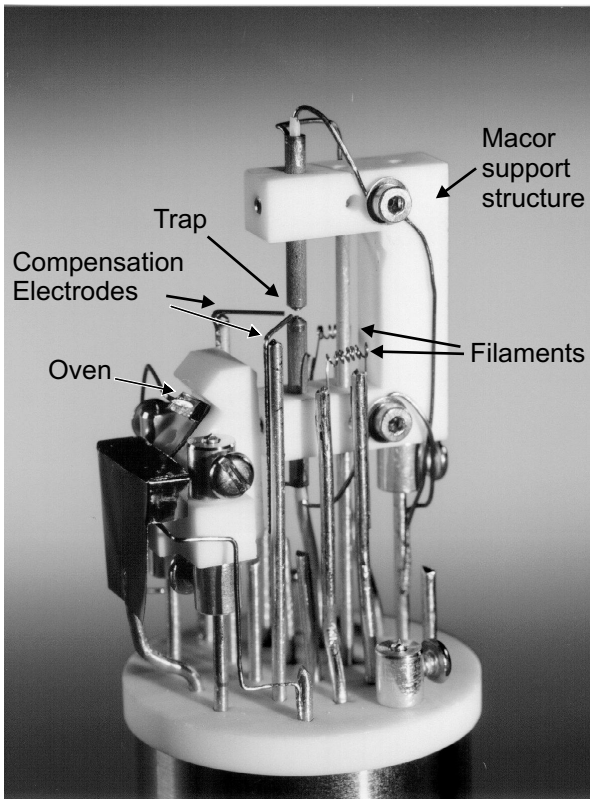

Figure 3.2: Photograph of endcap trap 1.

Strontium ions for loading the trap were produced by ionising atomic strontium with electrons from a tungsten filament. Since free strontium reacts quickly under atmosphere, atomic strontium is produced in the vacuum

chamber by the following chemical reaction

$$SrAl_4 + Ni \rightarrow Sr + \ldots$$

in an oven heated to 800°C. This oven was pointed upwards towards the centre of the trap (see fig 3.2).

3.2.2 Trap 2

Trap 2 is again identical in geometry to that constructed by Schrama *et al.* [70], with inner endcap electrodes of 0.5 mm diameter, separated by 0.56 mm and outer electrodes of 1 mm inner diameter and 2 mm outer diameter. The inner and outer electrodes are constructed of tantalum and are separated by an alumina spacer.

More care has been taken with this trap design to minimise any phase difference between the trapping voltage at the upper and lower inner endcap electrodes, which would lead to heating of the ion [71]. This has been done by ensuring that the RF trapping potential is delivered to the trap via two symmetric arms (see fig 3.3). These arms are also shielded to reduce the amount of RF radiation broadcast by the trap.

The $SrAl_4$:Ni oven used to load Trap 1 is likely to deposit aluminium and nickel as well as strontium onto the electrode structure. Such impurities lead to patch potentials developing on the electrodes and spoiling the quadrupolar trapping field. This is thought to be a major cause of heating in RF traps. R.G. DeVoe *et al.* have observed in experiments using $^{137}Ba^+$ trapped in RF microtraps, that the use of a $BaAl_4$:Ni oven led to unstable trap operation

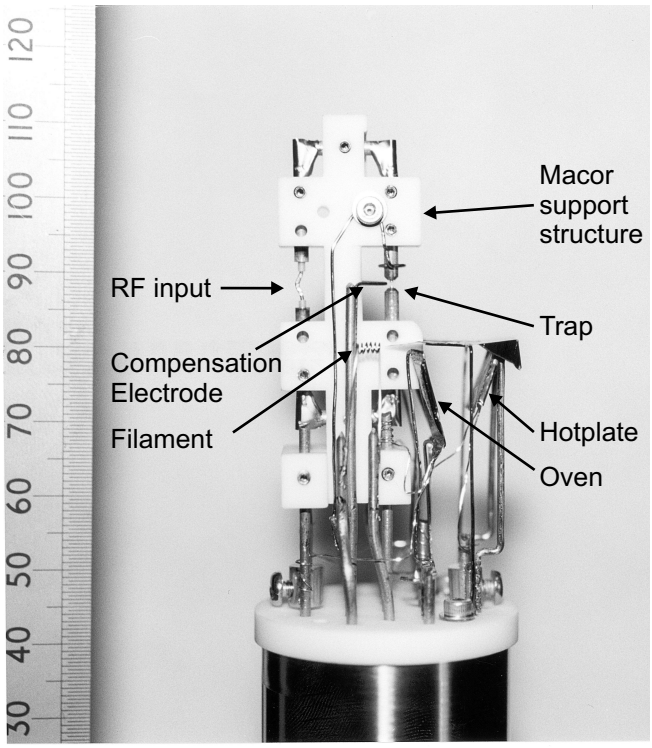

Figure 3.3: Photograph of endcap trap 2.

over the course of a number of loads. This was observed as large variation in the compensation voltages required to minimise micromotion. This type of behaviour had been obseverved during the final six months of operation of trap 1 (see section 6.2.1).

DeVoe *et al.* also demonstrated that onset of trap instability could be avoided by using a two stage oven: in the first stage, a mixture of barium oxide and tantalum powder is heated to 1200 °C to produce free barium:

$$\mathrm{BrO} + \mathrm{Ta} \rightarrow \mathrm{Br} + \ldots$$

which is deposited on a hot plate. As the oven containing the BrO:Ta mixture has no line-of-sight to the trap, impurities produced by this process are unable to coat the electrodes. The hot plate is then heated to produce barium with which to load the trap. In adition, at the lower temperatures required to free barium from the hotplate, tantalum has a very low vapour pressure.

In order to load Trap 2, a process analogous to that used by DeVoe *et al.* is used. An SrO:Ta mix oven is prepared from an oven containing a $SrCO_3$:Ta mix by heating to 1000°C for 24 hours. During this time the $SrCO_3$ evolves CO_2 gas, leaving behind only SrO. This process is completed with the vacuum chamber connected to a turbo pump, before the chamber is baked and pumped down to UHV conditions.

The first stage in loading the trap is to heat the ovens to 1200 °C so that the reaction:

$$\mathrm{SrO} + \mathrm{Ta} \rightarrow \mathrm{Sr} + \ldots$$

takes place, depositing strontium on the hot plate. The hot plate is then

heated to ∼400 °C to produce atomic strontium to load the trap.

3.3 Trap drives

3.3.1 Self-oscillating transitor circuit

In early work the trap drive voltage was produced by an self-oscillating transistor circuit. This circuit (shown in fig 3.4) was able to produce 350 V amplitude drive voltage at a frequency of 13.2 MHz. A limitation of this type of drive system is its poor spectral purity: output at the second harmonic of the drive frequency was only ∼20 dB below that of the fundamental. This trap drive was replaced in September, 2002 by a helical coil resonator system of higher spectral purity (see section 3.3.2).

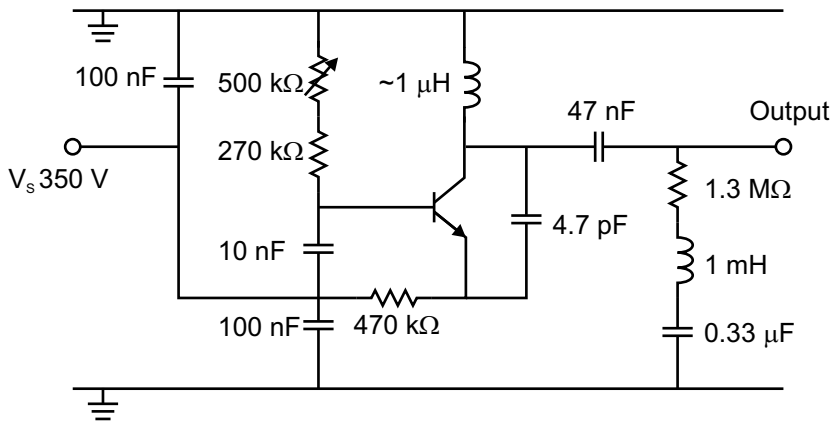

Figure 3.4: Self-oscillating transistor circuit trap drive.

3.3.2 Helical coil resonator

In this drive, the RF trapping potential is produced using a helical resonator [72] (see figure 3.5) driven by 1.5 – 4 W input power at 15.9 MHz. The resonator shield is constructed from copper and the helical inner conductor from 2 mm diameter copper plated wire. The resonator shield is 100 mm in diameter and 140 mm in length. The input coil is of 2–3 turns of 20–30 mm diameter, adjusted for the purpose of impedance matching to the RF source. The output coil consists of 10 turns of 52 mm diameter. The unloaded Q of the resonator is 500 at a frequency of 43.4 MHz. When connected to the trap, the loaded Q is $\sim$90 at 15.9 MHz. The resonator is driven by a Marconi 2019A RF synthesiser and Wessex RC601-5 5 W amplifier. A directional coupler is used to couple out the reflected signal from the resonator. The synthesiser is tuned to the resonator by minimising the reflected power.

The high Q of the helical coil resonator gives a trap drive of high spectral purity, with output at the second harmonic 70 dB below that at the fundamental drive frequency.

3.4 Vacuum chamber, beam paths and fluorescence detection

The trap is mounted in a stainless steel vacuum chamber 250 mm long and 150 mm in diammeter which is pumped down to around 10^{-10} Torr by a Varian triode pump and SAES non-evaporable getter pump. The entire trap apparatus is constructed directly onto a 20 pin UHV feedthrough, through

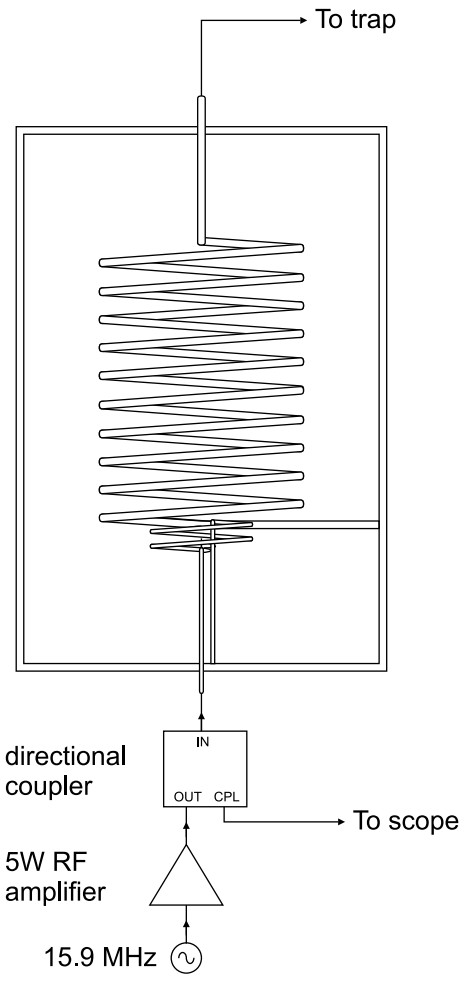

Figure 3.5: Helical resonator trap drive.

which all the DC electrical connections are made (to the compensation electrodes, ovens, filaments and hotplate). In the setup for trap 1, the connection from the RF trap drive to the inner endcaps was also made on this feedthrough, however with the construction of trap 2, the RF trap drive potential enters the vacuum chamber on a separate coaxial feedthrough.

The ion is Doppler cooled on the cooling transition at 422 nm. The ion may be optically pumped into one of the Zeeman sub-levels of the 5s $^2S_{1/2}$ state using circularly polarised light at 422 nm. Light from a repumper laser at 1092 nm is required to prevent optical pumping of the ion into the $^2D_{3/2}$ state. The narrow quadrupole transition is driven by a laser at 674 nm for spectroscopic investigations and resolved sideband cooling. A laser at 1033 nm may be used to quench or broaden the $^2D_{5/2}$ state by mixing it with the $^2P_{3/2}$ state. This laser is also be used as a clearout laser, to return the ion from the $^2D_{5/2}$ state to the electronic ground state.

Three different Doppler cooling beams enter the chamber through angled, AR coated windows and exit via Brewster windows. The cooling beam directions are along unit vectors $-0.87\hat{x} - 0.47\hat{y} - 0.13\hat{z}$ (cooling beam 1), $0.87\hat{x} - 0.34\hat{y} + 0.34\hat{z}$ (cooling beam 2), and $-0.87\hat{x} + 0.13\hat{y} + 0.47\hat{z}$ (cooling beam 3) as shown in figure 3.6. A pair of ports allows access for the optical pumping beam and clearout beam along the x-direction and a further pair are used for two counter-propagating probe beams along $0.87\hat{x} + 0.5\hat{z}$. The repumper makes two passes through the trap entering along cooling beam 1 and then being redirected along cooling beam 2. The quencher beam enters the chamber anti-parallel to cooling beam 3. Table 3.1 summarises the wavelengths and directions of all beams.

Beam	Wavelength	Unit Vector
Cooling beam 1	422 nm	$-0.87\hat{x} - 0.47\hat{y} - 0.13\hat{z}$
Cooling beam 2	422 nm	$0.87\hat{x} - 0.34\hat{y} + 0.34\hat{z}$
Cooling beam 3	422 nm	$-0.87\hat{x} + 0.13\hat{y} + 0.47\hat{z}$
Optical pumping beam	422 nm	$\hat{x}$
Repumper beam 1	1092 nm	$-0.87\hat{x} - 0.47\hat{y} - 0.13\hat{z}$
Repumper beam 2	1092 nm	$0.87\hat{x} - 0.34\hat{y} + 0.34\hat{z}$
Weak probe beam	674 nm	$0.87\hat{x} + 0.48\hat{z}$
Intense probe beam	674 nm	$-0.87\hat{x} - 0.48\hat{z}$
Quencher beam	1033 nm	$0.87\hat{x} - 0.13\hat{y} - 0.47\hat{z}$
Clearout beam	1033 nm	$\hat{x}$

Table 3.1: Beam wavelengths and unit vectors

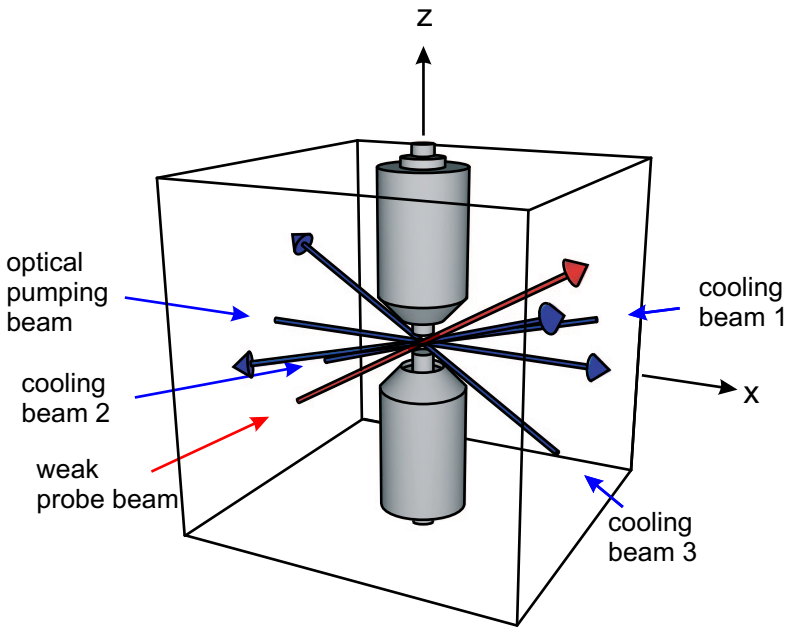

Figure 3.6: Beam paths of cooling beams 1, 2 and 3, optical pumping beam and weak probe beam. The repumper, intense probe, quencher and clearout beams are omitted for clarity.

To maximise the solid angle for fluorescence detection of 422 nm photons scattered on the cooling transition, one face of the vacuum chamber has a 15 cm re-entrant window. An f/1.05 multi-element lens with magnification of 10 is used to image the ion through a 200 μm pinhole onto an Electron Tubes 9893/350A photo-multiplier tube (PMT). The pinhole is necessary to reduce the amount of scattered light from the trap electrodes imaged onto the PMT. A filter is also placed between the pinhole and PMT to reduce its sensitivity to light at 674 nm, 1033 nm and 1092 nm which may also be incident on the ion and scattered by the trap electrodes. The PMT is biased at 1600 V, has a dark count of $\sim$10 count/s per second and quantum efficiency of 22% at 422 nm. Fluorescence count rates of $\sim 2 \times 10^4$ counts/s are observed with the cooling laser tuned to half a linewidth below line centre of the cooling transition compared to background count rates of 300–1600 count/s depending on which cooling beam or combination of cooling beams is used.

3.5 Magnetic field coils

Magnetic fields of up to 4.5 G may be applied to the ion using three pairs of mutually orthogonal field coils. The magnetic field coils oriented along the x- and y-axes each have 80 turns on square formers with 500 mm sides and each placed 250 mm from the trap. The magnetic field coils along the z direction have 170 turns each, wound on circular formers of 140 mm diameter, each approximately 150 mm from the centre of the trap.

The field coils along the y- and z-axes are used solely to null the ambient magnetic field, while the x-axis field coils is also used to apply a magnetic

bias field to the ion. The x-axis field coils produce a magnetic field of 1.44 G per ampere of applied current at the centre of the trap.

3.6 Cooling laser

Light at 422 nm for Doppler cooling the ion is generated by a frequency doubled 844 nm extended cavity diode laser (ECDL). The diode laser (SDL-5422-H1) is arranged with collimating lens and grating in the Littrow configuration and housed in a temperature controlled, air-tight enclosure (see fig 3.7), with a typical output power of 45 mW. The laser is stabilised to a tunable reference cavity (finesse $\mathcal{F} = 115$) by locking to the side of a transmission fringe. The cavity fringe photodiode signal (PD1) is divided by an intensity reference photodiode signal (PD2) using an Analog Devices AD534 analogue divider IC to produce a intensity independent discriminant to be used as an error signal. The laser is stabilised through feedback to two elements: the diode drive current and the piezo-electric transducer controlling the extended cavity grating angle (PZT1). A double integrator circuit in a 'bypass' topology [73] is used to feed back to the laser diode drive current, while the output of this servo is passed through a second integrator stage to provide feedback to PZT1. Fig. 3.8 shows the reduction in noise of the error signal when the laser is stabilised to the reference cavity. The laser is tuned by varying the reference cavity length with a second piezo-electric transducer (PZT2).

The 844 nm ECDL output is doubled using $KNbO_3$ in a bow-tie enhancement cavity (see fig 3.7). The $KNbO_3$ crystal is cooled to -17 °C to

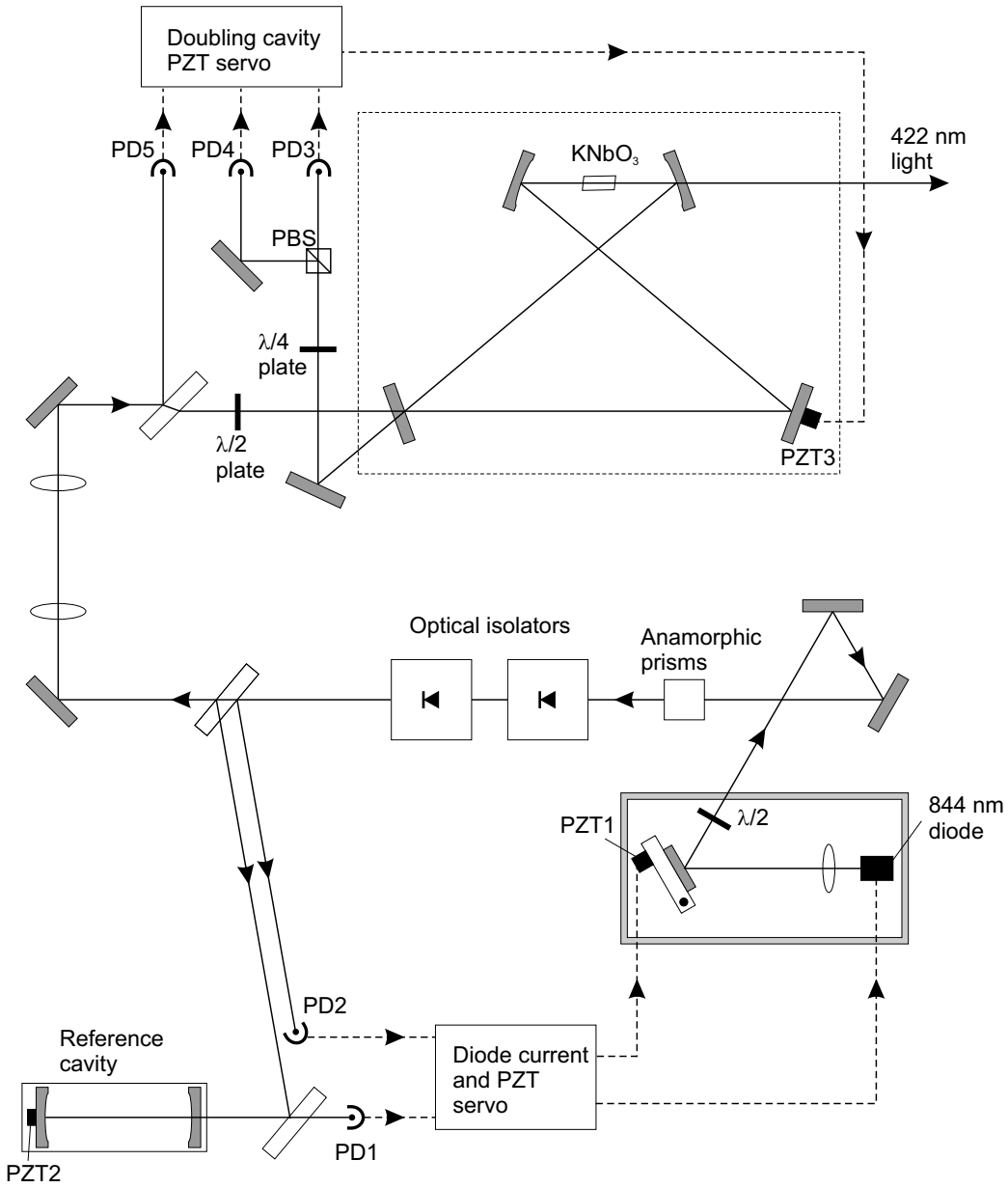

Figure 3.7: Diagram of cooling laser set-up

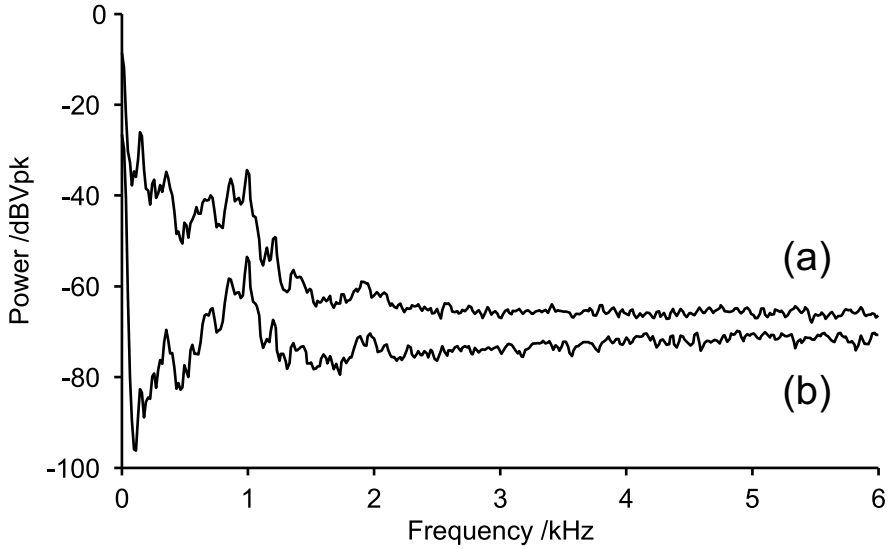

Figure 3.8: FFT of 844 nm diode laser side-of-fringe lock error signal, with (a) free-running laser and (b) laser stabilised to reference cavity

achieve the non-critical phase matching condition. Around 28 mW of the fundamental 844 nm light is coupled into the enhancement cavity with a mode matching efficiency of ∼70% yielding up to 2.6 mW of doubled light. The enhancement cavity is kept resonant with the fundamental using the Hänsch-Couillaud technique [74]. The polarisation analysers (made up of the quarter wave plate, polarising beam splitter and photodiodes PD3 and PD4) are made independent of beam intensity by dividing the output signals by that from an intensity reference photodiode, PD5 using an analogue divider IC. The enhancement cavity length is stabilised by feedback to a cavity mirror mounted on a piezo-electric transducer (PZT3). Notch filters tuned to the strongest two mechanical resonances of PZT3 are placed in the servo loop. This allows the servo gain to be increased without exciting mechanical resonances of the piezo-electric transducer.

For long term stability, the cooling laser is offset locked to the Doppler-free 5s $^2S_{1/2}(F''=2)$ – 6p $^2P_{1/2}(F'=3)$ transition in ^{85}Rb using saturated absorption spectroscopy. The 5s $^2S_{1/2}(F''=2)$ – 6p $^2P_{1/2}(F'=3)$ transition lies 440 MHz below the cooling transition in $^{88}Sr^+$ [56]. A double passed acousto-optic modulator (AOM) is used to down-shift light from the cooling laser to perform the saturated absorption spectroscopy. A first derivative signal of the transition spectra with which to stabilise the cooling laser is obtained by modulating the AOM drive frequency at 20 kHz and using lock-in detection. An integrator servo applies feedback to the 844 nm diode laser reference cavity piezo (PZT1). The cooling laser frequency is tuned by varying the double passed AOM drive frequency.

The output of this laser is used for Doppler cooling and optical pumping on the 5s $^2S_{1/2}$ – 5p $^2P_{1/2}$ transition. The cooling light is switched using both an AOM and a mechanical shutter. The AOM provides a fast switching time with an extinction ratio of ∼2000. The mechanical shutter is placed just before a pinhole in a focus of the beam give perfect extinction, but has a minimum opening time of around 500 μs. This beam of provides upto 75 μW and is split into three beams (cooling beams 1, 2 and 3) by beam splitters with $2w_0 = 100$ μm spot sizes at the ion. The optical pumping beam is circularly polarised using a Glan-Taylor polariser and quarter wave plate. This beam is also switched using an AOM and mechanical shutter.

3.7 Repumper laser

Light at 1092 nm needed to drive the 4d $^2D_{3/2}$ – 5p $^2P_{1/2}$ repumper transition is generated by a neodymium-doped fibre laser [56] (see fig 3.9). The Nd^{3+}-doped fibre is pumped at 825 nm by a diode laser (SDL-5421-G1). The 6 mW output of the fibre laser consists of a large number of modes at 15 MHz intervals under a ∼1.4 GHz envelope. This mode spacing corresponds to the modes of the cavity made up by the 6 m fibre and its grating output coupler. Unlike the other lasers described in this chapter, the repumper laser is not stabilised, as when one of the modes of the fibre laser drifts out of resonance with the transition an adjacent mode drifts in to resonance. This laser provides upto 2 mW of light into a $2w_0 \sim 560$ μm spot at the position of the ion.

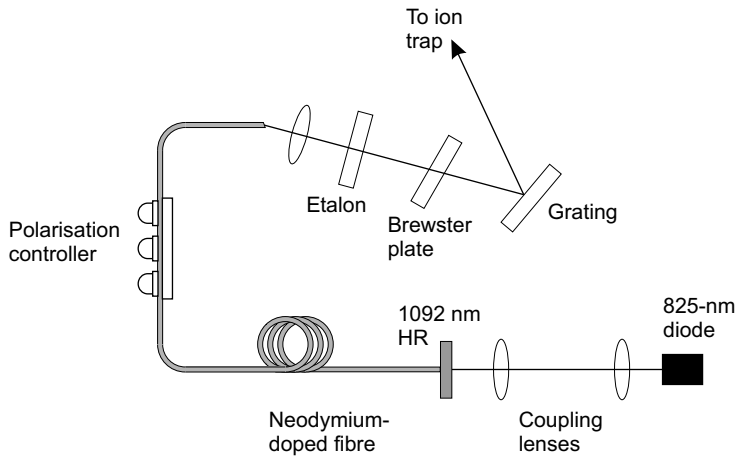

Figure 3.9: 1092 nm repumper laser

3.8 Probe laser

A master-slave diode laser system is used to generate radiation at 674 nm for probing and manipulating the ion on the 5s $^2S_{1/2}$ – 4d $^2D_{5/2}$ quadrupole transition. Two slave lasers are sideband injection locked [75] to the master laser. The master and slave lasers are all New Focus Vortex extended cavity diode lasers and output up to 5 mW of 674 nm radiation each.

The master laser linewidth is reduced to $\sim$ 3 kHz by stabilisation to a reference cavity of 1500 MHz free spectral range and finesse of 1500 using the Pound-Drever-Hall technique [73] (see fig. 3.10). In addition to having a narrow linewidth, the probe laser centre frequency must remain constant, requiring the reference cavity length to remain fixed. The cavity mirrors are therefore optically contacted onto a Corning ultra-low expansivity (ULE) glass spacer and the reference cavity is temperature stabilised.

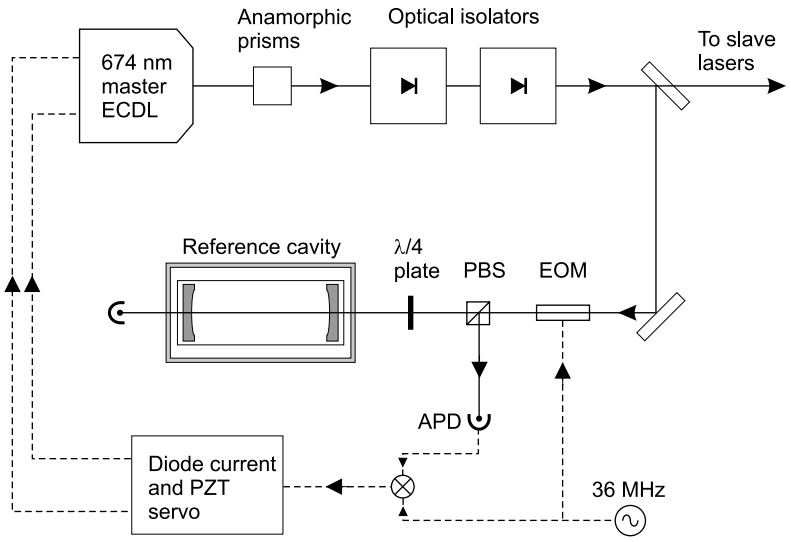

Figure 3.10: Probe laser, master ECDL set-up

The electronic servo loop used to stabilise the laser to the ULE cavity is similar to that used to lock the 844 nm diode laser to its reference cavity as described in section 3.6. A double integrator circuit in a 'bypass' topology [73] in parallel with a high pass filtered proportional amplifier provides feedback to the diode current. The high pass filter channel of the servo loop is required to compensate for the response function of the reference cavity [76], which acts as a low pass filter. An integrator servo is used to provide feedback to the diode laser extended cavity piezo. The resulting reduction in noise of the error signal is shown in figure 3.11.

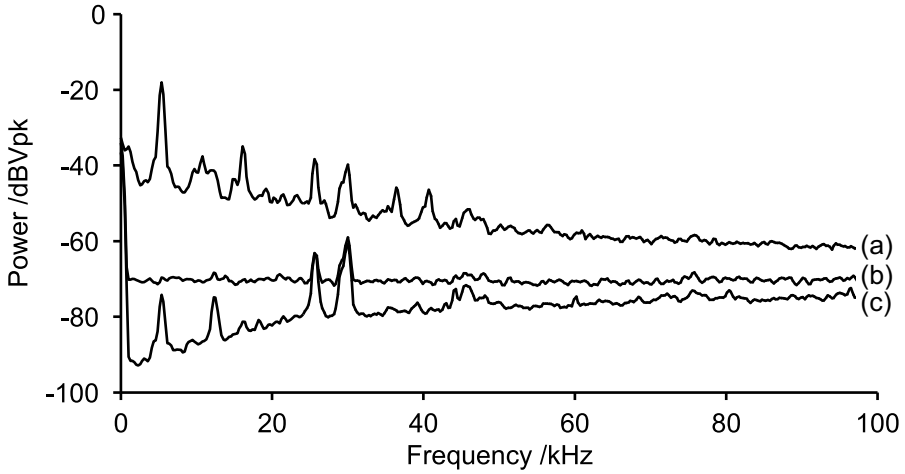

Figure 3.11: FFT power spectrum of 674 nm master laser error signal when (a) free running, (b) stabilised to ULE reference cavity using using feedback to the grating piezo and (c) stabilised using feedback to both grating piezo and diode drive current.

The reference cavity is mounted within a temperature stabilised vacuum chamber at a pressure of 2×10^{-7} mbar. To reduce the sensitivity of the temperature stabilisation servo to thermal drifts in DC amplifier offsets, a lock-in amplifier is used as the first stage of the servo. The temperature

stabilised vacuum chamber is housed in a temperature controlled enclosure to further isolate the cavity from fluctuations in the ambient temperature. This two stage temperature stabilisation of the reference cavity enables a reduction in the drift rate of the laser to less than $\sim$2 kHz/hour.

In order to produce a tunable output of the power necessary for coherent excitation (see chapters 6 and 7) and sideand cooling (see chapter 9) on the quadrupole transition, a slave laser is sideband injection locked [75] to the master laser (see fig. 3.12). In this technique, the slave diode laser has RF sidebands imposed on its output spectrum by modulating the drive current. A few microwatts of light from the master laser is injected into the slave laser. When the slave laser is tuned such that one of the sidebands approaches the master laser frequency, the slave laser optically phase locks to the master laser. The sideband injection lock therefore transfers the narrow linewidth and stability of the master laser to the slave laser. The slave laser can then be tuned with respect to the master laser by varying the modulation frequency of the drive current.

To ensure long term operation of the sideband injection lock, the slave laser extended cavity length is adjusteded to keep the slave laser within the capture range of the lock by an additional servo loop. The discriminant for this feedback loop is obtained by measuring the phase difference between the slave laser modulation frequency and the beat between master and slave lasers.

Two slave laser systems of identical design are locked to the master laser, the first delivers the weak probe beam of up to 750 μW into a spot size of $2w_0 = 260$ μm at the ion and the second gives the intense probe beam

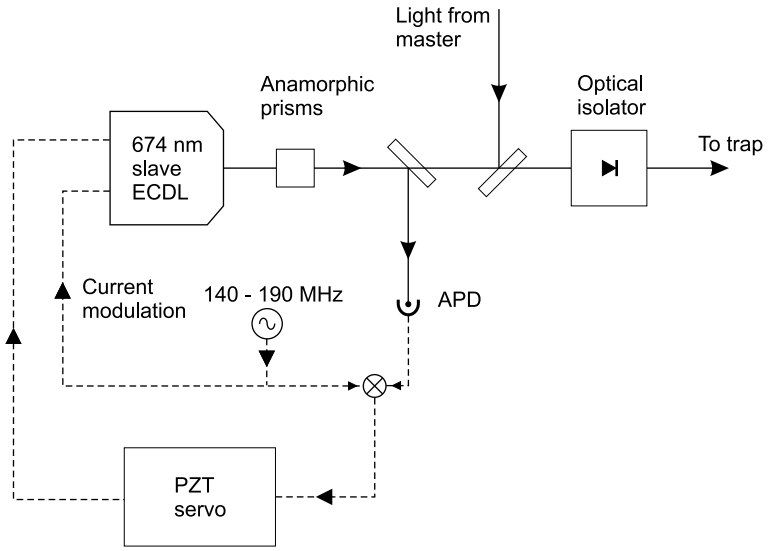

Figure 3.12: Probe laser, slave ECDL set-up

providing 1.5 mW into $2w_0 = 30$ μm at the ion. The weak probe beam is switched using an AOM only, giving an extinction ratio of $\sim$2000. The intense probe beam is switched using both an AOM and mechanical shutter. The intense probe beam AOM is switched on and off using Minicircuits ZYSWA-2-50DR high speed RF switches. Using two switches in series, an RF extinction ratio in excess of 70 dB is achieved.

3.9 Quencher and clearout laser

A diode laser is used to generate light at 1033 nm for driving the $^2D_{5/2}$ – $^2P_{3/2}$ quencher/clearout transition. The diode laser is set up in a Littrow configuration extended cavity in a temperature controlled enclosure. The laser produces an output of up to 5 mW at 1033 nm. Some of this light is used to stabilise the laser to a temperature controlled tunable reference cavity

by locking to the side of a transmission fringe. The side-of-fringe discriminant is made independent of the laser intensity by dividing the transmitted signal by an intensity reference signal (as used for locking the cooling laser to its reference cavity in section 3.6).

The output from this laser is divided in to two beam paths, the quencher beam and the clearout beam. The quencher beam is switched by both an AOM and mechanical shutter and provides up to 700 μW of light at the ion. The clearout beam is switched only by a mechanical shutter as the exact switching time is not critical and is capable of depopulating the $^2D_{5/2}$ state within 2 ms.

3.10 Experimental control and data acquisition

The experimental control system consists of a PC and four National Instruments data acquisition and control cards - a PCI-6602 high-speed counter-timer card, PCI-6533 digital I/O card, PCI-6713 analogue output card and PCI-GPIB GPIB card. These cards are controlled by routines written in LabVIEW[1]. The counter/timer has 8 counter devices and an on-board 80 MHz clock. The counters may be configured by LabVIEW for simple event counting, buffered event counting or pulse train generation. The digital I/O card has 32 TTL lines which are all configured as outputs and supports buffered clocked output. The analogue output card has 8 outputs and also supports buffered clocked output. The counter/timer, digital I/O and analogue out-

[1]National Instruments LabVIEW 6.0i

put cards are linked via an internal real time systems intgration (RTSI) bus system over which TTL signals can routed by software.

Many of the experiments described in this thesis require control of the apparatus with a timing resolution better than 1 μs. In addition, fluorescence counting using the counter/timer card must also be synchronised with control of the apparatus by the analogue output card and/or digital I/O card. Since LabVIEW software routines cannot respond faster than $\sim$1 ms, all synchronisation and as much of the switching logic as possible is carried using hardware triggering. In practice this means dividing down the counter/timer card's on-board clock to provided a fixed period pulse train to act as the master clock for the experiment. This clock signal is distributed via the RTSI bus to the other cards which are operated in a buffered clocked output mode. On each rising edge of the clock signal, the cards output the next output state contained in their respective buffers which are configured before the start of each experiment. One of the counters of the counter/timer card is dedicated to counting fluorescence forom the ion and is also configured to operate in a clocked[2] buffered mode. This allows the counts accumulated by the counter to be retrieved by LabVIEW at some time after the completion of an experimental cycle without the risk of losing data. Any elements of the experiments requiring control with resolution better than 1 μs are controlled by Stanford Research Systems DG535 digital delay generators which are set via GPIB commands and triggered by the digital I/O card.

The experimental control system is used to set laser frequencies, switch

[2]In the terminology of counter/timer operations this counter is not clocked, but *gated* by a timing pulse train

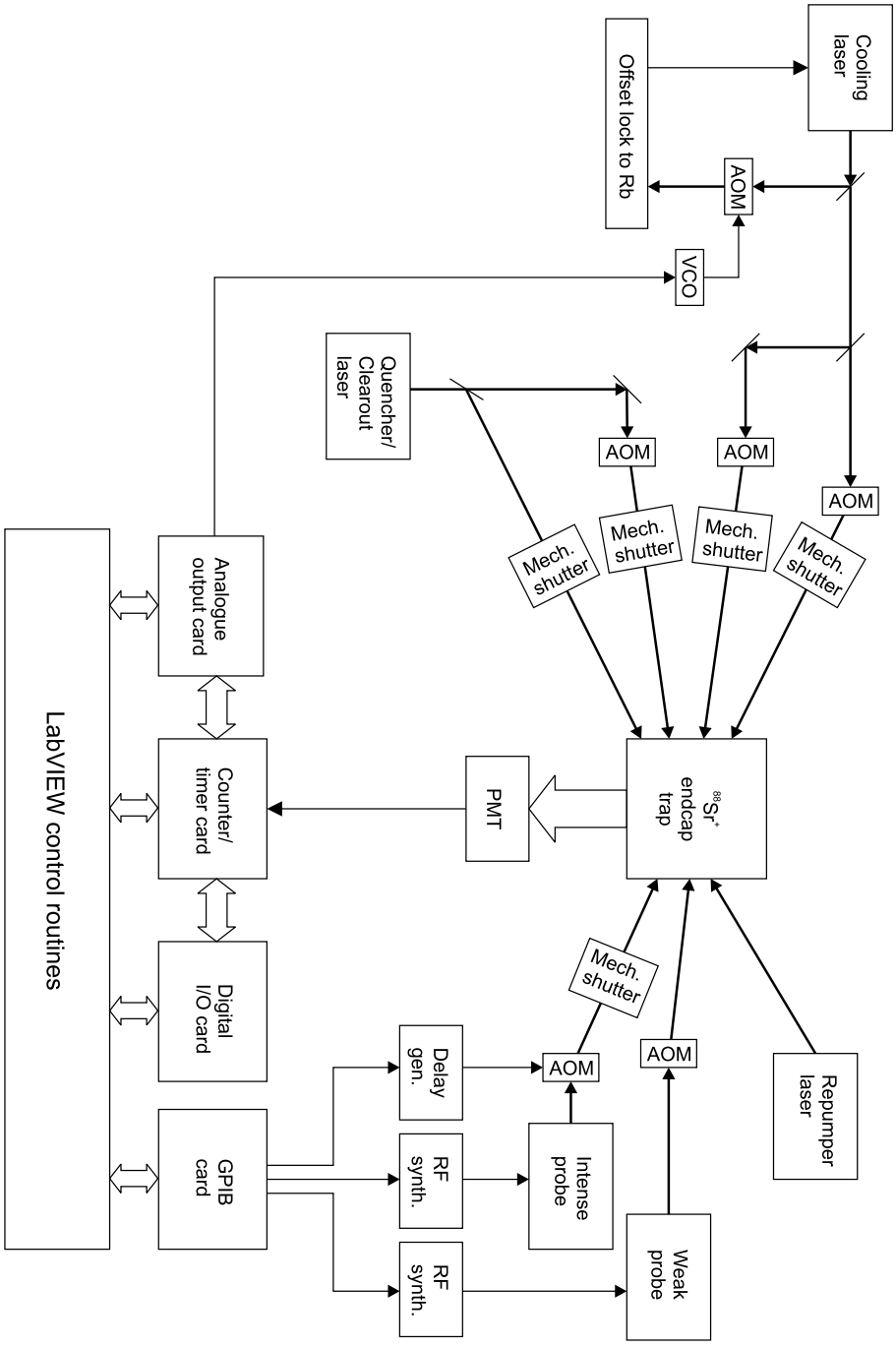

Figure 3.13: Overview of experimental control and data aquisition setup.

beams paths to the trap on and off, count fluorescence photons from the ion and determine its electronic state as needed (see fig. 3.13). The cooling laser is tuned by the changing the frequency of the offset lock to the ^{85}Rb saturated absorption feature. This is achieved by using the analog output card to vary the control voltage to the VCO providing the RF drive to the AOM in the offset lock. The frequencies of the weak and intense probe beams are set by GPIB control of the synthesiser used to modulate the slave laser for the sideband injection lock. Beams are switched on and off using a combination of AOMs and mechanical shutters controlled by the digital I/O card. The signals from fluorescence photons ariving at the PMT are converted to TTL pulses by an EG&G Ortec amplifier and discriminator setup. These TTL pulses are then counted by the counter/timer card.

3.10.1 Spectroscopy of the cooling transition

To obtain profiles of the 5s $^2S_{1/2}$ – 5p $^2P_{1/2}$ cooling transition lineshape the counter/timer card and analogue output card are used. A voltage ramp is calculated and stored in the analog output card buffer while counter 0 of the counter timer card is configured to generate a square wave of period 25 ms and counter 1 is set up for buffered counting. The square wave from counter 0 is sent via the RTSI bus to the clock input of the analogue output card and to to the gate of counter 1 of the counter/timer card (see figure 3.14). On each rising edge on the RTSI bus, the output voltage of the analogue output card is updated to the next value stored in the buffer. This outputs the voltage ramp to the VCO in the cooling laser offset lock, thereby scanning

the cooling laser frequency. At the same time, counter 1 commits the number of photons recorded between each rising edge of the clock signal to its buffer. These counts are then retrieved by LabVIEW after the scan is completed and post-processed to produce a profile of the cooling line shape.

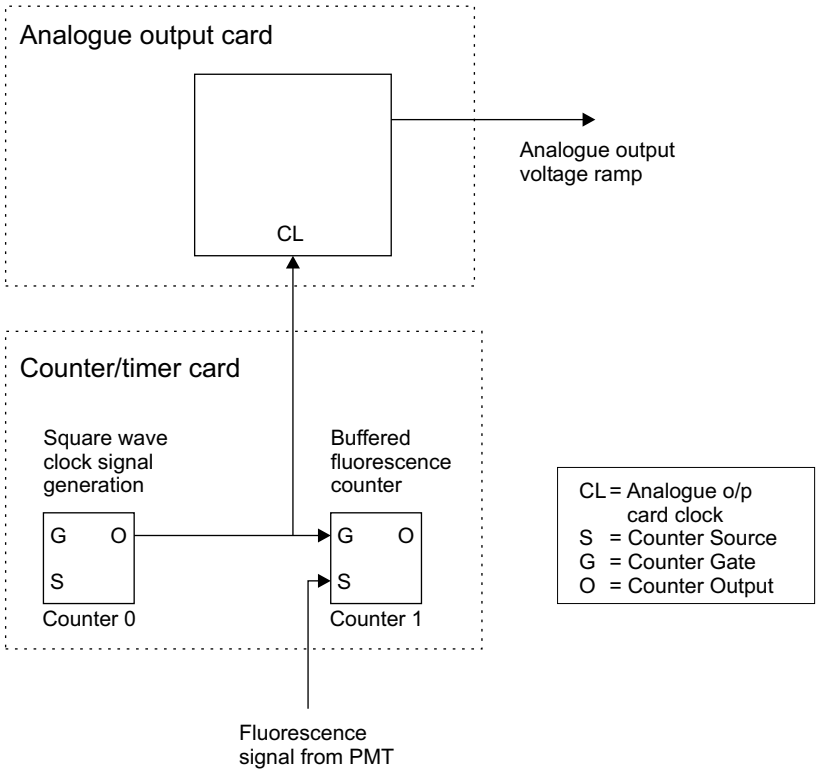

Figure 3.14: Analogue output card and counter/timer card setup used for obtaining profiles of the cooling transition.

3.10.2 Spectroscopy of the quadrupole transition

For spectroscopy and manipulation of the ion on the quadrupole transition, the counter/timer card and digital I/O card are used (see fig. 3.15). Each probe cycle is consists of two main tasks - the output of pulse sequences by

the digital I/O card and the counting of fluorescence to determine the ion's electronic state. The ion is probed a chosen number of times in order to accumulate statistics and determine the excitation probabilty. This process is repeated as a particular experimental parameter (such as the probe laser frequency, or probe pulse duration) is varied.

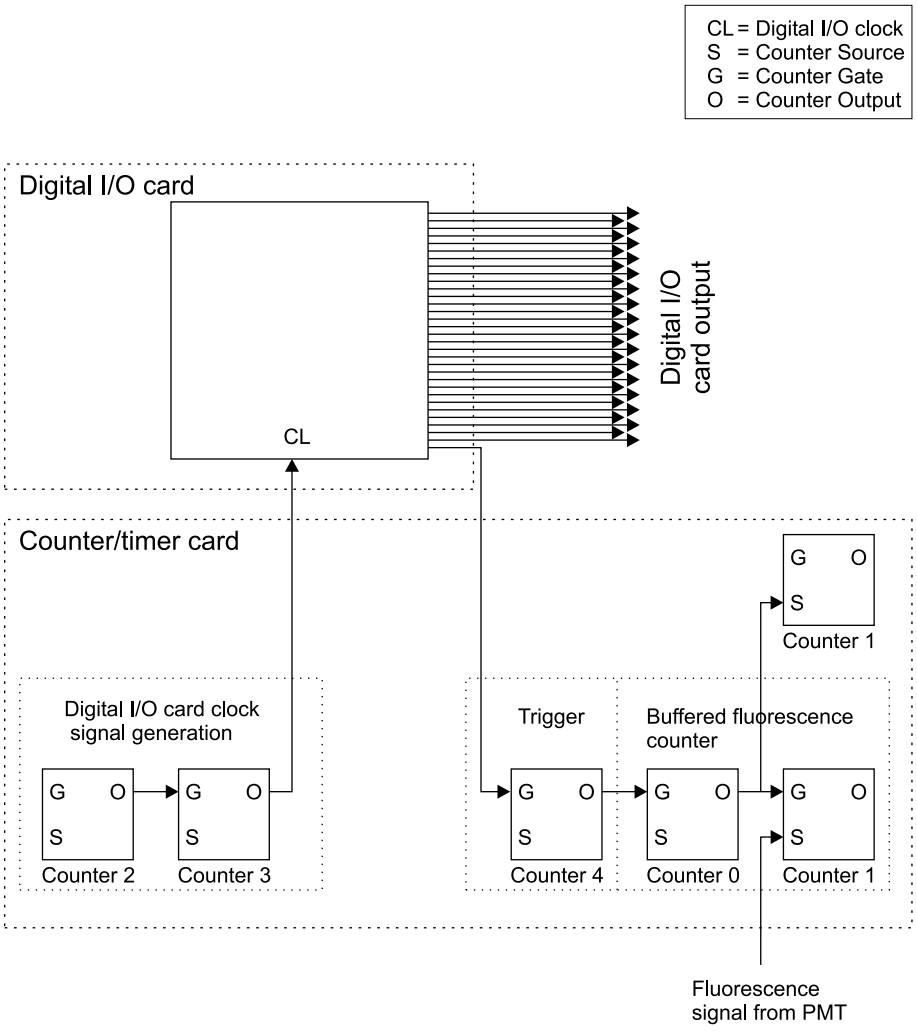

Figure 3.15: Digital I/O card and counter/timer card setup for interrogating the quadrupole transition

The experimental sequence is broken down into a series of 10 μs time

periods and the required logical state of each of the 32 digital I/O card outputs is calculated for each period. This sequence is loaded into the buffer of the digital I/O card which is configured for clocked output. In order to output every 10 μs period in this buffer once and once only, the digital I/O card clock line must receive exactly the same number of rising edges as points in the buffer - one for each 10 μs section of the experimental pulse sequence. This is done by using a pair of counters - counters 2 and 3. Counter 3 is set to output a square pulse train of 10 μs period, but is gated by counter 2 which is configured to generate a single pulse of the duration required to output the digital I/O card's buffer once. This results in a pulse train of exactly the right number of pulses at 10 μs intervals to output the buffer.

Fluorescence photons detected at the PMT are counted by counter 1 which is set up for buffered event counting. Counter 0 is configured to produce a 5 ms period square pulse train which is used as the clock signal for counter 1. This results in the counts accumulated in each 5 ms bin (i.e. between rising edges from counter 0) being stored in the counter's buffer for later retrieval by the LabVIEW control routine. To synchronise the first counting bin with the cooling light state detection pulse, the buffered event counting clock is gated 2.5 ms (half a bin) before the cooling light is switched on. To produce the gating signal, one of the output lines of the digital I/O card is set to output a trigger pulse sequence, which is converted to a TTL high signal by counter 4. The intermediate counter is needed because it is necessary to reset the gating signal independently of the digial I/O card buffer, which is required for the next probe cycle. The fluorescence counted in each bin is then read by LabVIEW as it is acquired. Once the number of

counts exceeds the state detection threshold 4.6.1 the probe cycle is complete and counter 4 followed by counters 0 and 2 are reset. If LabVIEW has been unable to empty the fluorescence count buffer quickly enough, there may be a backlog of count which need to be cleared. For this purpose counter 5 is used to count the number of bins elapsed. The difference between this value and the number of bins LabVIEW has already retrieved indivualy is the size of the backlog. The entire backlog is then retrieved from the buffer in one fast operation rather than on a bin by bin basis. It should be noted that from the time counter 1 is configured for buffered event counting it begins to count fluorescence from the PMT even though the first bin has not yet started. This means that the first count retrieved from the buffer in each probe cycle must be discarded.

Chapter 4

Trapping A Single $^{88}Sr^{+}$ Ion

4.1 Introduction

Before the experiments described in later chapters of this thesis can be performed, the endcap trap has to be loaded with a single ion and its micromotion minimised. For work requiring the Zeeman components of the quadrupole transition to be resolved, a magnetic bias field may be applied. The relevant Zeeman components can then be identified and their transition frequencies determined. This chapter details the methods used to accomplish these tasks for the basic day to day operation of the ion trap.

4.2 Loading the endcap trap

4.2.1 Trap 1

Trap 1 was loaded using the following procedure. A current of 4.2 A was passed through the $SrAl_4$:Ni oven for 30 s. During the last 10 s of this process,

a current of 3.5 A was passed throgh one of the filaments to produce electrons to ionise the atomic strontium. The cooling laser is detuned ∼250 MHz below line centre of the cooling transition in order to efficiently cool any hot atoms which have been ionised and trapped. The cooling laser frequency is then swept in towards the cooling resonance. If fluorescence is observed at greater than the background count rate due to cooling light scattered from the trap electrodes, an ion (or a number of ions) has been trapped.

To determine whether a single ion rather than a number of ions has been trapped, the micromotion is minimised in 1D by maximising the fluorescence just below line centre of the cooling transition (see section 4.3) and the cooling lineshape examined. If more than one ion is present, a low peak fluorescence rate will be observed, and the fall off in fluorescence as the cooling laser is tuned above line centre will not be sharp. In addition, as the laser is tuned back below resonance, there is a quick return of fluorescence when a single ion is present, as opposed to a slow return when there are a number of ions trapped.

If a number of ions has been loaded in to the trap, the excess ions are removed from the trap by blocking the repumper light. With the repumper light blocked, the ions are optically pumped into the metastable $^2D_{3/2}$ state and Doppler cooling effectively ceases. Without laser cooling, the ions are slowly heated out of the trapping potential. After a period of between 1 and 5 mins, the repumper is unblocked and the ion(s) Doppler cooled. This period is chosen to be short enough that not all of the ions are heated out of the trap. If there is still more than one ion in the trap, the process is repeated by blocking the repumper beam again.

4.2.2 Trap 2

Strontium atoms required for loading trap 2 are produced in a two-stage process (see section 3.2). In the first stage, the 'hotplate' is loaded with strontium. The two ovens containing the $SrCO_3$:Ta mixture are heated alternately for 30 s each, reaching a temperature of ∼1200 °C for the last 10 s. The ovens are heated by passing a current of between 7.0 and 7.4 A through them. This process is repeated four times to charge the hotplate. In the second stage the hotplate is heated for 30 s to ∼400 °C to produce strontium directed at the trap. During the last 12 s of this process, a current of 3.5 A is passed through one of two filaments. The filament is biased at -35 V to produce electrons with which to ionise the atomic strontium from the hotplate. The oven assemblies, which are in close proximity to the filament and normally earthed, are also biased to -35 V to prevent them from drawing the electrons towards themselves and away from the trapping region. On each successive loading of the trap, the current used to heat the hot plate is increased by ∼0.05 A from 6.0 A on the first load until a current of 8.0 A is reached. At this point there is no longer enough strontium left on the hotplate to load the trap and the hotplate must be recharged.

To maximise the probability of loading an ion, trap 2 is also made more shallow than is normally the case. This is done by reducing the RF power incident on the helical resonator trap drive by 3 dB. As was the case for trap 1, the cooling laser is detuned ∼250 MHz below the cooling transition. While the ion is being loaded, all three cooling beams and both repumper beams are incident on the trap. If a number of ions have been trapped, the

extra ions can be removed from the trap by blocking the repumper laser to stop the Doppler cooling process as described in section 4.2.1.

4.3 Minimising micromotion

In general, when the trap is loaded, stray electric fields will cause a displacement of the ion from the centre of the trapping potential. These stray fields are attributed to two mechanisms. Firstly, the oven or hotplate which produces neutral strontium to load the trap is situated on one side of the trap electrodes (see figures 3.2 and 3.3). As the trap is repeatedly loaded, this will lead to an uneven coating of the electrodes with strontium, causing contact potentials. Secondly, the electrons used to ionise strontium during the loading process are emitted over a large solid angle and unevenly charge the insulating surfaces around the trap (such as the macor support structure).

Displacement of the ion from the centre of the trapping potential leads to 'micromotion', the driven motion of the ion synchronous with the radio-frequency trapping field. Micromotion results in the modulation of atomic transitions such that the spectrum exhibits a carrier and RF sidebands, complicating the observed quadrupole transition spectra and reducing the coupling strength of the probe laser with the ion. For larger linewidth transitions such as the cooling transition, where the carrier and sidebands cannot be resolved, this is observed as a broadening of the transition. Micromotion also limits the storage time of the ion in the absence of laser cooling. In addition, micromotion leads to second order Doppler shifts and Stark shifts (as the electric field is zero only at the centre of the trap) in transitions frequen-

cies. These shifts however are not a limiting factor in the work described in this thesis and are mainly of concern in high precision spectroscopy of narrow transitions for optical atomic clocks and frequency standards work (see refs. [10, 77] for instance).

As the micromotion is driven motion it can not be significantly reduced using techniques such as laser cooling. It is therefore vital that the micromotion is minimised by positioning the ion at the centre of the trapping potential. This is accomplished by applying voltages to the compensation electrodes (see figure 3.1) to displace the ion in the horizontal plane and to the outer endcap electrodes to displace the ion axially. A number of techniques may be used to determine the magnitude of the ion's micromotion and are discussed extensively by Berkeland et al. [71]. In the work described in this thesis, the micromotion is first reduced by adjusting the compensation voltages to maximise the fluorescence observed just below resonance on the cooling transition. The more sensitive fluorescence modulation technique [78, 71] (see section 4.3.2) is then used to minimise the micromotion.

4.3.1 Coarse compensation

Micromotion leads to broadening of the observed cooling transition linewidth, and a reduction in the fluorescence rate measured at line centre. This may be used as a diagnostic to coarsely minimise the ion's micromotion. The cooling laser is tuned to just below line centre of the cooling transition. To minimise the micromotion in all three dimensions, three non-coplanar cooling beams are used. The unit vectors of the three cooling beams (1, 2 and 3)

given in table 3.1 have k-vector components in all three dimensions and are therefore sensitive to micromotion in all three dimensions. The compensation voltages are then adjusted to maximise the detected fluorescence rate, thus minimising the component of micromotion parallel to the cooling beam used.

Since the three cooling beam directions are not orthogonal and the compensation electrode geometry is such that micromotion along any one beam cannot be independently adjusted without affecting the others, an iterative process is used to minimise the micromotion along all three cooling beams simultaneously.

It has been found that the following iterative strategy converges quickly. The micromotion along beam 1 is minimised by varying the voltage on compensation electrode 1 and then compensation electrode 2 is used to minimise the micromotion along beam 2. This is repeated several times to minimise the micromotion in the plane of beams 1 and 2. The fluorescence rate is then measured using beam 3. This procedure is repeated, each time adjusting the compensation voltages applied to the outer endcap electrodes to try to maximise the fluorescence rate along beam 3. Once the fluorescence rate is maximised along beams 1, 2 and 3 simultaneously, the micromotion has been coarsely reduced in all three dimensions.

4.3.2 Fine compensation: fluorescence modulation technique

A more sensitive method for measuring the micromotion is the fluorescence modulation technique [78, 71], also known as the RF-photon correlation tech-

nique. Since the 7.4 ns lifetime [50] of the $^2P_{1/2}$ state is much shorter than the 63 ns period of the 15.9 MHz RF trapping potential, the ion's micromotion modulates the ion's fluorescence due to the first order Doppler effect. This modulation at the RF trap drive frequency is greatest when the cooling laser is tuned to the steepest slope of the cooling lineshape (see figure 4.1). For greatest sensitivity, the cooling laser is therefore detuned $\Gamma/2$ below line centre of the cooling transition.

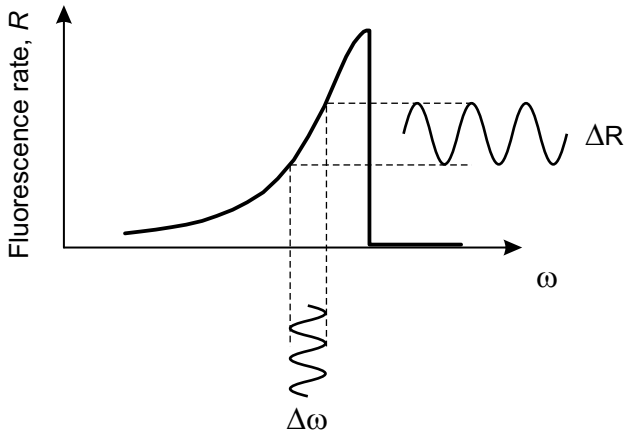

Figure 4.1: Due to its micromotion the ion is Doppler shift up and down the absorption profile of the cooling transition. This leads to the modulation of the fluorescence rate at the trap drive frequency.

The fluorescence modulation at the RF drive frequency is measured as follows. A time-to-amplitude-converter is used to generate an output voltage proportional to the time between the start of an RF trap drive cycle and the next photon registered by the PMT (see figure 4.2). The start and stop triggers for the time-to-amplitude-converter are the zero-crossings of the trap drive and the trigger pulses from the counting electronics respectively. These voltages are binned by a multi-channel-analyser. The compensation

voltages are then adjusted to minimise the modulation on the resulting traces. Typically a 15 s integration time is used to acquire modulation traces.

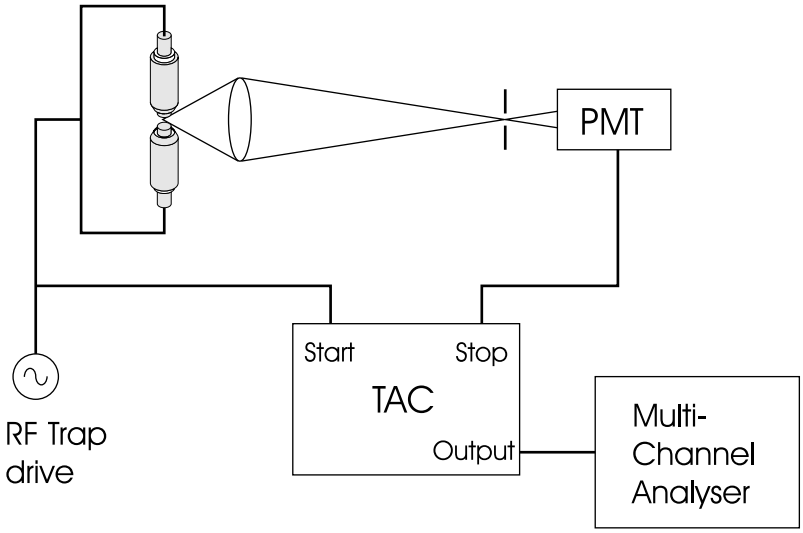

Figure 4.2: Time-Amplitude-Converter setup used for fluorescence modulation technique.

To ensure that the observed modulation is due solely to the ion's micromotion (rather than intensity modulation of the cooling laser due to RF pickup of the trap drive, for example) RF-photon correlation traces of light scattered from the trap electrode without a trapped ion present have been checked for modulation. No such effect was found.

To minimise the micromotion in all three dimensions, the iterative strategy used in section 4.3.1 is employed. Figure 4.3 shows typical RF-correlation traces observed after the micromotion has been reduced using the coarse method of section 4.3.1 and after the micromotion has been further reduced using the fluorescence modulation technique.

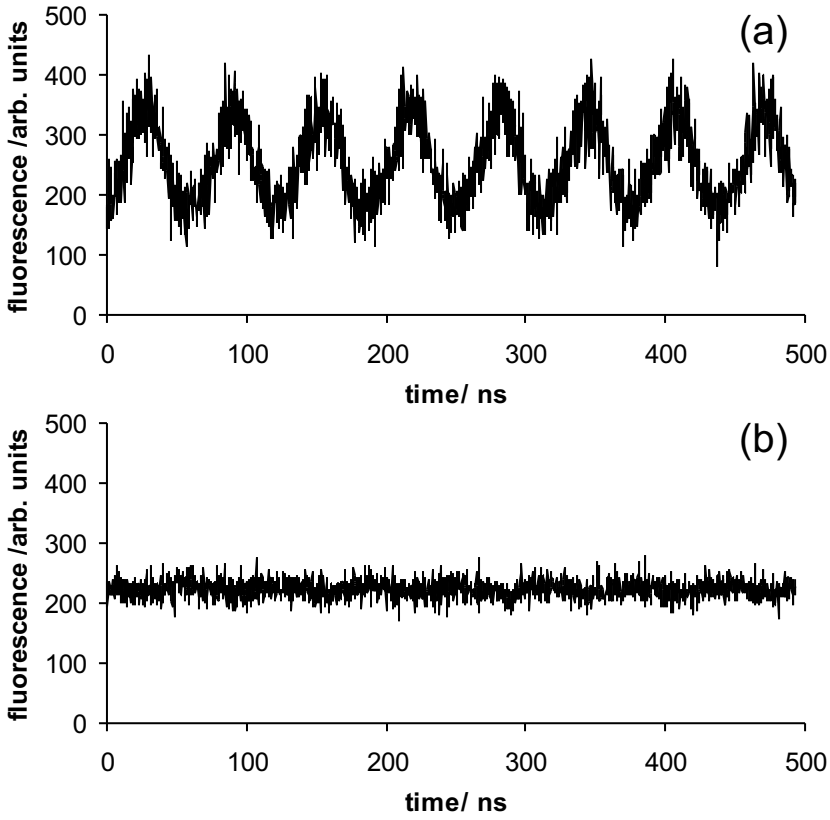

Figure 4.3: Typical fluorescence modulation observed when using cooling beam 3 at a power of 4.0 μW after (a) reduction of micromotion using the coarse method of section 4.3.1 (data recorded over 15 s integration time) and (b) further reduction of micromotion using the fluorescence modulation technique (data recorded over 60 s integration time).

4.4 Minimising the magnetic field

The spectrum of the quadrupole transition in a magnetic field is in general split into ten Zeeman components (see figure 4.9), each with axial and radial sidebands. Identifying each of these transitions is greatly simplified if they are resolved. This is achieved by applying a well chosen magnetic field. In addition, for sideband cooling (see chapter 9), well resolved transitions allow a closed cycle to be realised. The magnetic field is applied to the ion using three magnetic field coils arranged along the x, y and z-axes (see section 3.5). As the magnetic field is reduced to zero, the scattered light on the cooling transition also falls to zero. The magnetic field coil currents required to null the earth's field and stray fields from the ion pump, etc. are found roughly by looking for these fluorescence nulls on the cooling transition. The magnetic field is then reduced further by minimising the Zeeman splitting observed on the quadrupole transition. Once this has been done, bias fields applied using the magnetic field coils are calibrated by measuring the resulting Zeeman splittings.

It has already been noted that the fluorescence rate on the cooling transition falls to zero as the magnetic field is reduced to zero [53, 79, 80, 56]. This is attributed to optical pumping into dark Zeeman sub-levels of the $^2\mathrm{D}_{3/2}$ state in the following simple model. In a magnetic field, the repumper transition is split into six Zeeman components, two π components with $\Delta m_j = 0$ and four σ components with $\Delta m_j = \pm 1$. When viewed transversely to the magnetic field, the π and σ components are plane polarised orthogonally to each other [81]. All six Zeeman components may therefore be driven by

choosing the direction of polarisation of the linearly polarised repumper laser. If the polarisation of the repumper is parallel to the magnetic field, only the π components will be driven and the ion will become optically pumped into the dark $^2\mathrm{D}_{3/2}$ $m_j = \pm 3/2$ states. As the magnetic field is reduced to zero, the quantisation axis (previously defined by the magnetic field) is defined by the polarisation of incident repumper light. The polarisation of the repumper light can therefore be considered to be always parallel with quantisation axis, hence only the π components will be driven by the repumper laser and the ion will once again be optically pumped into the $^2\mathrm{D}_{3/2}$ $m_j = \pm 3/2$ states. It should be noted that if circularly polarised repumper light is used, the selection rule becomes $\Delta m_j = +1$ or -1 depending on the handedness of the polarisation leading to optical pumping into either the $m_j = +1/2$ and $+3/2$ states or the $m_j = -1/2$ and $-3/2$ respectively. A more rigorous treatment of dark states in Zeeman-degenerate systems is that of Berkeland and Boshier [82].

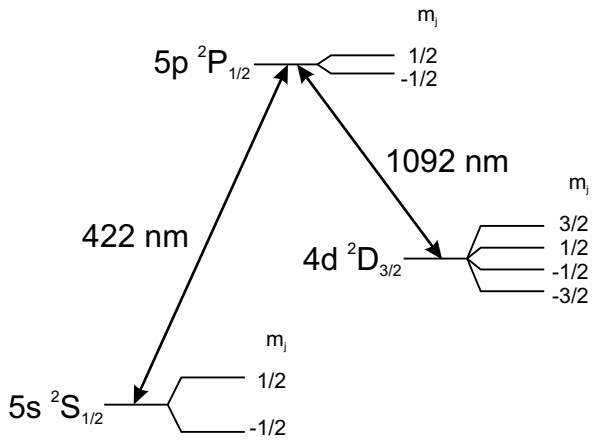

Figure 4.4: Zeeman sublevels of the $^2\mathrm{S}_{1/2}$, $^2\mathrm{P}_{1/2}$ and $^2\mathrm{D}_{3/2}$ states in small magnetic field.

The fluorescence nulling effect is used to coarsely minimise the magnetic field as follows. The second repumper beam is blocked so that only repumper beam 1 is incident on the ion. The remaining repumper beam is vertically polarised using a half-wave plate. Each of the magnetic field coil currents (I_x, I_y and I_z in the x,y and z-field coils respectively) are then adjusted to minimise the observed fluorescence rate. The fluorescence falls to zero not only when the magnetic field is zero, but also when the magnetic field is parallel to the polarisation of the repumper light. To avoid this condition, the polarisation of the repumper beam is chosen to be horizontal and I_x, I_y and I_z are varied to minimise the fluorescence. This process is repeated until the fluorescence is minimised for both polarisations simultaneously. With the magnetic field minimised and the cooling laser detuned to $\Gamma/2$ below line centre, a fluorescence rate of 3×10^3 s^{-1} is observed. In a small bias field, the fluorescence rate is restored to 2×10^4 s^{-1}. The fluorescence in zero magnetic field does not fall to the background level of scattered light from the trap electrodes. This is due to the imperfect linear polarisation of the repumper laser and any AC-magnetic fields present which cannot be nulled by the field coils.

After the magnetic field has been roughly minimised using the fluorescence nulling method, A Zeeman splitting of around 200 kHz is observed on the quadrupole transition. This corresponds to a magnetic field of around $\sim$20 mG (see equation 4.3) The field is further reduced by adjusting the magnetic field coil currents to further minimise the quadrupole transition Zeeman splitting. This process is repeated for both vertical and horizontal polarisations of the probe, as the line strength of each Zeeman component is

dependent on the orientation of the polarisation to the magnetic field [83]. Using this method, the Zeeman splitting on the quadrupole transition is typically reduced to 40 kHz, corresponding to a magnetic field at the ion of $\sim$5 mG.

To restore fluorescence and efficient Doppler cooling in zero magnetic field, techniques such as 'polarisation spinning' cite [82] may be used. In this technique the polarisation of the repumper is varied faster than the time taken for the ion to be optically pumped into a dark magnetic sub-level of the $^2D_{3/2}$ state. This method has been demonstrated using an electro-optic modulator to change the phase of the repumper light on the ion [80]. In the work described in this thesis, a different method is used to recover fluorescence at zero magnetic field. A second repumper beam with polarisation roughly orthogonal to the first is incident on the ion. This repumper beam is produced by redirecting repumper beam 1 back through the trap along a different beam path (see section 3.4).

4.5 Cooling transition spectra

With the micromotion minimised (see section 4.3) and the ion in a 3.6 G magnetic field, the cooling transition spectrum shown in figure 4.5 is observed. This spectrum is acquired by measuring the fluorescence as the cooling laser frequency is scanned over the cooling transition. For the spectrum shown in figure 4.5, cooling beam 3 was used at a power of 4.0 μW. The observed cooling lineshape is the sum of four unresolved Zeeman components of the cooling transition. The fall in fluorescence above line centre is attributed to

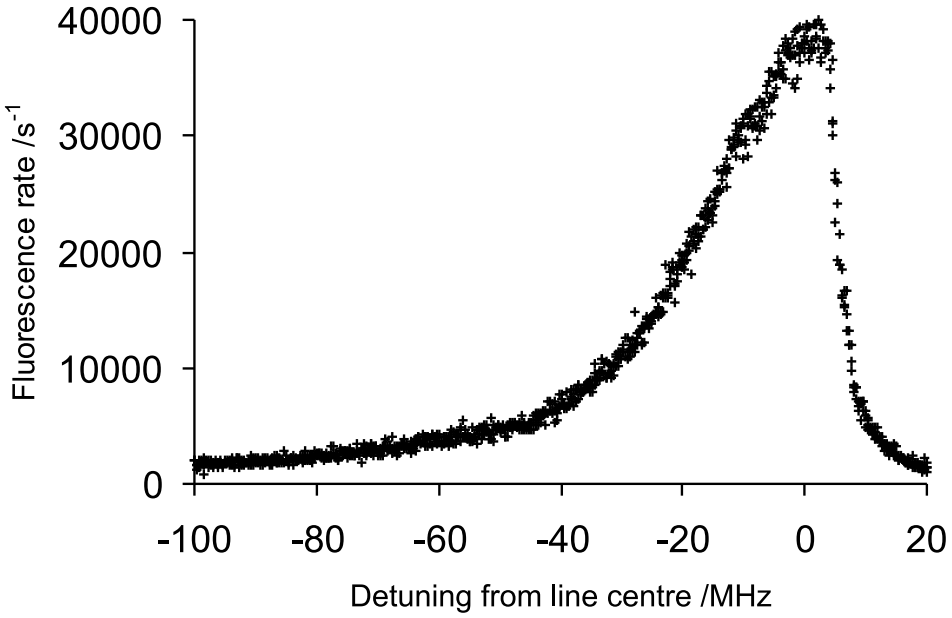

Figure 4.5: Cooling transition in 3.6 G magnetic field

heating of the ion by the blue detuned cooling laser. As the ion is heated, the Doppler effect shifts the cooling transition out of resonance with the cooling laser leading to the reduction in observed fluorescence. The lineshape has a width of 20 MHz at the half maximum points giving a FWHM of $\Gamma/2\pi$= 40 MHz. This is in good agreement with the 20 MHz natural linewidth of the cooling transition given the 13 MHz splitting between the highest and lowest frequency Zeeman components of the transition.

For Doppler cooling, the cooling laser is detuned approximately 20 MHz below resonance, where the fluorescence falls off to half the peak fluorescence observed at line centre. This corresponds to the $-\Gamma/2$ cooling laser detuning condition required for optimal Doppler cooling (see section 2.5).

4.6 Quadrupole transition spectra

This section describes how pulsed spectroscopy of the quadrupole transition is performed. Spectra of the quadrupole transition in zero magnetic field and a 3.6 G magnetic field are presented.

The method used to probe the quadrupole transition is similar to previously published routines [56, 84]. The typical experimental pulse sequence for one interrogation is shown in figure 4.6 and proceeds as follows. The ion is first Doppler cooled using 422 nm light from the cooling laser, detuned $\Gamma/2$ below line centre of the cooling transition. When working in a magnetic field, the ion may if necessary be optically pumped into the $m_j = -1/2$ magnetic sub-level of the $^2S_{1/2}$ electronic ground state using a pulse of circularly polarised 422 nm light (see section 4.7). The quadrupole transition is then

interrogated with a pulse of 674 nm radiation from the probe laser. Following this, the cooling laser is switched back onto the ion so that Dehmelt's electron shelving technique [47, 85] may be used to determine the electronic state of the ion. If the ion has been excited into the metastable $^2D_{5/2}$ state, it will be unable to scatter photons on the cooling transition. Therefore, if fluorescence is observed at the background rate, the ion has been 'shelved' in the $^2D_{5/2}$ state, but if a high rate of fluorescence is observed, the ion has not been excited to the $^2D_{5/2}$ state and is instead cycling on the cooling transition. Finally, if the ion has been 'shelved' in the $^2D_{5/2}$ state, the clearout laser is used to return the ion to the $^2S_{1/2}$ electronic ground state.

The ion is interrogated a number of times to determine the excitation probability. To build up a spectrum of the quadrupole transition, the excitation probability is measured as the probe laser frequency is stepped across the transition.

4.6.1 State Detection Threshold

Dehmelt's electron shelving technique exploits the fact that an ion in the $^2D_{5/2}$ state cannot scatter light on the cooling transition. Although the ion will scatter no photons when shelved, there will still be fluorescence at the background rate due to light scattered from the electrodes, etc. It is therefore clear that a 'state detection threshold' fluorescence rate must be set, above which the ion may be assumed to be cycling on the cooling transition and below which the ion is assumed to be shelved in the $^2D_{5/2}$ state.

The background fluorescence rate, R_D is measured by blocking the re-

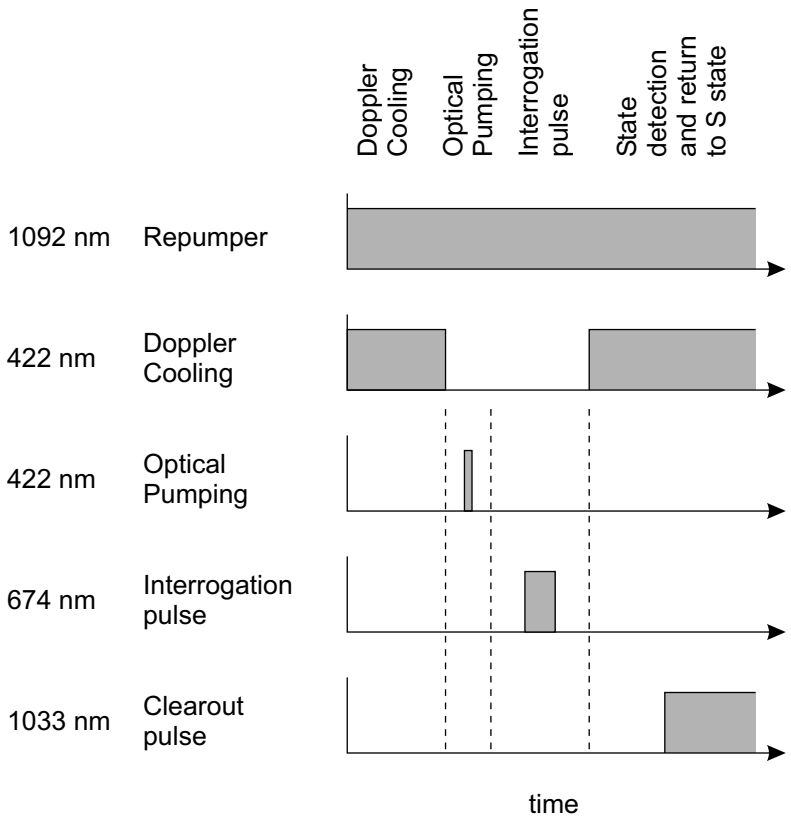

Figure 4.6: Typical experimental sequence used for pulsed spectroscopy of the quadrupole transition.

pumper light so that the ion becomes shelved in the $^2D_{3/2}$ state and counting the photons detected at the PMT over a period of 3 s. As the background rate does not change significantly over the course of one day, this is measured for each cooling beam at the beginning of each day the ion trap is operated. The fluorescence rate R_S observed when the ion is cycling on the cooling transition is determined by measuring the detected fluorescence over 100 ms with both the cooling and repumper lasers on the ion. This is done at just before a spectrum is acquired as the fluorescence rate may vary by up to 10 % over the day. This small variation is due to drifts in the repumper laser frequency, and changes in the ion's micromotion as the stray charge produced when loading the trap dissipates.

The state detection threshold is set as follows. The fluorescence detected at the PMT is counted in consecutive periods or 'bins' of duration t_d. If the ion has been shelved in the $^2D_{5/2}$ state, $D = R_D t_d$ counts are expected in one bin. If the ion has not been excited, $S = R_S t_d$ counts are expected. The threshold count T is set such that it is equal number of standard uncertainties $x\sigma_D$ above D and $x\sigma_S$ below S (see figure 4.7) giving

$$T = D + x\sigma_D = S - x\sigma_S \tag{4.1}$$

where x will now be referred to as the 'safety factor'. Since the standard errors in counting D and S are $\sigma_D = \sqrt{D}$ and $\sigma_S = \sqrt{S}$ respectively, equation 4.1 may be solved for x to give

$$T = \sqrt{SD}. \tag{4.2}$$

Below this threshold, the ion is assumed to be shelved in the $^2D_{5/2}$ state, while above the threshold, it is assumed that the ion has not been excited to the $^2D_{5/2}$ state. At the threshold, the probability of mistaking a shelved ion for one that is cycling on the cooling transition is equal to that of mistaking an ion cycling on the cooling transition for one which has actually been shelved in the $^2D_{5/2}$ state.

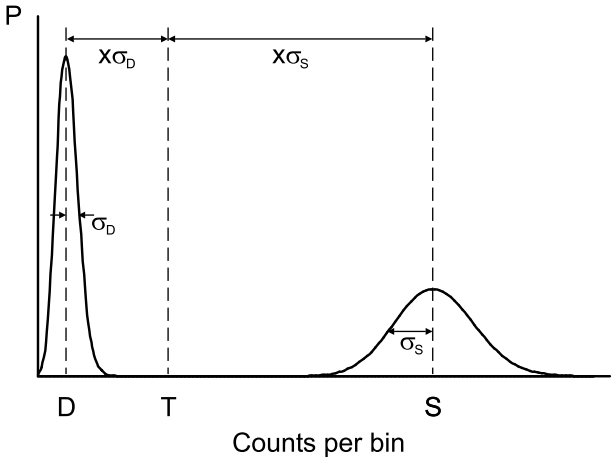

Figure 4.7: The state detection threshold, T is set so that it is an equal number of standard errors $x\sigma_D$ above D, the number of counts per bin expected if the ion is shelved in the D state and $x\sigma_S$ below S, the number of counts expected if the ion is cycling on the cooling transition.

Typically, bin periods of $t_d = 5$ ms are used. With a background scatter rate $R_D < 1.5 \times 10^3$ s^{-1} and a fluorescence rate on the cooling transition of $R_S = 2 \times 10^4$ s^{-1}, $D = 7.5$ and $S = 100$ counts per bin per bin are expected for a shelved and unshelved ion respectively. This results in a safety factor greater than $x = 7$. The probability of incorrectly determining the state of the ion due to counting statistics is less than $\sim 1 \times 10^{-12}$. Collisions between the ion and background gas particles in the UHV chamber may

cause a reduction in fluorescence as the ion is heated out of resonance with the cooling laser. An upper limit on the rate of these collisions is estimated to be 2.2×10^{-3} s^{-1} (see section 5.6.1). The probability of a collision occuring during a $\sim$20 ms interrogation cylce resulting in the state of the ion being incorrectly determined, is therefore less than $\sim 5 \times 10^{-5}$. The ion's electronic state is thus determined with almost unit detection efficiency.

4.6.2 Quadrupole transition spectrum in zero magnetic field

The quadrupole transition spectrum in figure 4.8 is observed when the ion is in zero magnetic field. For the spectrum shown, a 1.4 mW probe beam focussed into a 30 μm spot is used with a probe pulse of 20 μs duration. Each point is the result of 50 interrogations. The high beam power, large probe laser frequency steps and low number of interrogations at each frequency are chosen to reduce the length of time needed to aquired the spectrum. The spectrum consists of a carrier and axial and radial secular sidebands at $\omega_z = \pm$ 3.9 MHz and $\omega_r = \pm$ 2.1 MHz. The secular sidebands are due to the thermal motion of the ion in the trapping potential.

4.6.3 Quadrupole transition spectrum in 3.6 G magnetic field spectrum

In a magnetic field, the quadrupole transition is split into ten components (see figure 4.9). The energies of the $^2S_{1/2}$ and $^2D_{5/2}$ state magnetic sub-levels

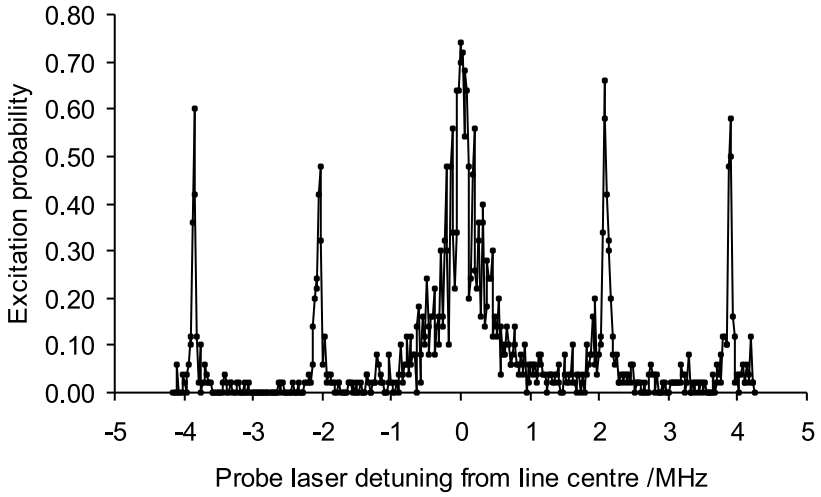

Figure 4.8: Spectrum of quadrupole transition in zero magnetic field, consisting of a carrier and axial and radial sidebands at $\omega_z = \pm$ 3.8 MHz and $\omega_r = \pm$ 2.1 MHz

are given by

$$\Delta E = g_j \mu_B B m_j \tag{4.3}$$

where μ_B is the Bohr magneton, B the magnitude of the magnetic field, m_j the magnetic quantum number of the sublevel and g_j is the Landé g-factor. For an ion with total angular momentum quantum number J, total spin angular momentum quantum number S and total orbital angular momentum L, the Landé g-factor is

$$g_j = \frac{3}{2} + \frac{S(S+1) - L(L+1)}{2J(J+1)} \tag{4.4}$$

The g-factors for the $^2S_{1/2}$ and $^2D_{5/2}$ states are therefore 2 and 5/6 respectively.

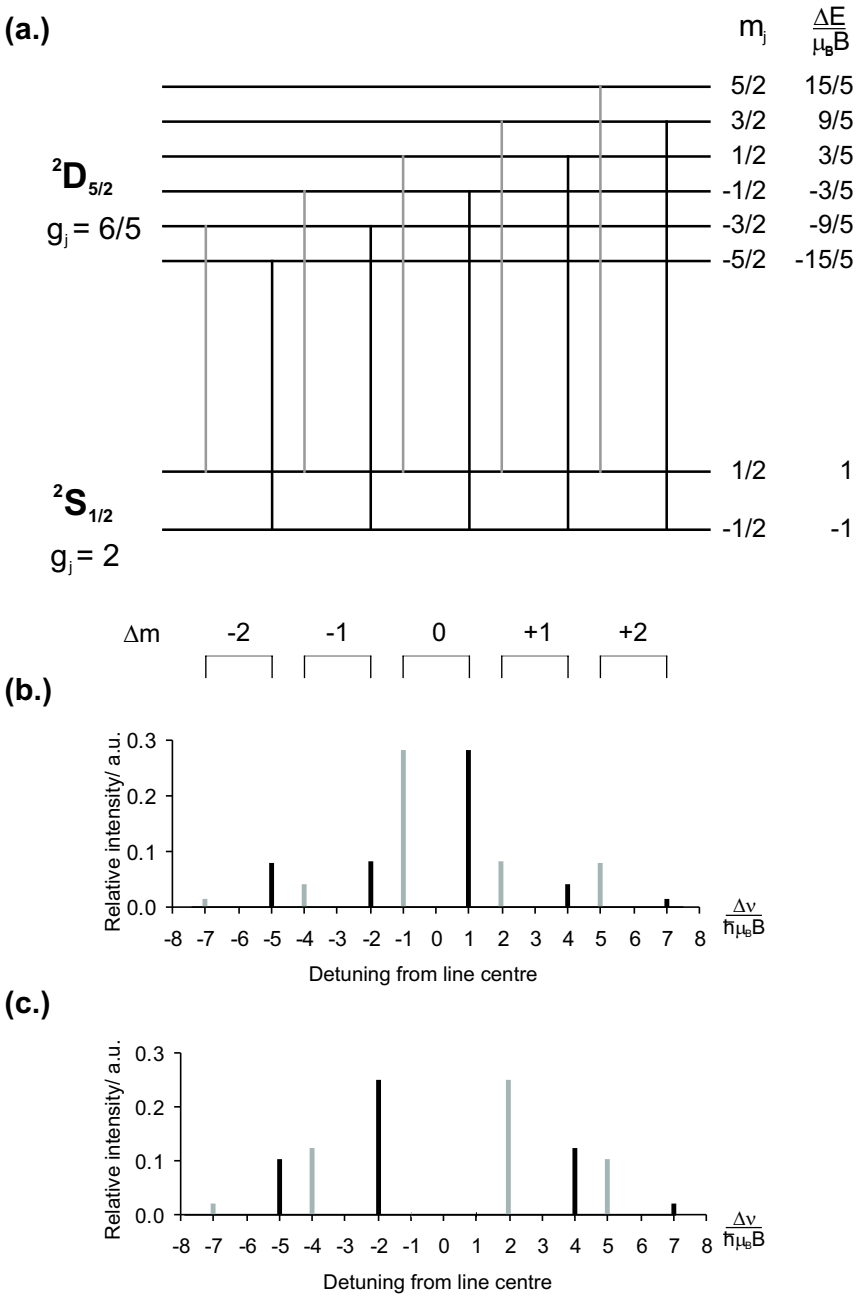

Figure 4.9: (a.) Energy splittings and g-factors of the $^2S_{1/2}$ and $^2D_{5/2}$ state magnetic sub-levels. Detunings and relative intensities of quadrupole transition Zeeman components with (b.) vertical and (c.) horizontal probe polarisations. The $\Delta m = 0$ components are not present when the ion is interrogated with a horizontally polarised probe beam.

The relative intensities of the Zeeman components are dependent on θ, the angle between the probe beam's direction of propogation and the magnetic field and ϕ the angle between the probe beam polarisation and the plane formed by the magnetic field and probe direction. The probe beam is inclined at $\theta = 30°$ to the direction of the magnetic field. The relative line strengths for vertical ($\phi = 0°$) and horizontal ($\phi = 90°$) probe polarisations calculated using the method outlined by James [83] are shown in figure 4.9. The $\Delta m = 0$ components are not observed when the probe beam polarisation is horizontal.

A high resolution scan of the $^2S_{1/2}$ ($m_j = -1/2$) – $^2D_{5/2}$ ($m_j = -1/2$) $\Delta m = 0$ Zeeman component is shown in figure 4.10. The probe laser is scanned across the transition in 500 Hz steps. At each frequency, the ion is interrogated 1000 times. A weighted-least squares fit of a Lorentzian to the transition gives a FWHM of $\gamma/2\pi = 2.4$ kHz. The free parameters is this fit were the transition frequency, peak excitation probability and FWHM. The natural width of the transition is 0.4 Hz. The observed width is attributed to the probe laser linewidth over the 5 minute timescale needed to acquire the spectrum and other broadening mechanisms such as ac-magnetic fields.

4.7 Optical pumping

When the ion is in a magnetic field, circularly polarised 422 nm light directed along the field can be used to prepare the ion in one of the magnetic sublevels of the electronic ground state (see figure 4.11). For this purpose, a σ^- polarised beam is used to drive the $^2S_{1/2}$ ($m_j = 1/2$) – $^2P_{1/2}$ ($m_j = -1/2$) component of the cooling transition resulting in optical pumping to the

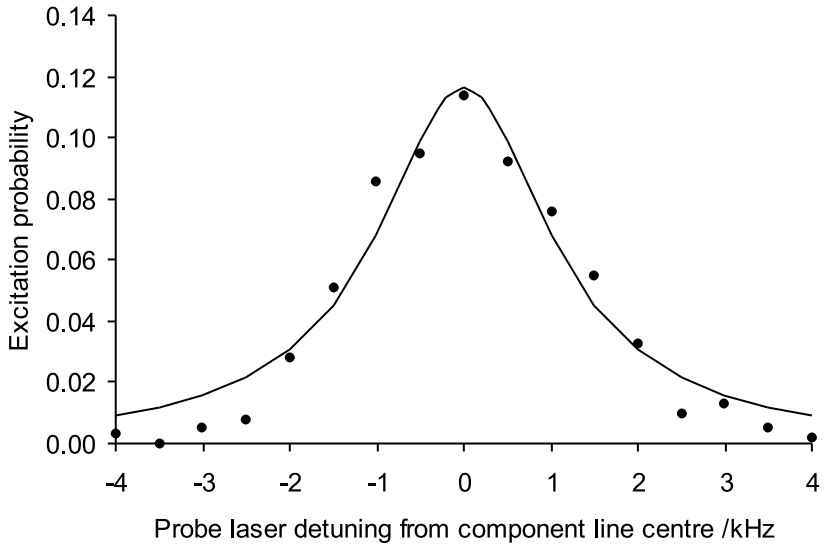

Figure 4.10: High resolution scan of the $^2S_{1/2}$ ($m_j = -1/2$) – $^2D_{5/2}$ ($m_j = -1/2$) $\Delta m = 0$ Zeeman component. Each point is the result of 1000 interrogations with the probe laser scanned in steps of 500 Hz. A 1 ms probe pulse was used and the probe intensity was 75 μW into 30 μm spot. The solid line is Lorentzian weighted least squares fit to the data, with FWHM of 2.4 kHz.

$^2S_{1/2}$ ($m_j = -1/2$) state. The optical pumping beam intensity is well below that needed to saturation the transition — with the beam set to vertical polarisation and tuned to $\Gamma/2$ below resonance, less than $3,000$ counts/s are detected by the photomultiplier tube.

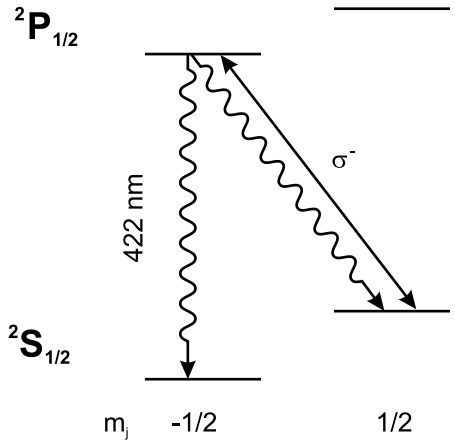

Figure 4.11: Optical pumping on the cooling transition. The ion is optically pumped into the $^2S_{1/2}$ ($m_j = -1/2$) sub-level of the electronic ground state using σ^- polarized light on the cooling transition.

The efficiency of the optical pumping process is measured by comparing the excitation probabilities on the $^2S_{1/2}$ ($m_j = -1/2$) – $^2D_{5/2}$ ($m_j = -1/2$) and $^2S_{1/2}$ ($m_j = -1/2$) – $^2D_{5/2}$ ($m_j = +1/2$) components of the quadrupole transition. An optimal optical pumping pulse efficiency of 97% is achieved using an optical pumping pulse duration of 20 μs. The optical pumping efficiency is reduced for shorter pulse durations.

A lower limit on the optical pumping efficiency may also be determined from the peak excitation probability when the $^2S_{1/2}$ ($m_j = -1/2$) – $^2D_{5/2}$ ($m_j = -1/2$) Zeeman component is coherently driven (see chapter 6).

4.8 Summary

The experimental methods used to trap a single $^{88}Sr^{+}$ ion in an endcap trap and acquire spectra of the cooling, quadrupole and quencher transitions have been detailed.

For loading trap 1, strontium was produced using an oven containing a $SrAl_4$:Ni mixture. In trap 2, an oven and hot-plate two-stage atomic strontium source is used to the avoid build-up of impurities on the electrode structure. Filaments are used to ionise the atoms for trapping in the endcap trap. Once trapped, the ion is Doppler cooled on the 422 nm cooling transition.

The ion's micromotion is detected by both monitoring the peak fluorescence at line centre on the cooling transition, and measuring the RF fluorescence modulation on the cooling transition. Compensation electrodes are then used to position the ion at the centre of the trapping potential and reduce its micromotion. The magnetic field is coarsely minimised using the fluorescence nulling technique and then further reduced by minimising the observed Zeeman splitting on the quadrupole transition.

Photons scattered on the cooling transition are detected at the PMT. Spectra of the cooling transition show a peak fluorescence rate of 4×10^4 s^{-1}. Therefore, a fluorescence rate of 2×10^4 s^{-1} is achieved when the cooling laser is detuend $\Gamma/2$ below line centre. A background fluorescence rate of less than 1.5×10^3 s^{-1} is observed. This allows almost unit detection efficiencey when determining whether the ion is in the $^2D_{5/2}$ state using Dehmelt's electron shelving method. Optical pumping into dark states of the $^2D_{3/2}$ in the absence of a magnetic bias field is avoided using two orthogonally

polarised repumper beams. This allows efficient Doppler cooling when no magnetic field is present.

Pulsed spectroscopy of the quadrupole transition has been performed. The ion's electronic state is determined using Dehmelt's electron shelving method. The spectra exhibit axial and radial sidebands. The motional frequencies observed in trap 2 are $\omega_z = \pm$ 3.8 MHz for the axial mode and $\omega_r = \pm$ 2.1 MHz for the radial mode. High resolution spectra of a single Zeeman component show a probe laser linewidth of 2.4 kHz.

When placed in a magnetic bias field, the ion may be prepared in the $^2S_{1/2}$ ($m_j = -1/2$) with a fidelity of greater than 97%. This is achieved by optical pumping using σ^- light on the cooling transition.

Chapter 5

Precision measurement of the 4d $^2D_{5/2}$ state lifetime

5.1 Introduction

This chapter, presents a precision measurement of the natural lifetime of the 4d $^2D_{5/2}$ state in $^{88}Sr^+$. The ion is prepared in the $^2D_{5/2}$ state by direct laser excitation of the $^2S_{1/2}$ – $^2D_{5/2}$ transition and the decay time measured using Dehmelt's electron shelving method [47, 85]. By accumulating 160,000 decay times, a measured lifetime that is over an order of magnitude more accurate than the previous best measurement [86] is obtained. The data used in the measurement presented here consists of 63,000 shelved periods recorded in May 2000 and 97,000 recorded in July 2002. The measured value of the lifetime is 390.3 ms.

A measurement of the lifetime of the 4d $^2D_{5/2}$ metastable state also gives the natural linewidth of the $^2S_{1/2}$ – $^2D_{5/2}$ transition. This transition is being

investigated as a reference 'clock' transition in an atomic frequency standard [6, 7] and as shown by work using the analogous quadrupole transition in $^{40}Ca^{+}$ [87, 45, 88], may also be used for investigations of quantum information processing and cavity QED. The lifetime of the $^{2}D_{5/2}$ state is useful in determining the ultimate limit to the stability of an optical clock based on the $^{2}S_{1/2}$ – $^{2}D_{5/2}$ transition. The $^{2}D_{5/2}$ state lifetime also imposes a limit within which all quantum computations using the $^{2}S_{1/2}$ and $^{2}D_{5/2}$ states as a qubit must be completed [16]. Knowledge of the lifetime is important for future cavity QED investigations using the quadrupole transition in $^{88}Sr^{+}$, for instance a strong atom-cavity coupling requires an atom-cavity interaction frequency greater than the rate of decoherence to the external environment.

Lifetimes of the metastable $^{2}D_{5/2}$ states are also of interest in astrophysics, since quadrupole transitions may be used as diagnostics of temperature and electron density in various astronomical objects [89]. The lifetime of the $^{2}D_{5/2}$ state may be of use in efforts to explain the origin of the forbidden $^{2}S_{1/2}$ – $^{2}D_{5/2}$ transition in recent spectroscopic studies of an emission filament of ejected matter from Eta Carinae [90].

A precision measurement of the $^{2}D_{5/2}$ state lifetime in $^{88}Sr^{+}$ offers a means of testing atomic structure calculations [91, 92, 93, 86]. There are several reported measurements of the 4d $^{2}D_{5/2}$ state lifetime in $^{88}Sr^{+}$, and have all been made using different approaches. The earliest reported measurement [94] used a cloud of ions in an R.F. quadrupole trap and monitored the exponential decay of photons at 674 nm. The first measurement using a single trapped ion [79] excited the $^{2}S_{1/2}$ – $^{2}D_{5/2}$ transition with a laser at 674 nm, and compared dark and bright periods of strong fluorescence at

422 nm. The technique of using a single ion, prepared in the 4d $^2D_{5/2}$ state, and accumulating statistics of decay times has also been used [95]. More recently, laser probing the metastable ions in a storage ring [86] has also yielded a measurement.

5.2 Experimental Method

The interrogation scheme used to measure the 4d $^2D_{5/2}$ lifetime is almost identical to that described in section 4.6. The ion is Doppler cooled and the count rate of fluorescence photons from the $^2S_{1/2} - {}^2D_{5/2}$ transition recorded. The cooling beam is then switched off and a pulse of 674 nm light irradiates the ion in order to excite it to the $^2D_{5/2}$ state. The cooling laser is switched on again and the count rate of 422 nm photons is recorded. If the ion has made the transition and is shelved in the 4d $^2D_{5/2}$ state, photons are recorded at the normal background count rate, D. However, if the ion has not been shelved in the $^2D_{5/2}$ state, then it will scatter light on the $^2S_{1/2} - {}^2P_{1/2}$ cooling transition and photons will be detected at the normal fluorescence count rate, S. A shelved ion is therefore easily identifiable with almost unit efficiency. The 1092 nm repumper light remains incident on the ion throughout the interrogation cycle.

Fluorescence photons from the cooling transition detected by the photomultiplier are counted in bins of $t_d = 10$ ms period. The state detection threshold count, T is given by equation 4.2. When the ion is detected in the $^2D_{5/2}$ state, the time taken for the ion to decay to the ground state is recorded. In practice this means recording the number of 10 ms bins which

elapse before the fluorescence rises above the threshold T.

This cooling, probing and interrogating process is repeated many times in order to record a large number of decays from the $^2D_{5/2}$ state.

5.3 Data analysis: fitting and estimation methods

5.3.1 Single-parameter model

The simplest approach to determining the lifetime from decay time data is to assume that the data is dependant on only one parameter: the lifetime of the $^2D_{5/2}$ state. For an atom prepared in an excited state of natural lifetime τ, the probability of decay per unit time at a time t is given by

$$P(t,\tau) = \frac{1}{\tau}\exp\left(-\frac{t}{\tau}\right). \tag{5.1}$$

The time taken for the ion to decay is repeatedly measured. Each observed decay period is known only to the nearest bin of duration t_d ($t_d \ll \tau$), where the ith bin ($i = 1, 2, 3\ldots$) extends in time from $(i-1)t_d$ to it_d. The mid-point of the ith bin occurs at the time $t_i = (i - \frac{1}{2})t_d$. If a total N_T decay periods are measured, from equation 5.1 the expected number of decays observed in the ith bin is given by

$$N(t_i,\tau) \approx N_T\frac{t_d}{\tau}\exp\left(-\frac{t_i}{\tau}\right). \tag{5.2}$$

It is therefore to be expected that over a large number of decay events, the number of shelved periods N_i ending in the ith bin will exhibit an exponential dependence on time, from which the lifetime τ may be determined.

Three different methods have been used in this work to determine τ from the recorded data using this single-parameter model: the weighted least squares fit, the maximum likelihood estimator of τ and the minimum variance unbiased estimator of τ. These methods will now be described, along with the means of estimating the statistical uncertainty in the value of τ.

5.3.1.1 Weighted least-squares fit

In the weighted least-squares fit [96], the best fit value of τ is that which minimises the sum of the squared deviations of each data point from the fitted curve in terms of the error on each point. In other words, the function $N(t_i, \tau)$ is fitted to the data (t_i, N_i) by varying the parameter τ to minimise the quantity

$$\chi^2(\tau) = \sum_i \left(\frac{N(t_i, \tau) - N_i}{\sigma_i} \right)^2 = \sum_i \left(\frac{N(t_i, \tau) - N_i}{\sqrt{N_i}} \right)^2 \qquad (5.3)$$

where $\sigma_i = \sqrt{N_i}$ is the standard uncertainty associated with N_i due to counting statistics.

The use of $\chi^2(\tau)$ as a measure of how well the function $N(t_i, \tau)$ fits the data (t_i, N_i) makes the assumption that both N_i and σ_i are normally distributed. However, in the case of exponentially distributed decay times, N_i and σ_i are governed by the Poisson distribution. For $N_i > 10$, the Poisson distribution is well approximated by the normal distribution, however for

$N_i < 10$ this approximation no longer holds and $\chi^2(\tau)$ ceases to be a good measure how well the theoretical curve fits the data. For this reason, bins in which less than 10 events are recorded are not included in the fitting procedure. In practice, this is done by truncating the data set at the first bin in which $N_i < 10$.

The standard uncertainty in the fitted value of τ is its 68.3% confidence interval. The boundaries of this interval $[\tau - u, \tau + u]$ are given by the two solutions of [96]

$$\chi^2(\tau \pm u) = \chi^2_{\text{min}} + \chi^2_{0.683,1} \tag{5.4}$$

where χ^2_{min} is the minimised sum of weighted least squares (given by equation 5.3) and $\chi^2_{0.683,1}$ is the 68.3% point of a one-tailed chi-squared distribution with one degree of freedom.

5.3.1.2 Maximum likelihood estimator

An alternative approach to determining the lifetime which best characterises the data is to find the value of τ which has the maximum probability of producing the observed data set. This technique is known as maximum likelihood estimation [97].

From equation 5.2, the number of decay periods ending in the ith bin is expected to be

$$X_i = N(t_i, \tau) = (N_T t_d/\tau) \exp(-t_i/\tau). \tag{5.5}$$

The probability of observing N_i decays in the ith bin is,

$$P(N_i) = \exp(-X_i)\frac{X_i^{N_i}}{N_i!} \tag{5.6}$$

according to the Poisson distribution. The probability of a particular value of τ producing the observed data set is therefore given by the likelihood function

$$L(\tau; N_1, \ldots, N_T) = \prod_i P(N_i) = \prod_i \exp(-X_i)\frac{X_i^{N_i}}{N_i!}. \tag{5.7}$$

The best estimate of τ will be the value which has the maximum probability of producing the observed data; i.e. the value of τ which maximises equation 5.7. For ease of computation, the log-likelihood

$$\ln[L(\tau)] = \sum_i [-X_i + N_i \ln(X_i) - \ln(N_i!)] \tag{5.8}$$

is maximised with respect to the single parameter τ.

For large samples, the Wilk's likelihood ratio statistic

$$W = 2\ln[L(\tau)/L_{\max}(\tau)], \tag{5.9}$$

where $L_{\max}(\tau)$ is the maximised likelihood, is normally distributed [97]. Therefore, the 68.3% confidence interval $[\tau - u, \tau + u]$ found by solving $2\ln[L(\tau \pm u)/L_{\max}(\tau)] = \chi^2_{0.683,1}$ yields the standard uncertainty in the estimated value of τ.

5.3.1.3 Minimum variance unbiased estimator

If the data is instead treated as an exponentially distributed set of decay times $[t_1, \ldots, t_{N_T}]$, with probability density function given by equation 5.1, the log-likelihood may be written as

$$\ln[L(\tau; t_1, \ldots, t_{N_T})] = -N_T \ln(\tau) - \frac{1}{\tau} \sum_i t_i. \tag{5.10}$$

This expression may be maximised by requiring

$$\frac{\partial \ln[L(\tau; t_1, \ldots, t_{N_T})]}{\partial \tau} = \frac{N_T}{\tau^2} \left(\frac{\sum_i t_i}{N_T} - \tau \right) = 0. \tag{5.11}$$

yielding $\mu = \sum_i t_i / N_T$ as the maximum likelihood estimator for τ. It follows from equation 5.11 and the Crámer-Rao theorem [97] that with a variance of $\mathrm{Var}(\mu) = \tau^2 / N_T$, μ is the minimum variance unbiased estimator of τ. Therefore, the minimum variance unbiased estimator gives $\tau = \mu$ with standard uncertainty $\sigma_\tau = \tau / \sqrt{N_T}$.

5.3.2 Two-parameter model

The decay time data may also be modelled using a two parameter model in which the amplitude of the fitted exponential is allowed to vary. The expected number of decays in the ith bin is now modelled by

$$N(t_i, \tau, A) = A \exp\left(-\frac{t_i}{\tau} \right). \tag{5.12}$$

A weighted least squares fit, and the maximum likelihood estimate of τ

and A may again be performed as follows.

5.3.2.1 Weighted least-squares fit

The best fit value of τ and A are those which minimise the sum of the squared deviations of each data point from the fitted curve in terms of the error on each point.

$$\chi^2(\tau) = \sum_i \left(\frac{N(t_i, \tau, A) - N_i}{\sigma_i} \right)^2 \tag{5.13}$$

where $\sigma_i = \sqrt{N_i}$ is the standard uncertainty associated with N_i due to counting statistics.

As with the single parameter model, in order to satisfy the assumption that both N_i and σ_i are normally distributed, only the portion of the data set where $N_i > 10$ may be used.

The two dimensional confidence region containing within which there is a 68.3% of finding the actual values of τ and A is enclosed by the constant χ^2-boundary

$$\chi^2_{\text{bound}} = \chi^2_{\text{min}} + \chi^2_{0.683,2} \tag{5.14}$$

where χ^2_{min} is the minimised sum of weighted least squares (given by equation 5.13) and $\chi^2_{0.683,2}$ is the 68.3% point of a one-tailed chi-squared distribution with two degrees of freedom. The standard uncertainty in the fitted value of τ is found by projecting the two-dimensional confidence region onto the one dimensional parameter space of τ alone. This is shown in figure 5.1.

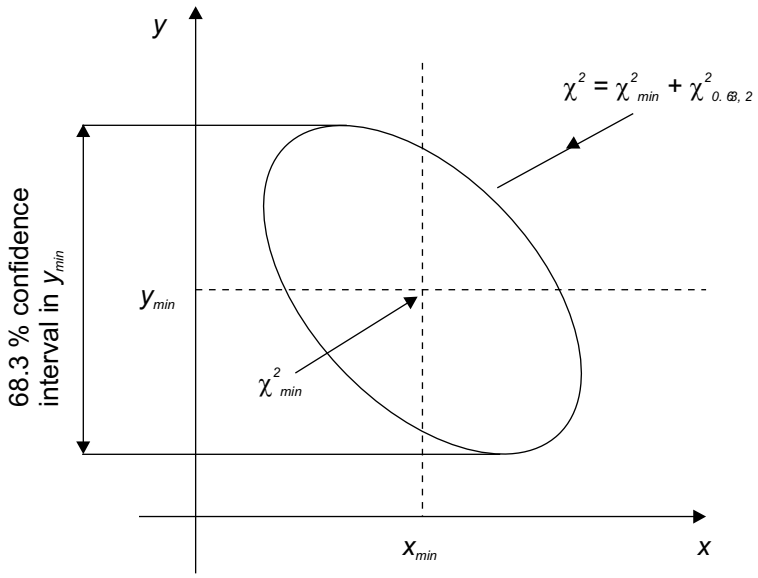

Figure 5.1: If a two parameters weighted-least squares fit is performed on parameters x and y, the standard uncertainty in the fitted value of y is given by the projection of confidence boundary $\chi^2_{bound} = \chi^2_{\min} + \chi^2_{0.683,2}$ onto the y-axis as shown.

5.3.2.2 Maximum likelihood estimator

Maximum likelihood estimates may also be made for τ and A, using a similar method to that described for the one parameter model in section 5.3.1.2. In this case however, the expected number of decays in the ith bin is given by

$$X_i = N(t_i, \tau) = A \exp(-t_i/\tau). \tag{5.15}$$

rather than equation 5.5. The best estimates of τ and A are the values which maximise the log-likelihood given by equation 5.7.

The normally distributed Wilk's likelihood ratio statistic (see equation 5.9) may be used to determine the 68.3% confidence region in τ and A. The boundary of this region satisfies the condition

$$2 \ln[L(\tau \pm u)/L_{\max}(\tau)] = \chi^2_{0.683,2} \tag{5.16}$$

where $L_{\max}(\tau)$ is the maximised log-likelihood and $\chi^2_{0.683,2}$ is the 68.3% point of a one-tailed chi-squared distribution with two degrees of freedom. The standard uncertainty in τ may then be found by projecting this confidence region onto the one-dimensional parameter space of τ alone as outlined in section 5.3.2.1.

5.3.3 Discussion of fitting and estimation techniques

Of the three methods using the single-parameter model to determine a value of τ from the experimental data, the minimum variance unbiased estimator is the simplest to calculate. This method whilst giving the estimate of τ with

smallest statistical uncertainty, relies on the validity of treating the data as an exponentially distributed set of decay times following equation 5.1 and provides no means to check this. The weighted least-squares method has the advantage that the residuals - the differences between the observed data and the fitted curve normalised by the standard error on each point, may be used as a measure of the goodness of fit of the data to the exponential form of equation 5.2. Due to the restriction that $N_i > 10$, a portion of the data must be rejected for the purposes of the least squares fitting procedure, in turn resulting in a larger uncertainty. While the maximum likelihood estimator is the most demanding of the three methods in terms of computation, all the data may be used resulting in a small statistical uncertainty in the resulting estimate of τ.

The two parameter model increases the complexity of the calculation required to determine the optimum value of τ, but offers an estimate free from small systematic errors introduced as a result of the finite duration of each bin and the time required to determine the state of the ion (see sections 5.6.5 and 5.6.6).

It should be noted that linearising the data, i.e. using the data set $(t_i, \ln(N_i))$, and fitting a straight line using a weighted least squares method is wholly inappropriate, since the logarithm does not preserve the normal distribution of uncertainties. A fitting procedure based on this linearised least-squares method will therefore introduce a bias in the fitted value of τ.

5.4 Apparatus

The data used for this measurement of the $^2D_{5/2}$ state lifetime was recorded over 3 days in May 2000 and 3 days in July 2002. Two different configurations of the apparatus described in chapter 3 was used over these two periods and will therefore be briefly described here.

Endcap trap 1 was used for both data sets. The UHV chamber in which the trap was housed was pumped only by a 40 ls^{-1} ion pump, resulting in a pressure of between $\sim 4 \times 10^{-10}$ and 1×10^{-9} torr.

5.4.1 May 2000 setup

During the May 2000 data sets, trap 1 was operated using the self-oscillating transistor trap drive described in section 3.3.1. Typical operating conditions of the trap were a drive frequency $\Omega_{RF}/2\pi = 13$ MHz, with a drive voltage amplitude of 300V, resulting in motional frequencies $(\omega_r, \omega_z) = (1.8,\ 3.0)$ MHz. The trap drive potential was produced by the self-oscillating transistor circuit described in section 3.3.1.

The cooling laser was stabilised only via the offset lock to the ^{85}Rb feature, with the higher frequency side-of-fringe stabilisation to the reference cavity not yet implemented. The probe laser system was stabilised to the ULE cavity using the Pound-Drever-Hall technique. However, the inner temperature servo for the ULE cavity used a DC bridge temperature monitor and the RF sideband for the Pound-Drever-Hall lock were generated by RF current modulation of the master laser diode current. These lasers would therefore have a larger linewidth and drift rate than is now the case. The beam di-

rections and typical powers of the cooling and repumper beams and also the weak probe beam were nominally the same as those described in chapter 3, with the intense probe beam not yet having been setup. Without the intense slave, the probe laser was configured to drive the $^2S_{1/2}$ – $^2D_{5/2}$ transition below saturation using the weak probe beam. All beams were switched using AOMs only. The experiment was also controlled by Visual BASIC software written by G. P. Barwood, rather than the LabVIEW routines described in section 3.10.

5.4.2 July 2002 setup

Following the data of May 2000, and prior to the data of July 2002, several improvements were made to the experimental apparatus. The LabVIEW [98] routines (see section 3.10) were installed and used to control the apparatus. The second slave laser was constructed, delivering 1.5 mW of radiation at 674 nm focused into a 30 μm ($2\omega_o$) spot at the ion. Mechanical shutters were installed in the laser beams, ensuring complete extinction of 674 nm light during the detection period. In addition, the spectral purity of the RF trap drive was improved through the use of the helical coil resonator.

In the July 2002 data, the intense slave laser was used at maximum intensity to drive the $^2S_{1/2}$ – $^2D_{5/2}$ transition and prepare the ion in the $^2D_{5/2}$ state. This yields a much larger percentage of attempts resulting in an ion shelved in the $^2D_{5/2}$ state. As a consequence, the time required to record a set number of shelved periods was reduced.

5.5 Results

Individual data sets were recorded for periods of around one hour. Before each data set was recorded, the ion's micromotion was verified to be minimum. In addition the probe laser was scanned across the $^2S_{1/2}$ – $^2D_{5/2}$ transition to verify the RF offset lock frequency required for the probe laser to be on resonance.

In the data recorded in May 2000 the weak probe beam was used below saturation to prepare the ion in the $^2D_{5/2}$ state. Between 2,000 and 5,000 decay times were recorded in each data set, and a total of 63,000 decay events were observed over the course of three days.

The various methods described in section 5.3 were all used to determine the lifetime of the $^2D_{5/2}$ state and its associated uncertainty. When using the single-parameter model, the weighted least-squares method gives a measured lifetime of 391.2(1.8) ms, the maximum likelihood estimator 392.2(1.6) ms, and the minimum variance unbiased estimator yields 391.8(1.6) ms, where the 1σ statistical uncertainties are given in parenthesis. These results are displayed in table 5.1. Figure 5.2(a) shows the decay times recorded in May 2000, with the exponential decay function of equation 5.2 fitted using the single parameter least-squares method. The residuals (the difference between the data points and the fit function normalised by the uncertainty in each point) are shown in figure 5.2(b). Shown in figure 5.3(a) is the exponential function corresponding to the maximum likelihood estimate of the lifetime, while (b) shows the least-squares residuals for this exponential decay. These residuals are not used in the maximum likelihood estimator method and are

shown only to illustrate that above decay times of 2000 ms, where the number of decay events recorded in each bin falls below 10, the residuals begin to show structure and are clearly no longer normally distributed. As such, they cease to be a good measure of the departure of the data from the fitted function. This highlights the necessity of removing theses data points when using the least-squares fitting method.

When using the two-parameter model, the weighted least-squares method gives a lifetime of 391.1(1.8) ms and the maximum likelihood estimator gives 392.2(1.6) ms. The confidence regions in the values of τ and A from the weighted least-squares fit and the maximum likelihood estimate are shown in figure 5.4.

The July 2002 data, also recorded over three days, used the intense probe beam to prepare the ion in the $^2D_{5/2}$ state. With the intense probe, the ion may be prepared in the $^2D_{5/2}$ state with high probability, by coherently driving the $^2S_{1/2} - {}^2D_{5/2}$ transition (see chapter 6). As a result, between 10,000 and 14,000 decay times were recorded in each data set and over the course of three days a total of 97,000 decay times were recorded. The data is analysed using the fitting/estimation techniques described in section 5.3. When using the single-parameter model, the weighted-least squares gives a measured lifetime of 388.6(1.4) ms, the maximum likelihood estimator 389.9(1.3) ms and the minimum variance unbiased estimator 389.9(1.3) ms with the 1σ statistical uncertainties being the figures in parenthesis. These results are also displayed in table 5.1 for comparison.

The weighted least-squares fit to the July 2002 data is shown in figure 5.5(a) with the residuals of this fit shown in figure 5.5(b). Figure 5.6(a)

	Fitted Lifetime, τ /ms	Decay Rate /s^{-1}
May 2000 Data		
Single-parameter model:		
Weighted Least-Squares Fit	391.2 ± 1.8	2.556 ± 0.012
Maximum Likelihood Estimator	392.2 ± 1.6	2.550 ± 0.010
Min. Var. Unbiased Estimator	391.8 ± 1.6	2.552 ± 0.010
Two-parameter model:		
Weighted Least-Squares Fit	391.1 ± 1.8	2.557 ± 0.012
Maximum Likelihood Estimator	392.2 ± 1.6	2.550 ± 0.010
July 2002 Data		
Single-parameter model:		
Weighted Least-Squares Fit	388.6 ± 1.4	2.573 ± 0.009
Maximum Likelihood Estimator	389.9 ± 1.3	2.564 ± 0.009
Min. Var. Unbiased Estimator	389.9 ± 1.3	2.565 ± 0.009
Two-parameter model:		
Weighted Least-Squares Fit	388.6 ± 1.4	2.573 ± 0.009
Maximum Likelihood Estimator	389.9 ± 1.3	2.565 ± 0.009

Table 5.1: Lifetimes and corresponding decay rates of the $^2D_{5/2}$ state determined from the May 2000 data and July 2002 data using the weighted least-squares fit, maximum likelihood estimator and minimum variance unbiased estimator with the single-parameter model and the weighted least-squares fit and maximum likelihood estimator with the two-parameter model.

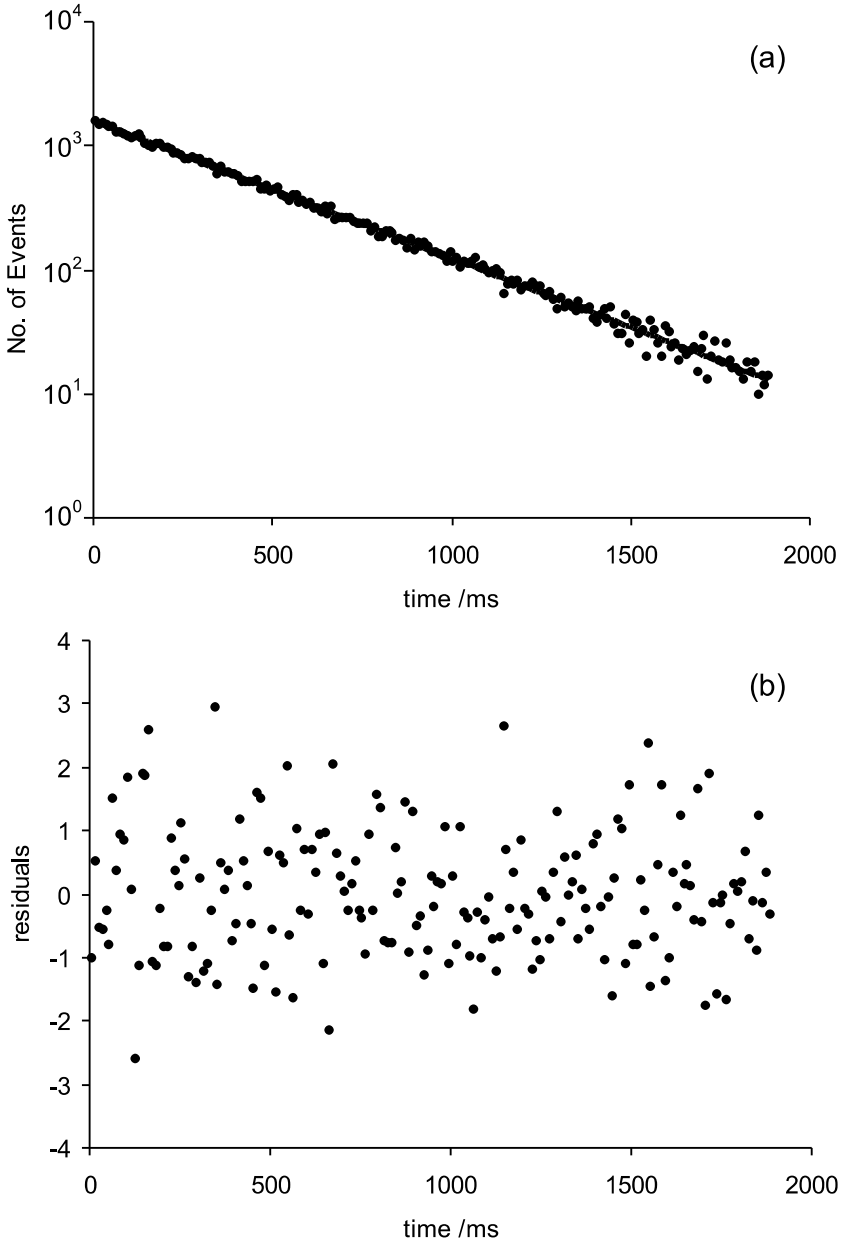

Figure 5.2: Weighted least squares fit to May 2000 data consisting of 63,000 shelved periods. Shown in (a) are the number of shelved periods N_i in each 10 ms bin at time t_i while the residuals i.e. $\big(N(t_i,\tau) - N_i\big)/\sqrt{N_i}$ are shown in (b).

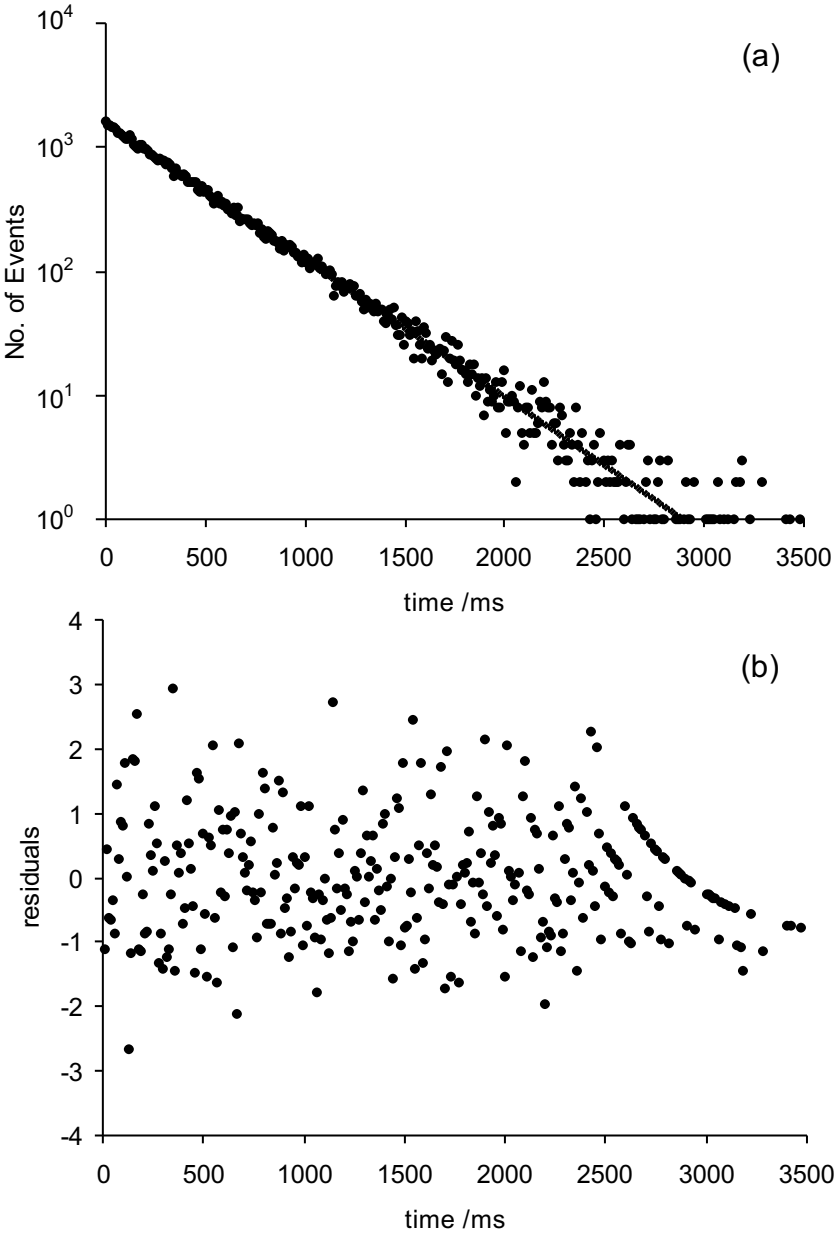

Figure 5.3: Exponential decay curve of maximum likelihood estimate of τ from May 2002 data of 63,000 shelved periods. Shown in (a) are the number of shelved periods N_i in each 10 ms bin at time t_i. For comparison with the least-squares method, $\big(N(t_i,\tau) - N_i\big)/\sqrt{N_i}$ is shown in (b), although these least-squares fitting residuals are not used in the maximum likelihood estimator. These residuals are clearly not normally distributed for $t_i > 2000$ ms demonstrating the need to remove these data points from a least-squares fit.

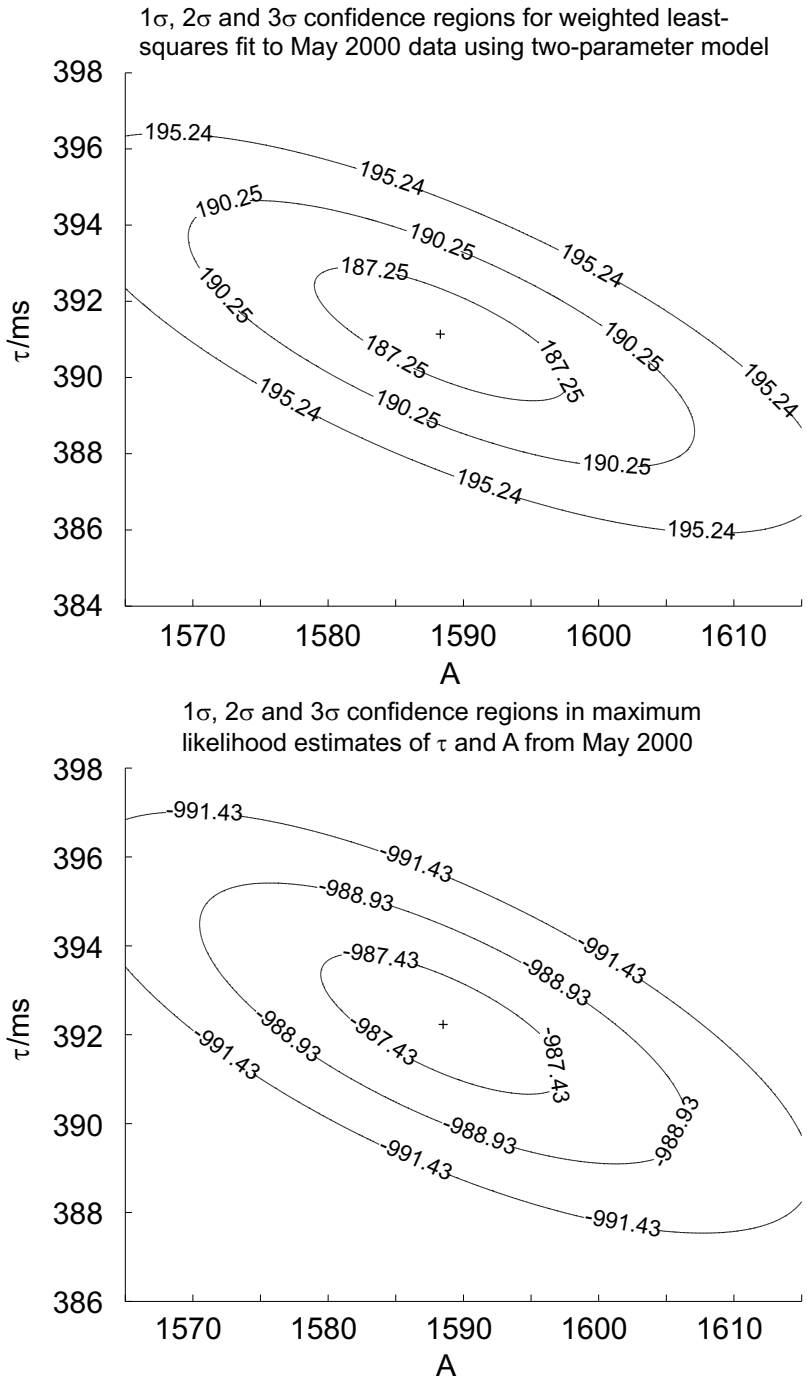

Figure 5.4: Confidence regions in results of weighted least-squares fit and maximum likelihood estimator. The confidence interval in τ is given by the projection of these regions on to the vertical axis.

shows the July 2002 data along with the exponential decay function corresponding to $\tau = 390.0$ ms as determined by the maximum likelihood estimator. Shown in figure 5.6(b) are the least-squares residuals for this exponential decay. Once again, these residuals are not used in the maximum likelihood estimator method and are shown only to illustrate that as the number of decay events recorded in each bin falls below 10, the residuals are clearly no longer normally distributed and cease to be a good measure of the departure of the data from the fitted function.

With the two-parameter model, the weighted least-squares method gives a lifetime of 388.6(1.4) ms and the maximum likelihood estimator gives 389.9(1.3) ms. The confidence regions in the values of τ and A from the weighted least-squares fit and the maximum likelihood estimate are shown in figure 5.7.

The results of the different methods for determining the $^2D_{5/2}$ state lifetime τ shown in table 5.1 do no yield exactly the same value, however it is important to note that all values agree to within the 1σ level of statistical uncertainties. This is also the case for the July 2002 data. There does not appear to be any statistically significant systematic shift between then results yielded by the different methods for determining τ for either of the two sets of data.

For both sets of data, a measured value of τ is determined by taking the mean of the values give by the two-parameter model weighted least squares fit and maximum likelihood estimator, as these methods are not skewed by systematic uncertainties in the decay time of each event (see sections 5.6.5 and 5.6.6). Symmetric 1σ uncertainty bounds in the measured value of τ are

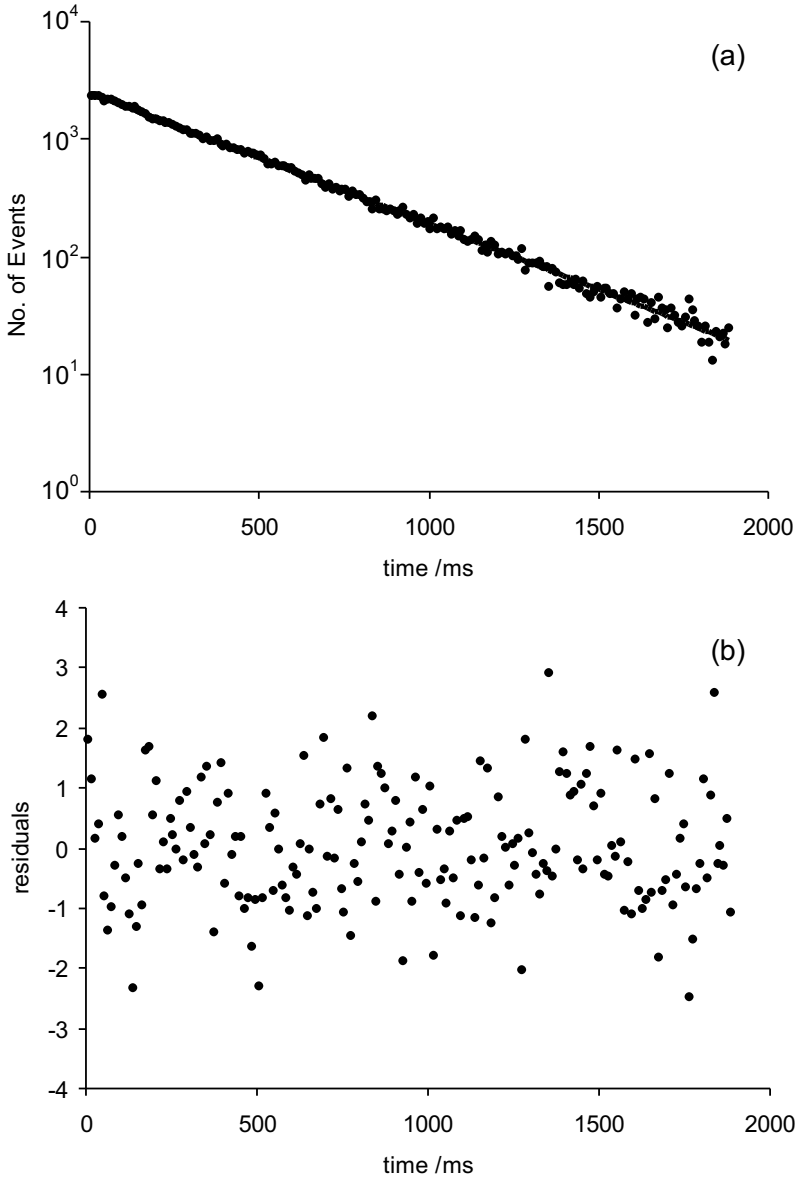

Figure 5.5: Weighted least squares fit to July 2002 data consisting of 97,000 shelved periods. Shown in (a) are the number of shelved periods N_i in each 10 ms bin at time t_i while the residuals i.e. $\big(N(t_i,\tau) - N_i\big)/\sqrt{N_i}$ are shown in (b).

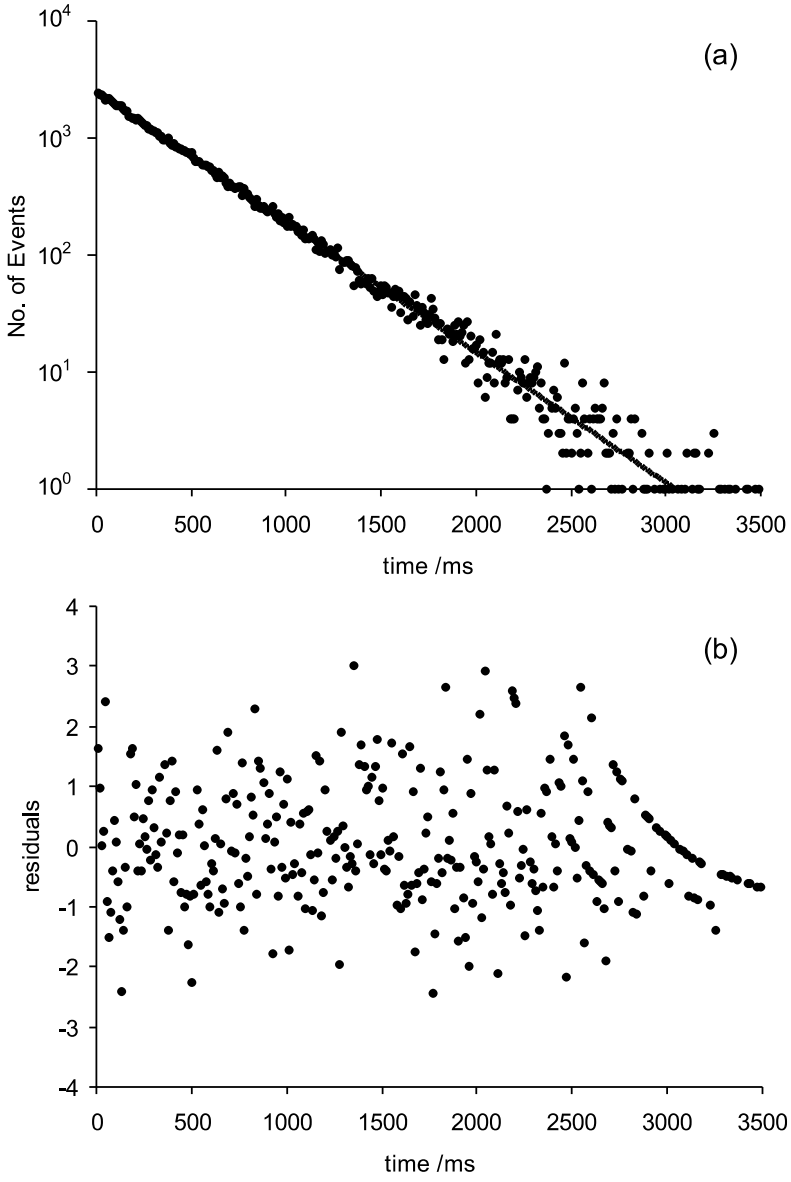

Figure 5.6: Exponential decay curve of maximum likelihood estimate of τ from July 2002 data of 97,000 shelved periods. Shown in (a) are the number of shelved periods N_i in each 10 ms bin at time t_i. For comparison with the least-squares method, $\big(N(t_i,\tau) - N_i\big)/\sqrt{N_i}$ is shown in (b), although these least-squares method residuals are not used in the maximum likelihood estimator method.

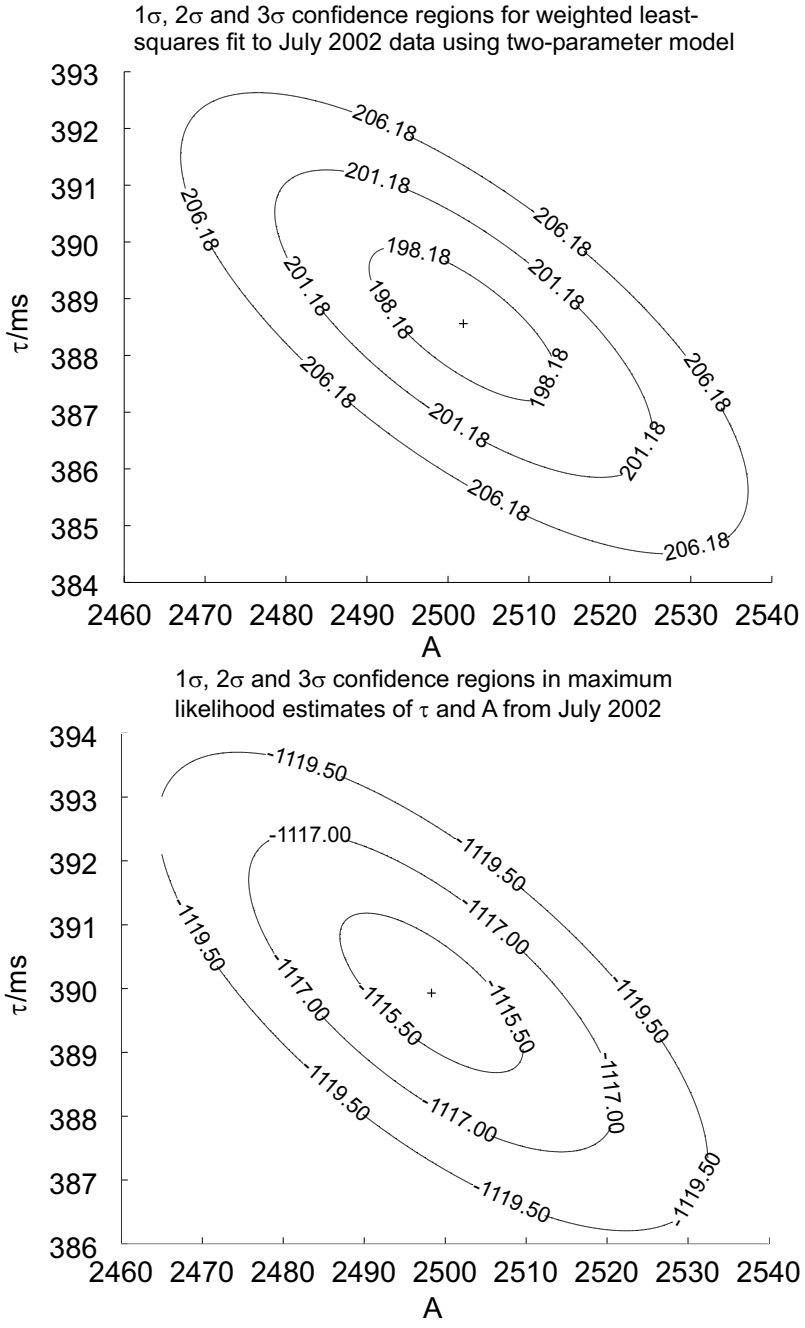

Figure 5.7: Confidence regions in results of weighted least-squares fit and maximum likelihood estimator. The confidence interval in τ is given by the projection of these regions on to the vertical axis.

chosen so as to include the 1σ uncertainty intervals of each of the constituent values. This yields measured values of 391.7(2.4) ms for the May 2000 data and 389.3(2.1) ms for the July 2002 data, and corresponding measured decay rates of 2.553(0.016) s^{-1} and 2.569(0.014) s^{-1} respectively.

5.6 Systematic Effects

The decay rates determined in section 5.5 are the total decay rates of the $^2D_{5/2}$ state determined for each data set and include not only the radiative decay rate, but also rates associated with other decay channels such as collisional decays. As such, the quoted decay rates must be corrected for these and any other systematic effects to find the radiative decay rate and the corresponding natural lifetime of the $^2D_{5/2}$ state. The recent measurement of the 3d $^2D_{5/2}$ state lifetime in $^{40}Ca^+$ also using a single trapped ion [99] has given extensive consideration to the systematics associated with this type of measurement. The relevant systematic effects, and their relative importance, are now discussed.

5.6.1 Collisional effects

During a collision with a background gas molecule, the ion may gain significant kinetic energy (i.e. be heated) or may change its electronic state. In the first case, where the ion is heated, it may become Doppler-shifted out of resonance with the cooling transition, leading to a drop in florescence. In the July 2002 data, on occasion, the fluorescence was observed to disappear abruptly and return slowly over the time scale of a few hundred milliseconds.

This was attributed to such collisions, where the ion is quickly heated out of resonance and then is slowly Doppler-cooled back into resonance again. This phenomenon was not observed in the data of May 2000. This therefore suggests that the background pressure in the UHV chamber was greater during July 2002 than May 2000. Ion gauge readings also indicate that the background pressure had risen slightly over the period between May 2000 and July 2002.

In the data of July 2002, it is estimated that around 8 collisions per hour, where the fluorescence recovers slowly, were observed. These observed events were discarded, since the gradual return of fluorescence could result in several false decays being recorded as the signal crossed the threshold. The rate of 8 collisions per hour, or 2.2 $\times 10^{-3}$ s^{-1} is assumed as an upper limit to the rate of collisional decay. Barton *et al.* [99] discuss a similar approach in estimating this rate. Each interrogation was allowed to proceed only after an appropriate count rate has been detected, thus ensuring that the ion is properly cooled.

5.6.2 Off-resonant quenching by the repumper laser

When the ion is shelved in the $^2D_{5/2}$ state, any radiation driving the $^2D_{5/2}$ – $^2P_{3/2}$ transition at 1033 nm may return the ion to the electronic ground state via the $^2P_{3/2}$ state (see figure 2.1). Since the cooling laser and repumper laser must both be incident on the ion during the shelved period, one possible source of quenching is off-resonant excitation of the $^2D_{5/2}$ – $^2P_{3/2}$ transition at 1033 nm by the far-detuned repumper laser at 1092 nm. The repumper

laser has a typical power of 4 mW and is directed onto the ion in a $2\omega_0 = 600$ μm spot. Following the analysis by Barton *et al.* [99], the deshelving rate R is given by

$$R = \frac{2J_P + 1}{2J_D + 1} \frac{\pi^3 c^3}{\hbar \omega_{PD}^3} A_{PD} \frac{I}{c} g(\omega_L - \omega_{PD}) \tag{5.17}$$

where J_P and J_D are the total angular momenta of the $^2P_{3/2}$ and $^2D_{5/2}$ states respectively, ω_{PD} is the angular frequency of the $^2D_{5/2}$ – $^2P_{3/2}$ quenching/clearout transition at 1033 nm, ω_L is the angular frequency of the repumper laser and $g(\omega_L - \omega_{PD})$ is the normalised transition lineshape function. It is assumed that the lineshape is Lorentzian, with

$$g(\omega_L - \omega_{PD}) = \frac{\Gamma_P / 2\pi}{(\omega_L - \omega_{PD})^2 + \Gamma^2/4} \tag{5.18}$$

where Γ_P is the decay rate of the $^2P_{3/2}$ level (over all decay channels). Using the P-D decay rate $A_{PD} = 8.7 \times 10^6$ s^{-1} gives an upper deshelving rate of 6×10^{-4} s^{-1}.

The recent measurement of the 3d $^2D_{5/2}$ state lifetime in $^{40}Ca^+$ [99] demonstrated that background emission from the analogous repumper laser (at 866 nm) was able to quench the $^2D_{5/2}$ state by excitation of the $^2D_{5/2}$ – $^2P_{3/2}$ transition at 854 nm. This led to a significant shortening of the measured lifetime. The quenching of the $^2D_{5/2}$ state by the repumper laser in this work was particularly pronounced due to the broad spectral output of the diode laser used, which extended several nanometres from the lasing wavelength. This background is due to the high gain in these devices.

The analogous effect in $^{88}Sr^+$ would be the presence of 1033 nm radiation in the output of the repumper laser. As described in section 3.7, this laser is

a Nd^{3+}-doped fibre laser. This type of laser is incapable of lasing at 1033 nm having a tuning range of 1070 nm – 1140 nm [100]. The spectral output of the repumper laser has also been examined using an optical spectrum analyser. No significant evidence of radiation at 1033 nm above the noise floor of the instrument was detected (∼60 dB down from the peak emission). It is informative to note that in the $^{40}Ca^{+}$ work, the background was easily detectable.

5.6.3 Quenching by blackbody radiation

Blackbody radiation is another source of light at 1033 nm which may lead to quenching of the $^2D_{5/2}$ state. The rate of deshelving from the 4d $^2D_{5/2}$state is given by $(1-b)B_{DP}\rho(\omega_{PD})$, where b is the branching ratio from the 5p $^2P_{3/2}$ state, $\rho(\omega_{PD})$ is the spectral energy density in the blackbody radiation, ω_{PD} is the transition frequency, and the subscripts D and P denote the relevant atomic states. The Einstein B-coefficient is given by $B_{DP} = (g_P\pi^2c^3A_{PD})/(g_D\hbar\omega_{PD}^3)$, therefore the deshelving rate becomes

$$(1-b)\frac{2J_P+1}{2J_D+1}A_{PD}\frac{1}{\exp(\hbar\omega_{PD}/k_BT)-1} \tag{5.19}$$

At room temperature, this leads to a quenching rate of 10^{-14} s^{-1}, which is negligible compared to the decay rate being measured.

Illumination of the ion by a higher temperature source such as a tungsten-filament lamp or ion gauge filament could result in a deshelving rate which is no longer negligible. In the apparatus used for this measurement however, the vacuum windows are shielded from room lights in order to reduce the

background photons detected by the photomultiplier and the ion gauge was not in operation. In addition, there are no tungsten-filament lamps in use, therefore deshelving due to thermal radiation is insignificant.

5.6.4 Residual 674 nm radiation

A further possible source of systematic uncertainty existed in the May 2000 set of data. In that experiment, no mechanical shutter was used to ensure total extinction of the 674 nm probe beam: only an acousto-optic modulator was used. Despite the extinction ratio being around 1 part in 2000, there is a possibility that some of the 674 nm light leaking through the AOM could drive the ion back to the ground state. However, the data of May 2000 was recorded with the probe laser well below saturation. This possible source of systematic error was removed in the July 2002 data. Had this been a significant systematic error in the May 2000 data, then the result of the July 2002 data would have exhibited a larger measured lifetime than the May 2000 data.

5.6.5 Effect of binning

The effect of determining the decay time of each shelved period only to within the time interval corresponding to one bin leads to a negligible systematic error when the single-parameter model is used to determine τ, and no systematic error when the two parameter model is used. This may be shown as follows.

From equation 5.1, it is to be expected that if a total of N_T decay events

are measured, the number of events expected to occur during the ith bin of duration t_d centred around a time t_i is

$$N_e(t_i) = \int_{t_i-\frac{1}{2}t_d}^{t_i+\frac{1}{2}t_d} \frac{N_T}{\tau} \exp\left(-\frac{t}{\tau}\right) \mathrm{d}t \tag{5.20}$$

$$= N_T \exp\left(-\frac{t_i}{\tau}\right)\left[\exp\left(\frac{t_d}{2\tau}\right) - \exp\left(-\frac{t_d}{2\tau}\right)\right] \tag{5.21}$$

which to third order in t_d/τ is

$$N_e(t_i) = N_T \frac{t_d}{\tau} \exp\left(-\frac{t_i}{\tau}\right)\left(1 + \frac{t_d^2}{24\tau^2}\right). \tag{5.22}$$

When compared with the single-parameter model of equation 5.2, it can be seen that the exponential fitted to the data has the same slope as equation 5.22, and differs only in amplitude by $(1 + t_d^2/24\tau^2)$ which for the values of t_d and τ in this work is a negligible difference of less than 0.003%.

When using the two-parameter model, the amplitude of the exponential is left as a free parameter and so there is no systematic due to the binning process.

5.6.6 Attributing quantum jumps to the wrong bin

Consider an ion which decays from the excited state a short time δ_t before the end of a bin. If a count rate R_S is detected when the ion is no longer shelved, only a small amount of fluorescence, $\delta_t R_S$ above the background will be counted before the end of the bin. If δ_t is short enough, this will be below T the threshold number of counts (see section 4.6.1) and the ion will be assumed to have not decayed in this bin. Instead, the decay time will

attributed to the next bin.

If all decay events occurring within a time ϵ of the end of a bin are attributed to the next bin, according to the single-parameter model of 5.1 the number of events expected in each bin is

$$N_e(t_i) = \int_{t_i-\frac{1}{2}t_d-\epsilon}^{t_i+\frac{1}{2}t_d-\epsilon} \frac{N_T}{\tau} \exp\left(-\frac{t}{\tau}\right) \mathrm{d}t \tag{5.23}$$

$$= N_T \frac{t_d}{\tau} \exp\left(-\frac{t_i}{\tau}\right) \exp\left(-\frac{\epsilon}{\tau}\right) \tag{5.24}$$

neglecting the higher order terms in t_d/τ which have already been shown in section 5.6.5 to be negligible. To first order in ϵ/τ, the amplitude of this function differs from the single-parameter model of equation 5.2 by a factor $(1+\epsilon/\tau)$, while the time constants of the exponential parts of the functions are equal.

If a count rate of 15,000 s^{-1} is detected when the ion is fluorescing and a background of 1,000 s^{-1} is detected when the ion is shelved in the $^2\mathrm{D}_{5/2}$ state, for a bin duration of 10 ms, it should be expected that $\epsilon \sim 2$ ms. This in turn means that the amplitude of the fitted function may be different to that of the data by $\sim$0.5%. For the fitting and estimation methods using the single-parameter models, it is difficult to estimate the resulting systematic in the determined values of τ since both the time constant and amplitude of the fitted exponential are dependent on τ.

If the τ is chosen so that the amplitude of the exponential function fits the data well, the time constant of the exponential will be too large (on a logarithmic plot, the slope of the function will be too steep). If on the other hand, τ is chosen so that the slope of the exponential fits that of the data, it

should be expected that the amplitude of the exponential will be too large. As a result, the optimal value of τ determined unsing the single-parameter model must lie between these two extremes. The determined value of τ must then be within 0.5% of the actual value of τ associated with the data.

When using the two-parameter model, this systematic is again not present, since the amplitude of the exponential decay curve is a free parameter and the value of τ is determined from the decay time constant of the data only.

5.6.7 Discussion

The most significant systematic effects are therefore considered to be the effect of collisions and of off-resonant excitation out of the $^2D_{3/2}$ state by the 1092 nm laser. Both effects serve to reduce the measured decay rate. These effects are not directly measurable in our apparatus, however the magnitude of each has been estimated. An uncertainty exists in these estimates, therefore the uncertainty introduced by each systematic is set to the upper limit of the effect as quoted above.

Table 5.2 shows the measured decay rates, together with the rates associated with the systematic effects described in the previous section. Both measurements were corrected for systematic effects and an uncertainty was calculated based on those shown in table 5.1. Taking the weighted mean of the results shows that the value for the lifetime measured in this experiment is 390.3(1.6) ms where the uncertainty is the 1σ error.

	May 2000 Rates /s^{-1}	July 2002 Rates /s^{-1}
Measured Rate	2.553 ± 0.016	2.569 ± 0.014
Systematic effect		
Collisional deshelving	2.2×10^{-3} ± 2.2×10^{-3}	2.2×10^{-3} ± 2.2×10^{-3}
Off-resonant excitation of $^2D_{5/2}$ –$^2P_{3/2}$ transition	6×10^{-4} ± 6×10^{-4}	6×10^{-4} ± 6×10^{-4}
Corrected (Radiative) Decay Rate	2.550 ± 0.016	2.569 ± 0.014

Table 5.2: Measured decay rate of the $^2D_{5/2}$ state, decay rates due to non-radiative decay mechanisms and corrected, radiative decay rate of the $^2D_{5/2}$ state.

5.7 Discussion

The result of τ = 390.3(1.6) ms is compared with other measured and calculated values in figure 5.8, which quotes the corresponding 1σ uncertainty where possible [101, 102, 103].

In comparing the different experimental results, it is helpful to consider some of the salient features of the various experiments. The work of Gerz et al [94], was conducted using a cloud of ions in an r.f. trap. This experiment was performed at pressures in the range $\sim3\times20^{-8}$ to 1.5×10^{-6} mbar, and the result of 345(33) ms was determined by extrapolating to zero pressure.

The result of Madej and Sankey [79] was not limited by collisional de-excitation, being performed at a pressure of 4×10^{-10} mbar. In that work, the ratio of shelved to unshelved periods in a single trapped ion was used to determine the $^2D_{5/2}$ state lifetime. This method is dependent on both

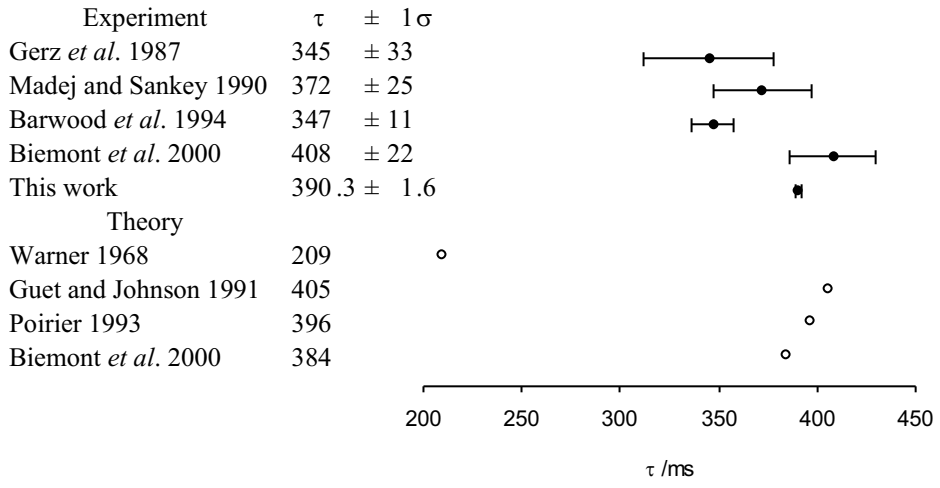

Figure 5.8: Previous measurements and calculations of the natural lifetime of the 4d $^2D_{5/2}$ state. Measured values are shown as filled circles with 1σ uncertainty error bars and calculated values shown as open circles.

the power of the 422 nm cooling laser as well as the power of the excitation laser at 674 nm. The laser powers were varied to extract the lifetime of 372(25) ms. The result of Barwood *et al.* of 347(33) [95] (the uncertainty quoted is 3σ [102]) was performed in the same fashion as the work reported in this paper, however it was only based on only 5120 observed decays.

More recently, the lifetime has been measured using an ion storage ring [86]. The result of 408(22) ms is arrived at after correcting for a beam loss rate of 0.21 s^{-1} and a collisional loss rate of 0.23 s^{-1}: note that these corrections are both around 10% of the radiative decay rate. It is also interesting to note that the lifetime of the $^2D_{3/2}$ state has been measured using the same laser probing technique, as well as with a separate optical pumping technique. The results for the $^2D_{3/2}$ state lifetime are: 455(29) ms measured using the former

method, and the smaller value of 435(4) ms measured using the latter [86].

The result 390.3(1.6) ms determined in this work is in agreement with the results of Madej and Sankey [79] and Biémont et al [86] at the level of one standard uncertainty. The large amount of data recorded in this work yields an uncertainty over an order of magnitude more accurate than all other experimental investigations. The theoretical calculation of Poirier (396ms) [93] is closest to the measurement presented here.

5.8 Summary and Conclusion

This paper has described a measurement of the 4d $^2D_{5/2}$ metastable state of $^{88}Sr^+$ natural lifetime using a single laser-cooled ion confined in an RF trap. This measurement has been performed on two separate occasions under slightly different experimental configurations. The measured value of 390.3(1.6) ms agrees with other experimental results and is an order of magnitude more accurate than previous measurements. The most significant source of error in the final value is statistical rather than systematic.

Chapter 6

Coherent excitation on the quadrupole transition

6.1 Introduction

This chapter describes the coherent manipulation of the electronic state of the Doppler-cooled ion by driving the $^2S_{1/2}$ ($m_j = -1/2$) – $^2D_{5/2}$ ($m_j = -1/2$) Zeeman component of the quadrupole transition. Coherent Rabi oscillations are observed on both the carrier and sidebands of the transition. The oscillations exhibit a decaying contrast over time. This decay is the result of two different effects. The first is decoherence, attributed mainly to the finite probe laser linewidth. The second effect is an apparent damping due to the ion's distribution over motional states of the trap. The different motional states of the ion have different Rabi frequencies with the probe laser (see section 2.4.2). This leads to a dephasing between contributions from each of the ion's motional states and a washing out of the observed Rabi oscillation.

Since the dependence of the Rabi frequency on the ion's motional state is weaker on the carrier component than the sidebands, the contrast of Rabi oscillations on the carrier decays more slowly.

As the loss of contrast is dependent on the motional state of the ion, the mean motional quantum number after Doppler-cooling may be determined from the observed Rabi oscillations. This is an invaluable tool for optimising the Doppler-cooling process.

The contrast of the Rabi oscillations is an important figure of merit for the implementation of the Cirac and Zoller proposal for an ion trap quantum computer [16]. The fidelity of electronic state and motional state manipulations using the probe laser is given by the contrast of the oscillations on the carrier and sidebands respectively.

6.2 Investigations of coherent excitation on the quadrupole transition in trap 1

The first investigations of coherent excitation of the quadrupole transition using the intense probe laser were made using trap 1. Figure 6.1 shows Rabi oscillations observed in December 2001. The ion was Doppler-cooled using cooling beam 3 at a power of 4.2 μW and the probe laser tuned to line centre of the $^2S_{1/2}$ ($m_j = -\frac{1}{2}$) – $^2D_{5/2}$ ($m_j = -\frac{1}{2}$) carrier transition. The interrogation pulse duration was varied from 0 to 12 μs in steps of 100 ns. The intense probe beam power was 1.5 mW and 400 interrogations were made at each different pulse duration.

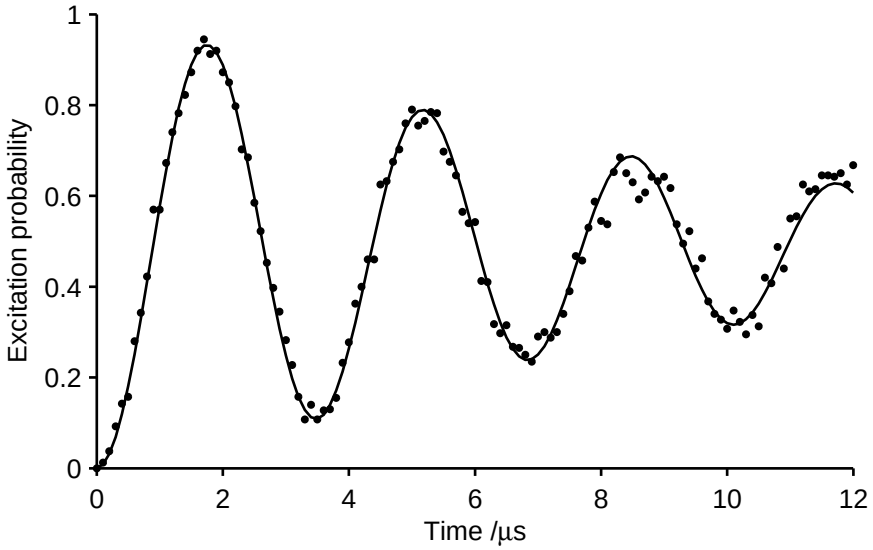

Figure 6.1: Rabi oscillations of the $^2D_{5/2}$ state population observed when the $^2S_{1/2}$ ($m_j = -1/2$) – $^2D_{5/2}$ ($m_j = -1/2$) carrier transition is driven. Each data point is the result of 400 interrogations.

Since the radial secular frequencies are almost degenerate, a two dimensional basis set of motional states consisting of an axial motion and a radial motion is chosen. In this model, the ion's motional state is described by $|n_z, n_r\rangle$. From equation 2.23, the Rabi frequencies on the carrier may therefore be written as

$$\Omega_{(n_r,n_z),(n_r,n_z)} = \Omega_0 e^{-\eta_r^2/2} L_{n_r}(\eta_r^2) e^{-\eta_z^2/2} L_{n_z}(\eta_z^2) \tag{6.1}$$

where η_r and η_z are the radial and axial Lamb-Dicke parameters (see section 2.4.2), Ω_0 is the free atom Rabi frequency and L_m is the mth order Laguerre polynomial. The observed Rabi oscillations may be modelled by summing the solutions to equations 2.18 and 2.19 over the motional states

n_r and n_z with the appropriate weight given by $P_{n_r}(\bar{n}_r)P_{n_z}(\bar{n}_z)$ the probability distribution of a thermal state of mean vibrational quantum numbers $\bar{n}_r$ and $\bar{n}_z$ (see equation 2.28). This approach is however computationally intensive. For the purpose of fitting a curve to the data, where the computation time required to produce the large number of solutions as fit parameters are varied is too great, an alternative, computationally simpler approach is adopted. In this method, the excitation probability, P_D as a function of the pulse duration is approximated by superposing pure sinusoidal solutions of Rabi frequency $\Omega_{(n_r,n_z),(n_r,n_z)}$ for each motional state and assuming that each of these solutions is damped with the same decoherence rate γ as follows [84]

$$P_D(t) = \frac{A}{2}\left(1 - e^{-\gamma t}\sum_{n_r,n_z} P_{n_r}(\bar{n}_r)P_{n_z}(\bar{n}_z)\cos\left(\Omega_{(n_r,n_z),(n_r,n_z)}t\right)\right). \qquad (6.2)$$

The term A is the fidelity with which the ion is prepared in the $^2\mathrm{S}_{1/2}$ ($m_j = -\frac{1}{2}$) Zeeman sublevel before the atom is driven on the quadrupole transition i.e. the optical pumping efficiency. The decoherence rate γ accounts for decoherence mechanisms such as the finite coherence time of the driving field. Equation 6.2 is fitted to the data using a maximum likelihood method [97] assuming the binomial statistics of quantum projection noise [104] in the measurement of population in the $^2\mathrm{D}_{5/2}$ state. It is assumed that the radial and axial modes of motion are equally well cooled, meaning that

$$E_{\mathrm{Doppler}} = \hbar\omega_z\left(\bar{n}_z + \frac{1}{2}\right) = \hbar\omega_r\left(\bar{n}_r + \frac{1}{2}\right). \qquad (6.3)$$

Given the axial and radial motional frequencies in trap 1 of $\omega_z/2\pi$ = 2.3 MHz and $\omega_r/2\pi = 1.6$ MHz, the resulting fit yields mean radial and axial motional quantum numbers of $\bar{n}_r = 48$ and $\bar{n}_z = 33$ and a decoherence rate of $\gamma/2\pi = 0.25$ kHz. It should be noted that the fitted value of γ has a large associated uncertainty and cannot be used to accurately establish the probe laser linewidth. The fit is shown as the solid line in figure 6.3. This should be compared with the Doppler limit of $\bar{n}_r = 3.9$ and $\bar{n}_z = 3.4$ (calculated using equation 2.30). This clearly indicates that the ion was not well Doppler cooled, probably due to an anomalous heating rate in trap 1.

6.2.1 Onset of unstable behaviour in trap 1

Over the period between December, 2001 and June, 2002, the contrast of coherent oscillations on the carrier transition decreased even further. By the end of June 2002, the contrast of the observed coherent oscillations appeared to be varying on a time scale of $\sim$ 5 minutes. This was approaching the time taken to acquire coherent excitation data. The micromotion had also become progressively harder to compensate, with an increase in the drift rate of the required compensation voltages. This behaviour was similar to that described by DeVoe *et al.*in $^{137}Ba^{+}$ microtraps [55]. DeVoe *et al.* ascribed these observations to high trap heating rates caused by contact potentials between the endcap electrodes and impurities sputtered onto them during the trap loading process.

Attempts were made to 'clean' the impurities from the electrode structure of the trap. The first method used was that of 'high potting'. A high

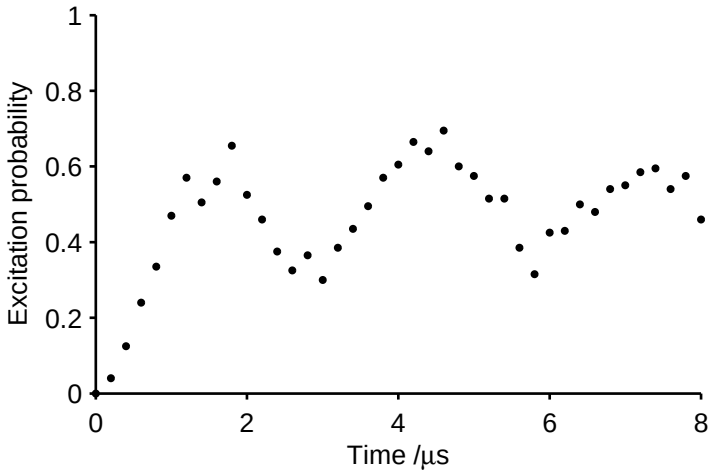

Figure 6.2: Rabi oscillations observed on the $^2S_{1/2}$ ($m_j = -1/2$) – $^2D_{5/2}$ ($m_j = -1/2$) carrier transition is driven. Each data point is the result of 200 interrogations. The low contrast of the Rabi oscillations implies that the ion is very poorly cooled.

voltage source was connected across the inner and outer endcaps and gradually increased from 0 V to 520 V. As the voltage was increased above 400 V, spikes were observed in the current flowing across the inner and outer endcaps indicating arcing. These events were accompanied by a rise in pressure observed at the ion pump. This process was applied to both the upper and lower endcaps. However, this method proved unsuccessful in cleaning the trap sufficiently to enable high contrast Rabi oscillations to be observed.

A second attempt to clean the electrode structure was made using an Ar^+ ion laser. A beam from this laser was directed through the large re-entrant window of the vacuum chamber onto each of the trap electrodes in turn. The power in the beam was slowly increased until a rise in pressure was observed at the ion pump. The highest power used was a total of 4 W.

Unfortunately, this process caused some form of damage to the trap,

leading to an intermittent RF short between the inner electrodes and one of the outer electrodes. As a result, it was impossible to continue to use trap 1 and trap 2 was constructed (see section 3.2.2).

6.3 Coherent excitation of a Zeeman component of the quadrupole transition in trap 2

Once trap 2 had been constructed and single ions successfully trapped, investigations of coherent excitation on the $^2S_{1/2}$ ($m_j = -1/2$) – $^2D_{5/2}$ ($m_j = -1/2$) Zeeman component of the quadrupole transition were carried out. It should be noted that trap 2 has higher motional frequencies than trap 1, with $\omega_r/2\pi = 2.2$ MHz and $\omega_z/2\pi = 3.8$ MHz.

6.3.1 Coherent excitation of the carrier component

The ion was interrogated using the intense probe beam at a power of 1.5 mW and tuned to line centre of the $^2S_{1/2}$ ($m_j = -1/2$) – $^2D_{5/2}$ ($m_j = -1/2$) carrier transition. The Rabi oscillations observed when the interrogation pulse duration is varied from 0 to 45 μs in steps of 100 ns are shown in figure 6.3. Each data point in the figure is the result of 400 interrogations. These oscillations were of higher contrast than those previously observed under similar conditions in trap 1.

Repeating the fitting procedure described in section 6.2 yields mean radial and axial motional quantum numbers of $\bar{n}_r = 14$ and $\bar{n}_z = 8$, a decoherence

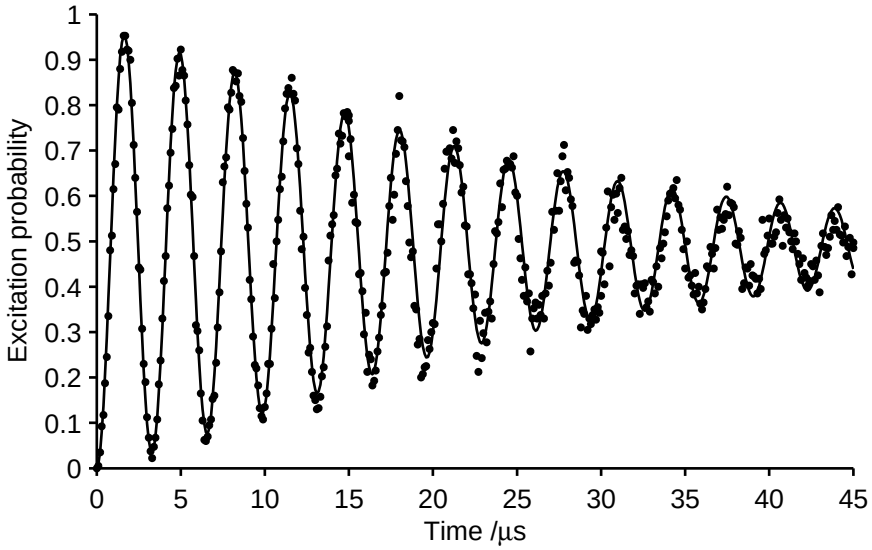

Figure 6.3: Rabi oscillations of the $^2D_{5/2}$ state population when the $^2S_{1/2}$ ($m_j = -1/2$) – $^2D_{5/2}$ ($m_j = -1/2$) carrier transition is driven. Each data point is the result of 400 interrogations.

rate of $\gamma/2\pi = 0.46$ kHz and Rabi frequency $\Omega_0/2\pi = 313$ kHz for the data shown in figure 6.3. These motional quantum numbers are much lower than those observed in trap 1 (see section 6.2) and less than a factor of 4 above the Doppler limit of $\bar{n}_r = 4.3$ and $\bar{n}_z = 2.1$ calculated in section 2.5.

6.3.2 Coherent excitation of the upper radial sideband

Coherent excitation of the $^2S_{1/2}$ ($m_j = -1/2$) – $^2D_{5/2}$ ($m_j = -1/2$) upper radial sideband was performed. The intense probe laser was tuned to the sideband and the excitation probability recorded as the interrogation pulse length was varied from 0 μs to 40 μs. The resulting Rabi oscillations in the $^2D_{5/2}$ state population are shown in figure 6.4.

Following the model of equation 6.2 the observed Rabi oscillations on the

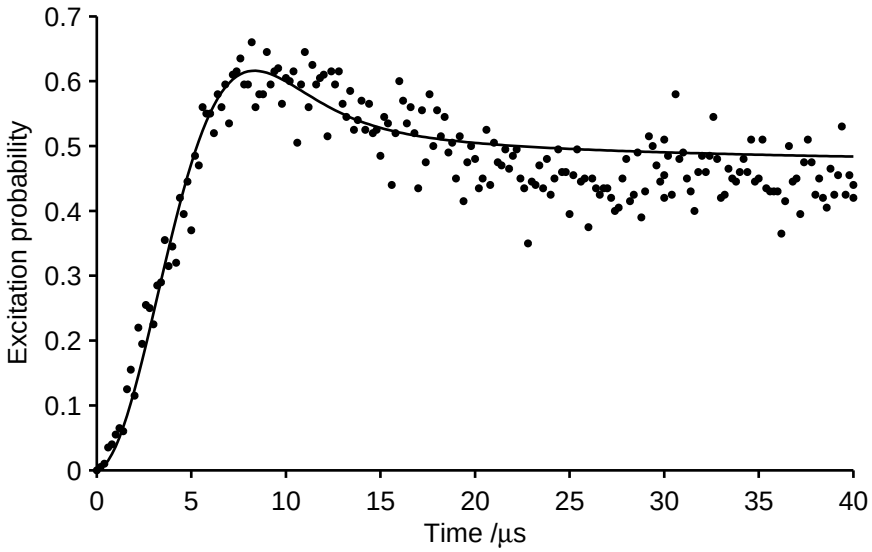

Figure 6.4: Rabi oscillations on the upper radial sideband of the $^2S_{1/2}$ ($m_j = -1/2$) – $^2D_{5/2}$ ($m_j = -1/2$) transition. Each data point is the result of 200 interrogations.

upper radial sideband are described by

$$P_D(t) = \frac{A}{2}\left(1 - e^{-\gamma t}\sum_{n_r,n_z} P_{n_r}(\bar{n}_r)P_{n_z}(\bar{n}_z)\cos\left(\Omega_{(n_r,n_z),(n_r+1,n_z)}t\right)\right) \qquad (6.4)$$

where

$$\Omega_{(n_r,n_z),(n_r+1,n_z)} = \Omega_0\sqrt{n_r+1}\eta_r e^{-\eta_r^2/2}L^1_{n_r}(\eta_r^2)e^{-\eta_z^2/2}L_{n_z}(\eta_z^2) \qquad (6.5)$$

as given by equation 2.23. After setting $\Omega_0/2\pi = 313$ kHz (as determined from coherent excitation on the carrier, equation 6.4 was fitted to the data of figure 6.4 using the procedure outlined in section 6.2. This yields mean radial and axial motional quantum numbers of $\bar{n}_r = 16$ and $\bar{n}_z = 9$. The poor fit of equation 6.4 to the data at times above 15 μs is likely to be due

to a small detuning of the probe laser from the radial sideband which is not accounted for in this analysis.

Coherent oscillations of higher contrast may be achieved by preparing the ion in a pure motional state by cooling the to the motional ground state of the trap [33]. With high contrast oscillations, it will be possible to prepare the ion in specific motional states with high fidelity by driving the sideband transitions. This is a requirement for the implementation of Cirac and Zoller's proposal for an ion trap quantum computer [16].

6.3.3 Coherent excitation of the upper axial sideband

Rabi oscilations were also observed on the upper axial sidebands of the $^2S_{1/2}$ $(m_j = -1/2)$ – $^2D_{5/2}$ $(m_j = -1/2)$ transition. Figure 6.5 shows the result of varying the interrogation pulse duration from 0 μs to 50 μs. Once again, an intense probe beam power of 1.5 mW is used. This data however, is not well described by the model used to describe the coherent oscillations observed on the carrier and upper radial sideband. Since coherent oscillations on the sideband are particular sensitive to the thermal distribution over the motional states of the trap, it should be expected that the oscillations dephase much more quickly than observed. The coupling strength

$$\Omega_{(n_r,n_z),(n_r,n_z+1)} = \Omega_0 e^{-\eta_r^2/2} L_{n_r}(\eta_r^2) \times \sqrt{n_z+1}\eta_z e^{-\eta_z^2/2} L^1_{n_z}(\eta_z^2) \qquad (6.6)$$

should also be small for a well cooled ion with $n_z \sim 10$. However, the data exhibits oscillations of both high contrast and high frequency.

It is hypothesised that the assumption that the ion's axial motional state

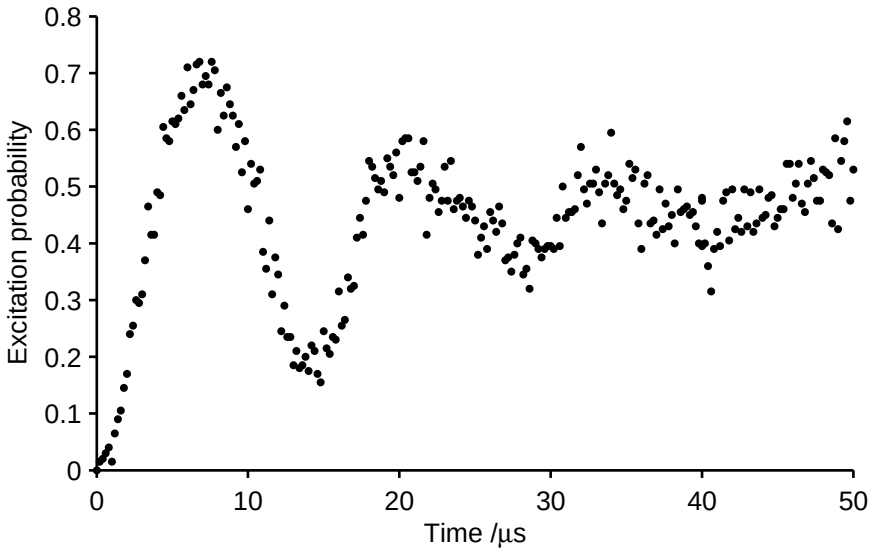

Figure 6.5: Rabi oscillations on the upper axial sideband of the $^2S_{1/2}$ $|m_j = -\frac{1}{2}\rangle$ – $^2D_{5/2}$ $|m_j = \frac{5}{2}\rangle$ transition. Each data point is the result of 200 interrogations.

is described by a thermal distribution over the motional states of the trap does not hold in the data of figure 6.5. A non-thermal narrow distribution with high mean axial motional quantum number may account for the data observed. This however requires further investigation. This situation of an unknown distribution of the ion over the motional states of the trap may be avoided by cooling the ion to the ground state of the trap, for example by the technique of sideband cooling (see chapter 9).

6.4 Summary

This chapter has demonstrated coherent 'Rabi' oscillations between the $^2S_{1/2}$ ($m_j = -1/2$) and $^2D_{5/2}$ ($m_j = -1/2$) state. Due to the distribution of the

ion over the motional states of the trap, the observed oscillations exhibit a decaying contrast. The rate of decay of this contrast is an invaluable tool for assessing the efficiency of Doppler cooling.

Coherent oscillations were observed by driving the $^2S_{1/2}$ ($m_j = -1/2$) – $^2D_{5/2}$ ($m_j = -1/2$) carrier transition in an ion stored in trap 1. The poor contrast of these oscillations implied that the ion was not well Doppler cooled, probably due to the existence of an anomalous heating rate in this trap.

Coherent oscillations of high contrast were observed on the $^2S_{1/2}$ ($m_j = -1/2$) – $^2D_{5/2}$ ($m_j = -1/2$) carrier transition using an ion in trap 2. The rate at which the contrast decays implies an ion with mean radial and axial motional quantum numbers of $\bar{n}_r = 14$ and $\bar{n}_z = 8$, which is a few times above the Doppler limit. Coherent oscillations have also been observed on the radial and axial sidebands of the $^2S_{1/2}$ ($m_j = -1/2$) – $^2D_{5/2}$ ($m_j = -1/2$) transition. The contrast of these oscillations decay much more rapidly than those on the carrier. This is due to the laser-ion coupling strength on a sideband having a stronger dependance on the ion's motional state than the coupling strength on the carrier.

Chapter 7

Ramsey spectroscopy

7.1 Introduction

The previous chapter has shown that it is possible to coherently drive the $^2S_{1/2} - {}^2D_{5/2}$ transition and prepare the Doppler cooled ion in a superposition of the $|S\rangle$ and $|D\rangle$ states with high fidelity. This suggests that Ramsey's method of separated oscillatory fields may be used to perform spectroscopy of the $^2S_{1/2} - {}^2D_{5/2}$ quadrupole transition.

Ramsey's method of separated oscillatory fields (Ramsey spectroscopy) was originally developed in 1950 [105] to improve the accuracy of molecular beam resonance experiments, and has since found widespread use in precision atomic and molecular spectroscopy [106]. In this technique, the atomic sample is interrogated by two coherent pulses of radiation, separated by a period of free precession. Ramsey's method of separated oscillatory fields has a number of advantages over conventional single pulse interrogation techniques, providing a reduction in the observed linewidth and an insensitivity

to inhomogeneity in the field experienced during the free precession period. These advantages have led to the use of this method in interrogating the hyperfine clock transition in cesium beam clocks [107] and, as laser-cooling methods have been developed, in atomic fountain clocks using cesium [108] and rubidium [109].

Early demonstrations of Ramsey spectroscopy in the optical domain were performed using a neon atomic beam [110] and a sodium vapour cell [111]. The prospect of high-precision optical experiments using Ramsey's method was illustrated by the observation of the Sagnac effect in a calcium beam interferometer [112]. The intercombination transition in laser-cooled ^{40}Ca atoms, interrogated using Ramsey's method, now represents the forefront of research into optical frequency standards based on high-Q optical transitions in neutral atoms [113, 114, 115, 116, 117]. Optical Ramsey spectra have been reported for similarly narrow transitions in single trapped ions of $^{199}Hg^{+}$ [5] and $^{88}Sr^{+}$ [118], which are also candidates for a future optical frequency standard. The work of Rafac *et al.* [5] presents results confirming that a Ramsey experiment results in a narrower linewidth when compared to a single pulse experiment of the same interrogation cycle duration. In addition, high contrast, high signal-to-noise Ramsey spectra have been used to study decoherence of quantum superpositions of the narrow 4s $^2S_{1/2}$ – 3d $^2D_{5/2}$ quadrupole transition in trapped $^{40}Ca^{+}$ ions [42, 87]. Ramsey spectroscopy has also been used to characterize ac-Stark shifts induced by an intense off-resonant laser on the same transition [119].

The characteristic fringe pattern observed in Ramsey spectroscopy is a result of quantum interference between the atomic excitation amplitudes of

the two temporally separate interactions. Any unintended phase shifts between the two oscillatory fields, as experienced by the atomic sample will lead to a shift in the resonance frequency observed [106]. A laser source of minimal phase fluctuations (i.e. high coherence) is therefore required. In addition, due to the short wavelength of the optical interrogation field, large unintended phase shifts will also occur due to atomic motion during the free precession period. This problem may circumvented by using two-photon Ramsey spectroscopy. In this technique, the atomic sample is interrogated using a standing wave laser field [120] in which the atom absorbs a photon from each direction to complete a two-photon transition. The total optical phase of the field is therefore independent of position. This method has been used to perform spectroscopy of the 1S – 2S transition in a beam of atomic hydrogen [121]. An alternative approach using single photon absorption, is the geometry of Bordé [122], which uses four travelling waves. This technique is used in spectroscopy of the narrow intercombination line in existing neutral ^{40}Ca experiments [113, 114, 115, 116, 117]. The systematic uncertainties of these systems should be reduced as sub-Doppler cooling schemes [123, 124, 125] and confinement in optical dipole traps [126] are employed. In contrast, an ion trapped in the Lamb-Dicke regime is confined to dimensions small compared to the wavelength of the interrogating radiation (see section 2.4.2). Therefore, the techniques of two-photon Ramsey spectroscopy and the Bordé four beam geometry are unnecessary and single-photon optical Ramsey spectroscopy using two temporally-separated oscillatory fields is possible [5, 118, 42, 87].

As discussed previously any unintended relative phase shift between the

separated fields experienced by the atomic sample will lead to a shift in the observed fringe pattern. Ramsey and Silsbee have pointed out that the fringe pattern may be shifted in a predictable manner through the use of a controlled phase difference $\delta\phi$ between successive interrogating pulses, and that this can provide significant advantages over 'conventional' Ramsey spectroscopy in which there is no phase difference [127]. Substantial benefits may be gained by simply measuring the difference in transition probability on switching $\delta\phi$ from $+90^\circ$ to -90° when using Ramsey's method of separated oscillatory fields. This interrogation scheme (hereafter referred to as 'phase modulation technique RS1') results in an anti-symmetric resonance signal, with a zero-crossing at line centre A further advantage is that the observed line centre frequency is insensitive to drifts in signal amplitude. A second, similar technique in which the change in transition probability on switching $\delta\phi$ from 0° to 180° yields in a symmetric fringe pattern with a maximum at line centre. This scheme will be referred to a 'phase modulation technique RS2'. Both Ramsey phase-modulation techniques are relatively insensitive to drifts in background signal. They were particularly useful in beam experiments where the beam intensity was a limiting factor, with the resulting signal being equivalent to that when the beam intensity was doubled. These are well-known techniques for rf and microwave experiments with beams, however to the best of the author's knowledge, there have been no reported demonstrations in the optical domain.

This chapter describes a series of experiments using Ramsey's method of separated oscillatory fields to perform spectroscopy of the $|m_j = -1/2\rangle$ – $|m_j = -1/2\rangle$ component of the quadrupole transition of a Doppler-cooled ion

and is organised as follows. Firstly, section 7.2 gives a theoretical description of the method of separated oscillatory fields applied to a Doppler-cooled trapped ion, including the effect of a finite laser coherence time and a relative phase difference between interrogating pulses. The means of generating a relative phase shift in the probe beam is described in section 7.3. Section 7.4 presents optical Ramsey spectra of the $^2S_{1/2}$ ($m_j = -1/2$) – $^2D_{5/2}$ ($m_j = -1/2$) transition. Conventional time-domain Ramsey spectroscopy (with no relative phase shift $\delta\phi$ between interrogating pulses) has been demonstrated and used to investigate the coherence of the experimental system. The effect of varying the relative phase difference $\delta\phi$ at line centre of the transition has been investigated and the results of phase modulation techniques RS1 and RS2 are presented. The observed fringe patterns are well described by numerical integration of the optical Bloch equations. The relevance of phase modulation technique RS1 and the controlled variation of the relative phase difference between Ramsey interrogation fields is discussed with regard to optical frequency standards and quantum information processing respectively in section 7.5.

7.2 Theoretical model

In Ramsey's method of separated oscillatory fields, an atomic transition is interrogated using two coherent fields of equal duration τ, separated by a period, T of free precession. The atom-field coupling strength is characterised by the Rabi frequency Ω_0. The pulse duration and Rabi frequency are chosen such that $\Omega_0\tau = \pi/2$ giving a '$\pi/2$-pulse'. The first of these $\pi/2$-pulses

prepares the ion in the $\frac{1}{\sqrt{2}}(|S\rangle + |D\rangle)$ coherent superposition of ground and excited electronic states. If the laser frequency ω_{laser} differs from the resonance frequency of the atomic transition ω_{atom}, a relative phase shift will be accumulated during the period of free precession. If this phase difference is an odd multiple of π, the second Ramsey $\pi/2$-pulse will return the atom to the ground state. At other phase differences, the ion is left in a superposition of ground and excited states and a non-zero excitation probability will be observed. When the laser is tuned to the centre of the resonance, there is zero accumulated phase difference and the maximum excitation probability occurs. The accumulated phase difference, which is linearly dependent on the detuning $(\omega_{\text{laser}} - \omega_{\text{atom}})$ of the laser from the atomic resonance thus determines the excitation probability and as a result, fringes approximately separated by $1/(T + \tau)$ are observed in the spectral line shape.

The coherent manipulation of the electronic state of a trapped ion has be described using the optical Bloch equations (equations 2.18 and 2.19) in section 2.4. This system of equations may also be used to model the evolution of the electronic state of the ion during Ramsey spectroscopy. During the first $\pi/2$ pulse, the atom-laser coupling strength is Ω_0 and the phase of the field is $\phi = 0$. From equations 2.18 and 2.19, the evolution of the system is therefore described by

$$\dot{\rho}_{DS} = \left[i(\omega_{\text{laser}} - \omega_{\text{atom}}) - \left(\Gamma_{\text{laser}} + \tfrac{1}{2}\Gamma_{DS}\right)\right]\tilde{\rho}_{DS} - i\tfrac{\Omega_0}{2}\left(\rho_{DD} - \rho_{SS}\right) \quad (7.1)$$

$$(\dot{\rho}_{DD} - \dot{\rho}_{SS}) = -\Gamma_{DS}\left[1 + (\rho_{DD} - \rho_{SS})\right] + i\Omega_0\left(\tilde{\rho}^*_{DS} - \tilde{\rho}_{DS}\right). \quad (7.2)$$

During the free precession period, the atom-laser coupling strength $\Omega_0 = 0$

and the optical Bloch equations become

$$\dot{\rho}_{DS} = \left[i(\omega_{\text{laser}} - \omega_{\text{atom}}) - \left(\Gamma_{\text{laser}} + \tfrac{1}{2}\Gamma_{DS}\right)\right]\tilde{\rho}_{DS} \tag{7.3}$$

$$(\dot{\rho}_{DD} - \dot{\rho}_{SS}) = -\Gamma_{DS}\left[1 + (\rho_{DD} - \rho_{SS})\right]. \tag{7.4}$$

Finally, during the second $\pi/2$-pulse, the atom-laser coupling strength is once again set to ω_0 and the evolution of the system is described by

$$\dot{\rho}_{DS} = \left[i(\omega_{\text{laser}} - \omega_{\text{atom}}) - \left(\Gamma_{\text{laser}} + \tfrac{1}{2}\Gamma_{DS}\right)\right]\tilde{\rho}_{DS} - i\tfrac{\Omega_0}{2}e^{-i\delta\phi}\left(\rho_{DD} - \rho_{SS}\right) \tag{7.5}$$

$$(\dot{\rho}_{DD} - \dot{\rho}_{SS}) = -\Gamma_{DS}\left[1 + (\rho_{DD} - \rho_{SS})\right] + i\Omega_0\left(e^{-i\delta\phi}\tilde{\rho}^*_{DS} - e^{i\delta\phi}\tilde{\rho}_{DS}\right) \tag{7.6}$$

where $\delta\phi$ is the phase difference between the Ramsey pulses.

The time evolution of the system is then found by numerically solving equations 7.1 – 7.6, for the relevant experimental parameters (τ, T, Ω_0) with the ion starting in the ground state (i.e. the initial condition $\rho_{SS} = 1$, $\rho_{DD} = 0$ at $t = 0$). The expected Ramsey fringe pattern for this two-level system is then given by finding this excitation probability as a function of the laser frequency ω_{laser}.

The results of solving 7.1 – 7.6 for a Ramsey pulse duration τ and pulse separation $T = 2\tau$, for the case of conventional Ramsey spectroscopy in which there is no relative phase difference between Ramsey pulses are shown in figure 7.1a. In this case $\delta\phi = 0°$ and equations 7.5 and 7.6 are reduced to 7.1 and 7.2. The fringe pattern for phase differences of 90°, 180° and −90° found in the same fashion are shown in figure 7.1b – d respectively. The

lineshapes expected from using phase modulation techniques RS1 and RS2 given by the change in transition probability on switching a relative phase difference $\delta\phi$ from $+90°$ to $-90°$ and switching from $0°$ and $180°$ respectively. The calculated lineshapes for theses two schemes are shown in figure 7.1e and f.

As discussed in section 2.4.2, a Doppler-cooled trapped ion will have a probability distribution over a number of vibrational levels $|n\rangle$ of the trap. An ion in each of these vibrational levels has a different atom-laser coupling strength, $\Omega_{n,n}$ given by equation 2.23. In one dimension, the coupling strength on the carrier transition is found from 2.23 to be

$$\Omega_{n,n} = \Omega_0 e^{-\eta^2/2} L_n(\eta^2) \tag{7.7}$$

where Ω_0 is the total coupling strength and $L_n(\eta^2)$ is the nth order Laguerre polynomial. It can now be seen that a $\pi/2$-pulse cannot be realised for an ion in all vibrational states simultaneously, since $\Omega_{n,n}\tau > \pi/2$ for some vibrational states and $\Omega_{n,n}\tau < \pi/2$ for others. The resulting fringes will therefore exhibit a lower contrast than the ideal case of a two-level atom at rest.

The expected fringe patterns for a Doppler-cooled ion may be calculated be taking into account the ion's thermal probability distribution over vibrational states $|n\rangle$ given by equation 2.28. The fringe pattern is therefore found by numerically solving equations 7.1 – 7.6 for each vibrational level, and summing these solutions in proportion to the occupation probability of the vibrational state. This may be viewed as a similar procedure to sum-

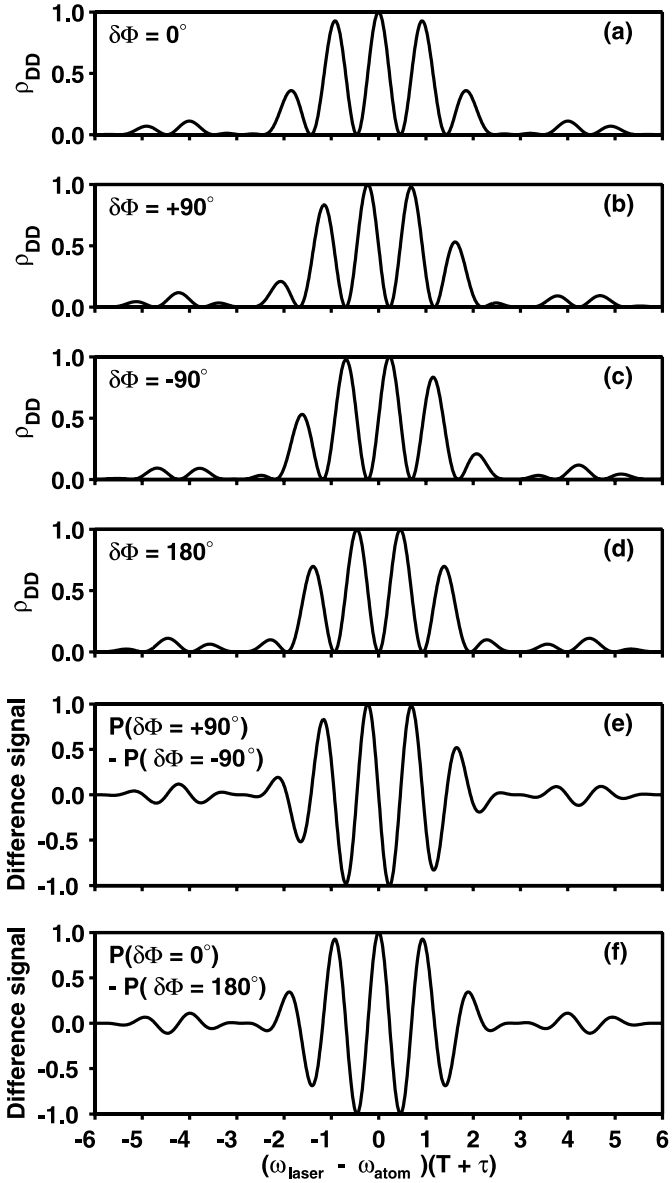

Figure 7.1: Calculated Ramsey fringe patterns for different relative phase shifts $\delta\phi$ between Ramsey pulses. Spectra shown are for $\delta\phi$ of (a) 0° (conventional Ramsey spectrum) (b) +90°, (c) −90°, and (d) 180°. The difference between the +90° and −90° signals yield an anti-symmetric signal shown in (e). The predicted change in transition probability on switching between 0° and 180° is shown in (f).

ming over the contributions of different velocity classes to the fringe patterns observe in atomic and molecular beam experiments [105]. The complication of summing contributions over the ion's thermal distribution of vibrational states may be avoided by preparing the ion in the motional ground state of the trap. This would mean that only a single Rabi frequency would be relevant in the calculation. In addition, this would also result in fringes of higher contrast [87].

7.3 Varying the probe laser phase

In order to demonstrate phase modulation techniques RS1 and RS2, it is necessary to introduce a relative phase difference between the two Ramsey pulses. The phase of the probe beam may be shifted using an electro-optic modulator, however this would require careful and precise calibration of the phase shift as a function of the voltage applied to the modulator. An alternative approach is to use an acousto-optic modulator (AOM) to introduce a phase shift into the probe beam.

If a phase shift $\delta\phi_R$ is applied to the RF drive of the AOM, a change in the optical phase $\delta\phi_O$ of the first-order diffracted beam occurs. It has been shown that $\delta\phi_R = \delta\phi_O$ [128], that is to say that the optical phase shift is equal to the phase shift introduced to the RF drive. The intense probe beam optical setup includes a single-pass, fixed frequency AOM, required for fast switching of the intense probe beam (see section 3.8). Arbitrary phase shifts may thus easily be imposed on the intense probe beam by using a direct digital synthesis (DDS) RF source and amplifier to drive this AOM.

The phase modulation technique RS1 requires only two different relative phase shifts: $\delta\phi = +90°$ and $-90°$, while phase modulation technique RS2 requires only $0°$ and $180°$. These phase differences maybe easily produced using an in-phase and quadrature (I&Q) modulator, which produces the four phase quadratures of an RF input. For the work described in this chapter, both an I&Q modulator and DDS sources have been used. The I&Q modulator was a Minicircuits MIQC-88M and at the frequency of 80 MHz used in this setup produced phase difference accurate to the $1°$. On the other hand, the Novatech Instruments 2908A, DDS signal generator also used during the course of this work, allowed arbitrary phase shifts to be set with a precision of $\sim 0.02°$ (1 part 16,384).

7.4 Spectroscopy of the $^2\mathrm{S}_{1/2}$ $(m_j = -1/2)$ – $^2\mathrm{D}_{5/2}$ $(m_j = -1/2)$ transition

Ramsey spectroscopy of the $^2\mathrm{S}_{1/2}$ $(m_j = -1/2)$ – $^2\mathrm{D}_{5/2}$ $(m_j = -1/2)$ transition is performed using an experimental sequence similar to that for single-pulse spectroscopy described in previous chapters. The only difference in this experimental routine is that the single interrogation pulse used previously is replaced by two Ramsey pulses of duration τ separated by a period of free precession T. The pulse sequence is shown in diagram 7.2.

For all the Ramsey spectra presented in this chapter, the intense probe beam was reduced to a power of ~ 75 μW, approximately 5% of the power typically used when performing single pulse coherent spectroscopy (see chap-

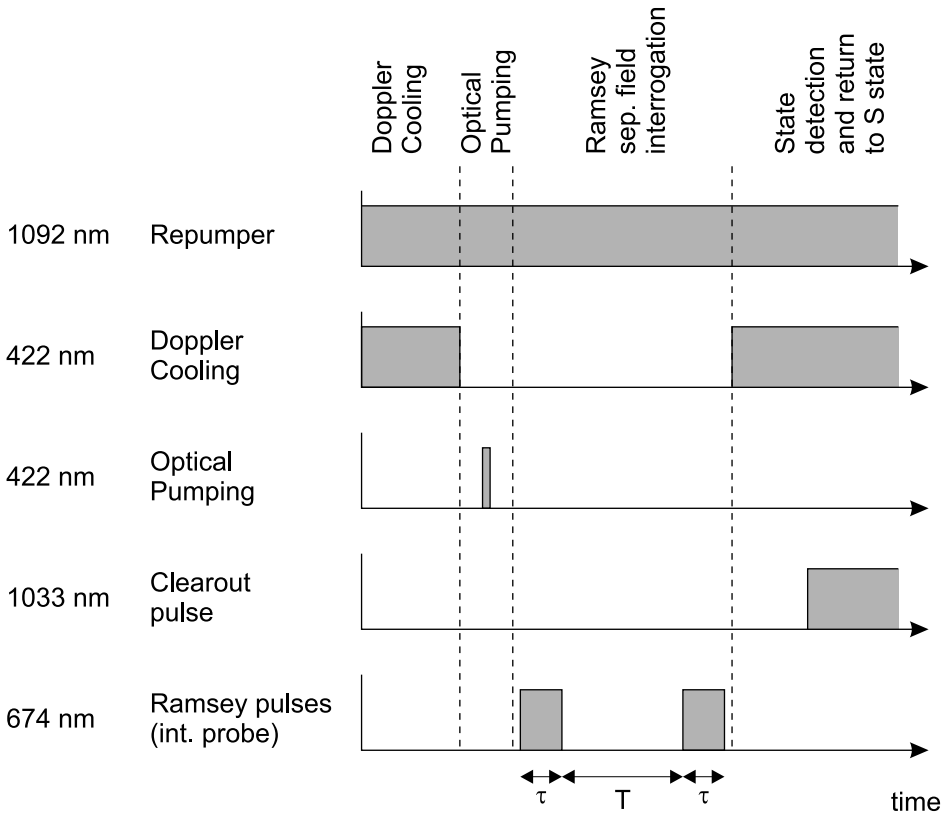

Figure 7.2: Pulse sequence using to perform Ramsey spectroscopy. (Not to scale)

ter 6).

To calculate the lineshapes that best describe the measured data, the optical Bloch equations (equations 7.1 – 7.6) were integrated numerically for each harmonic oscillator level, and summed with a statistical weight determined by the thermal occupation probability of each level. In all instances, the best fit to the data was determined using a maximum likelihood method pawi01, with $\tau_c = 1/\Gamma_{\text{laser}}$ as the only free parameter.

In order to determine the best fit to the data, the statistical noise present on the Ramsey signals must be considered. At each detuning of the probe laser, N independent measurements of the ion's electronic state are made. Each measurement results in one of two possible outcomes — the ion is either in the excited state or the ground state. The probability of each of these occurrences are $P_D = \rho_{DD}$ and $P_S = (1 - \rho_{DD})$ as predicted by the optical Bloch equations. Such a situation may be described by binomial statistics. So, for a specific set of experimental parameters, a series of N interrogations will result in a signal of NP_D observed excitations, with the standard deviation on the signal being $\sqrt{NP_D(1 - P_D)}$. In conventional optical Ramsey spectroscopy on a single trapped ion, the statistical noise of the central Ramsey fringe is largest half way up the fringe and approaches zero at the maximum and minimum.

The analysis of the noise in a Ramsey fringe signal has been considered in detail by Itano *et al.* [104] using a quantum treatment of the problem. It is important to note that in the case of a single ion, this quantum treatment yields the same result of binomial statistics in the number of excitations observed outlined above. These signal fluctuations have been named by

Itano et al. as the *quantum projection noise* [104]. In contrast to these noise statistics on a single ion, Ramsey experiments in atomic beams and fountains are limited by fluctuations in the atom number. By measuring the populations of the two states of the clock transition, the quantum projection noise limit can be reached [129], circumventing this limitation.

7.4.1 Conventional Ramsey Spectroscopy

Conventional Ramsey spectroscopy of the $^2S_{1/2}$ ($m_j = -1/2$) – $^2D_{5/2}$ ($m_j = -1/2$) transition is performed by setting zero phase difference between pulses (i.e. $\delta\phi = 0$). The ion is then repeatedly interrogated to determine the excitation probability. This procedure is repeated at each frequency in the interval of interest in order to build up the spectrum.

Using the probe laser beam at the reduced intensity of $\sim$75 μW, a single Rabi oscillation period was recorded, and the Rabi frequency $\Omega_0/2\pi$ was determined to be 15.7 kHz. Conventional Ramsey spectroscopy experiments were then conducted on the $|m_j = -1/2\rangle$ – $|m_j = -1/2\rangle$ Zeeman component of the quadrupole transition. A pulse duration of $\tau = 15.5$ μs was found to maximise the observed fringe contrast. The experimentally determined parameters Ω_0 and τ gave a good approximation to a $\pi/2$-pulse, since $\Omega_0\tau = 0.49\pi$. Conventional Ramsey spectroscopy was performed using pulse separations of $T = 20$, 40, 60, 80, 100, 150 and 200 μs. In all instances, the ion was interrogated 100 times at each detuning. However as T increased, the resolution of the scans was increased accordingly. This is detailed in Table 7.1, where the incremental steps in detuning for each scan are listed.

T /μs	Interrogations per step	Step size /kHz	$1/\Gamma_{\text{laser}}$ /μs	$\Gamma_{\text{laser}}/2\pi$ /kHz	Approx. scan rate / kHz/s
20	100	1.0	800	0.199	0.60
40	100	1.0	550	0.289	0.61
60	100	0.5	450	0.354	0.31
80	100	0.5	400	0.398	0.31
100	100	0.4	400	0.398	0.25
150	100	0.2	300	0.530	0.13
200	100	0.2	300	0.530	0.13

Table 7.1: Fitted values of Γ_{laser} for conventional Ramsey spectra shown in figure 7.3, along with step size and scan rate for each spectrum.

The resulting spectra are shown in figure 7.3 along with fitted theoretical fringe patterns for the experimental parameters τ, T and Ω_0. The theoretical fringe patterns were calculated by numerically integrating the optical Block equations (equations 7.1 – 7.6) as described in section 7.2 and the best fit chosen using a maximum likelihood method with the laser coherence decay rate $\tau_c = 1/\Gamma_{\text{laser}}$ being the sole free parameter. It is worth noting here that the model assumes only Gaussian laser phase fluctuations and that Γ_{laser} laser is the resulting laser linewidth.

From figure 7.3 it can be clearly seen that as the pulse separation is increased the Ramsey fringe contrast decreases. While there is good agreement between the experimental data and the theoretically predicted lineshapes, the apparent value of Γ_{laser}, as determined from the fitted theoretically predicted lineshapes, does not remain constant throughout the data. In fact, Γ_{laser} is observed to increase as the pulse duration T is increased, starting with $\Gamma_{\text{laser}}/2\pi = 0.19$ kHz when $T = 20$ μs and increasing up to $\Gamma_{\text{laser}}/2\pi =$

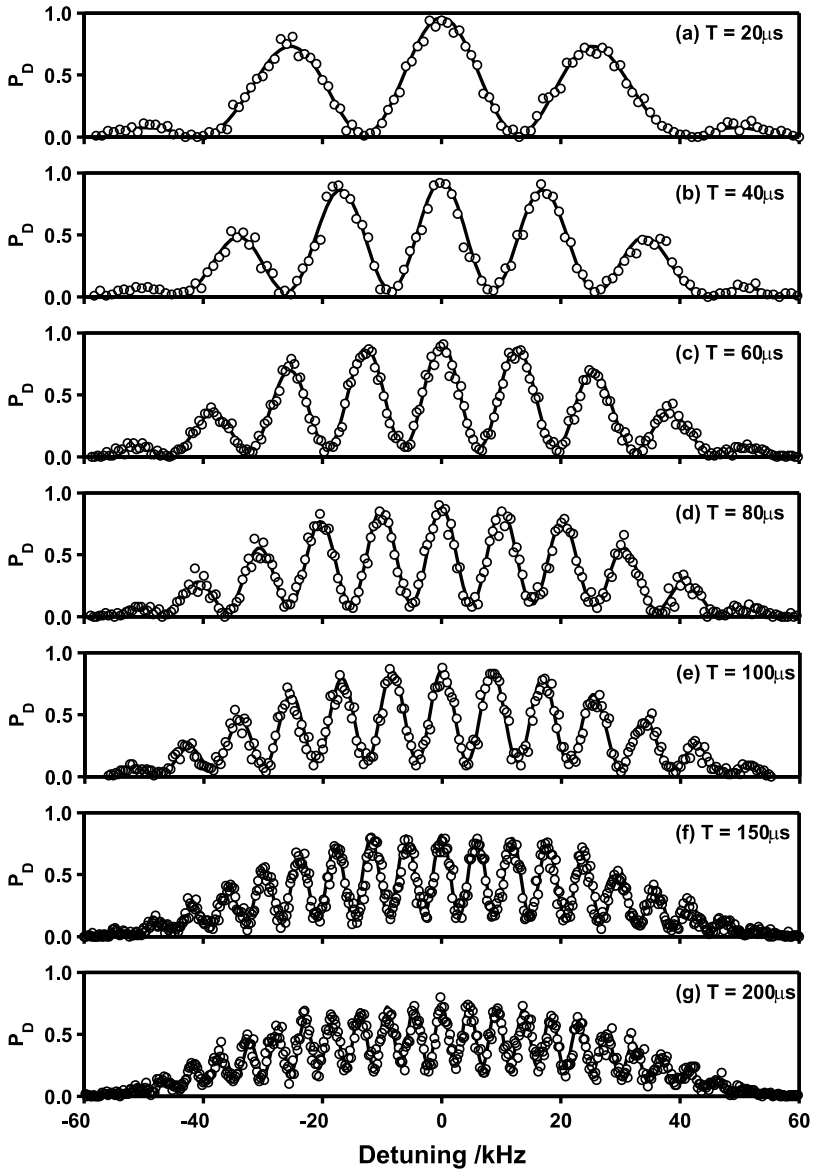

Figure 7.3: Conventional Ramsey spectroscopy of the $^2S_{1/2}$ ($m_j = -1/2$) – $^2D_{5/2}$ ($m_j = -1/2$) transition. The data shown used consecutive pulses of 15.5 μs duration, separated by periods T of (a) 20 μs, (b) 40 μs, (c) 60 μs, (d) 80 μs (e) 100 μs, (f) 150 μs and (g) 200 μs. Each data point is the result of 100 interrogations. The solid lines are fitted simulations with $\Omega_0 = 15.6$ kHz and laser coherence decay rate $\Gamma_{\text{laser}}/2\pi$ of (a) 0.19 kHz, (b) 0.29 kHz, (c) 0.35 kHz, (d) 0.40 kHz, (e) 0.40 kHz, (f) 0.53 kHz (g) 0.53 kHz.

0.53 kHz at $T = 200$ μs. These apparent values of Γ_{laser} are also inconsistent with the 2.4 kHz linewidth observed when using a weak single pulse excitation scheme to measure the laser linewidth (see figure 4.10) as discussed in section 4.6.3. Indeed, if $\Gamma_{\text{laser}} = 2\pi \times 2.4$ kHz (equivalent to a characteristic decay time $1/\Gamma_{\text{laser}} = 55$ μs), the Ramsey fringe contrast would be expected to decay much faster than in the data of figure 7.3.

The most likely explanation for these observations is slow drifts in the probe laser frequency not accounted for in the theoretical model used to predict the fringe patterns. The incremental step size in detuning for the various scans of figure 7.3 was chosen to record the Ramsey spectra with an appropriate resolution. Therefore, as the pulse seperatation T was increased, and the fringe seperation became smaller, a reduction in incremental steps in probe laser detuning was required. As a result, slower scan rates were employed at T was increased (see Table 7.1). With a slower scan rate, the Ramsey signal then becomes more sensitive to slow drifts in the probe laser frequency, resulting in an additional decrease in contrast. In the fitting procedure, $\tau_c = 1/\Gamma_{\text{laser}}$ is the only free parameter and this slow drift manifests itself as an apparent increase in the fitted laser linewidth.

The 2.4 kHz wide spectral line of section 4.6.3 would be particularly sensitive to the slow laser drift. It was recorded with a scan rate of around 0.04 kHz/s, which is considerably slower than for any of the Ramsey data of figure 7.3. Therefore the data of figure 4.10 has a far higher sensitivity to probe laser frequency drifts and noise components at the lowest Fourier frequencies.

Any significant heating of the ion during the Ramsey sequence would

also reduce the fringe contrast. However, this is unlikely to be the case since the timescale of the experiments performed here is less than 1 ms, whereas heating rates as low as 1 phonon in 190 ms have been reported for a trap of similar dimensions [33].

7.4.2 Effect of oscillator phase

The characteristic fringe pattern observed when using Ramsey's method of separated oscillatory fields is a result of the phase difference between the interrogation field and the atomic transition accumulated during the period of free precession. It is therefore to be expected that introducing a further phase shift to the second Ramsey interrogation pulses will similarly alter the fringe pattern in a predictable fashion.

The effect of varying the relative phase difference $\delta\phi$ between the Ramsey interrogation pulses was demonstrated as follows. The laser was tuned to line-centre of the atomic transition and the ion interrogated using two successive 15.5 μs $\pi/2$-pulses. With the pulse separation T fixed at 20 μs, the excitation probability was measured as the relative phase difference $\delta\phi$ between Ramsey pulses was varied. The results of this measurement are shown in Figure 7.4. Each data point is the result of 400 interrogations. Since the frequencies of the probe laser field and the atomic resonance are equal, no phase difference between the two is accumulated during the period of free precession. The sinusoidal variation in excitation probability is due solely to the relative phase difference between the two Ramsey interrogation pulses. The excitation probability is therefore maximised when $\delta\phi = 0^\circ$ and min-

imised when $\delta\phi = 180°$. The expected form of the excitation probability is shown by the solid curve of figure 7.4.

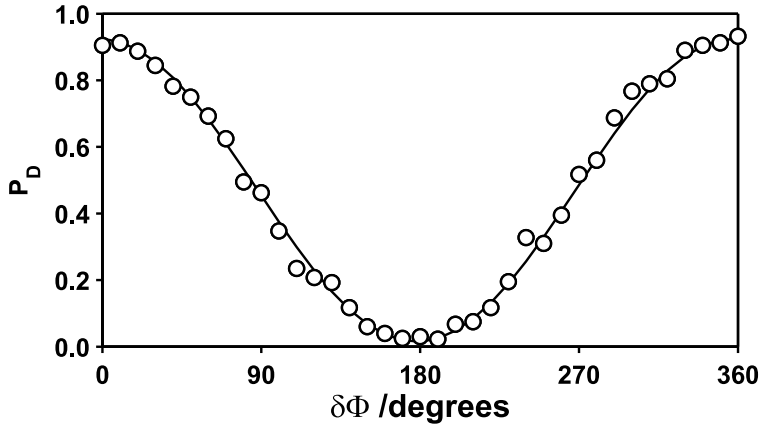

Figure 7.4: Excitation probability at line center on the $^2S_{1/2}$ ($m_j = -1/2$) – $^2D_{5/2}$ ($m_j = -1/2$) transition as the relative phase shift $\delta\phi$ between the Ramsey pulses is varied.

This data demonstrates precise control of the optical phase of the interrogation field relative to the ion. As an arbitrary phase shift may be introduced between the ion and the interrogation field, this technique may be used to null any known unwanted phase difference, or in the case of Ramsey spectroscopy any known frequency shifts.

7.4.3 Phase modulation techniques

The phase modulation techniques RS1 and RS2 measure the change in transition probability on switching $\delta\phi$, the relative phase shift between Ramsey pulses from $\delta\phi_x$ to $\delta\phi_y$ [127]. For phase modulation technique RS1, $\delta\phi_x = +90°$ and $\delta\phi_y = -90°$, while for RS2, $\delta\phi_x = 0°$ and $\delta\phi_y = 180°$. In order to measure the change in transition probability on switching the relative

phase shift, the ion is interrogated using each phase shift $\delta\phi_x$ and $\delta\phi_y$ at each probe laser detuning. Rather than interrogating the ion using the repeating sequence ($\delta\phi_x$, $\delta\phi_y$) a more complex sequence of ($\delta\phi_x$, $\delta\phi_y$, $\delta\phi_y$, $\delta\phi_x$, $\delta\phi_y$, $\delta\phi_x$, $\delta\phi_x$, $\delta\phi_y$) is used. This sequence is chosen to reject systematic errors in the measurement of the change in transition probability at each detuning due to time-dependent linear and quadratic drifts of any background signal that may exist [130]. The change in transition probability is simply found by calculating the mean difference between the excitation probabilities for each relative phase shift.

The phase modulation technique RS1 was demonstrated using a $\pi/2$-pulse duration of $\tau = 15$ μs and a free precession period $T = 40$ μs. The ion was interrogated using 25 sets of the relative phase shift interrogation sequence ($\delta\phi_x$, $\delta\phi_y$, $\delta\phi_y$, $\delta\phi_x$, $\delta\phi_y$, $\delta\phi_x$, $\delta\phi_x$, $\delta\phi_y$) - a total of 100 interrogations of each relative phase shift at each probe laser detuning. The resulting fringe patterns are shown in figure 7.5(a), while (b) and (c) show the excitation probability for the two constituent phase shifts $\delta\phi_x = +90°$ and $\delta\phi_y = -90°$. The fringe pattern predicted by solving the optical Bloch equations as outlined in section 7.2 are shown as solid lines in each figure.

Phase modulation technique RS2 has also been demonstrated using the same experimental parameters as those used to demonstrate phase modulation technique RS1 ($\tau = 15$ μs and $T = 40$ μs). Again, the ion was interrogated using 25 sets of the relative phase shift sequence ($\delta\phi_x$, $\delta\phi_y$, $\delta\phi_y$, $\delta\phi_x$, $\delta\phi_y$, $\delta\phi_x$, $\delta\phi_x$, $\delta\phi_y$) at each probe laser detuning. Figure 7.6(a) shows the resulting fringe pattern. It is important to note that this fringe pattern has a zero-crossing at line centre. The fringe patterns corresponding to each of the

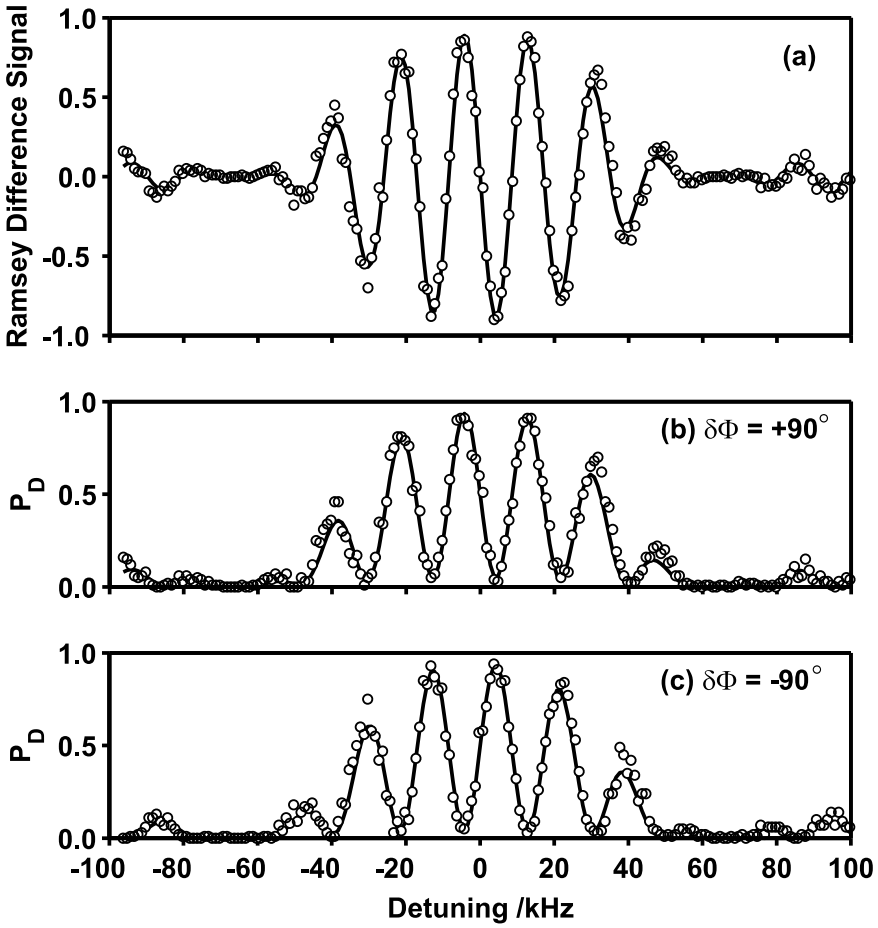

Figure 7.5: (a) Ramsey fringe pattern observed when measuring the change in excitation probability on switching the Ramsey pulse relative phase shift $\delta\phi$ between $+90°$ and $-90°$ (phase modulation technique RS2). Each point results from 100 interrogations of each phase. (b) Data for Ramsey measurement with $\delta\phi = +90°$ phase only, extracted from data of (a). (c) Data for Ramsey measurement with $\delta\phi = -90°$ phase only, extracted from data of (a). The solid curves are calculated using the optical Bloch equations and fitted to the data. The anti-symmetric lineshape in (a) crosses zero at line center.

two relative phase shifts $\delta\phi_x = 0°$ and $\delta\phi_y = 180°$ are shown in figures 7.5(b) and (c) respectively. The solid lines in each of these figures represents the theoretically predicted fringe patterns for the experimental parameters used.

7.5 Discussion

Ramsey's method of separated fields has been employed in both quantum information processing studies and also in optical frequency standards. The possible applications of controlled variation of the relative phase shift $\delta\phi$ and phase modulation technique RS1 (the measurement of the change in transition probability on switching from $\delta\phi = +90°$ to $-90°$) are now discussed in this context.

Ramsey spectroscopy was employed by Häffner *et al.* to investigate the phase shifts induced by an intense off-resonant laser beam incident on a single $^{40}Ca^{+}$ ion during the period of free precession. This work was motivated by the fact that such phase shifts commonly occur in quantum information processing schemes where superpositions of atomic states are manipulated by intense lasers. These unintentional phase shifts of the quantum states are due to the AC-Stark shifts of the atomic energy levels caused by the off-resonant interaction of the laser with other nearby transitions (such as motional sidebands, or other Zeeman or hyperfine transitions). Häffner *et al.* used a second off-resonant laser beam to induce an equal but opposite ac-Stark shift to that caused by the first laser beam. Rather than using a second laser field to null the phase shift induced by the intense off-resonant laser present during the free precession period, the phase shift may be compensated

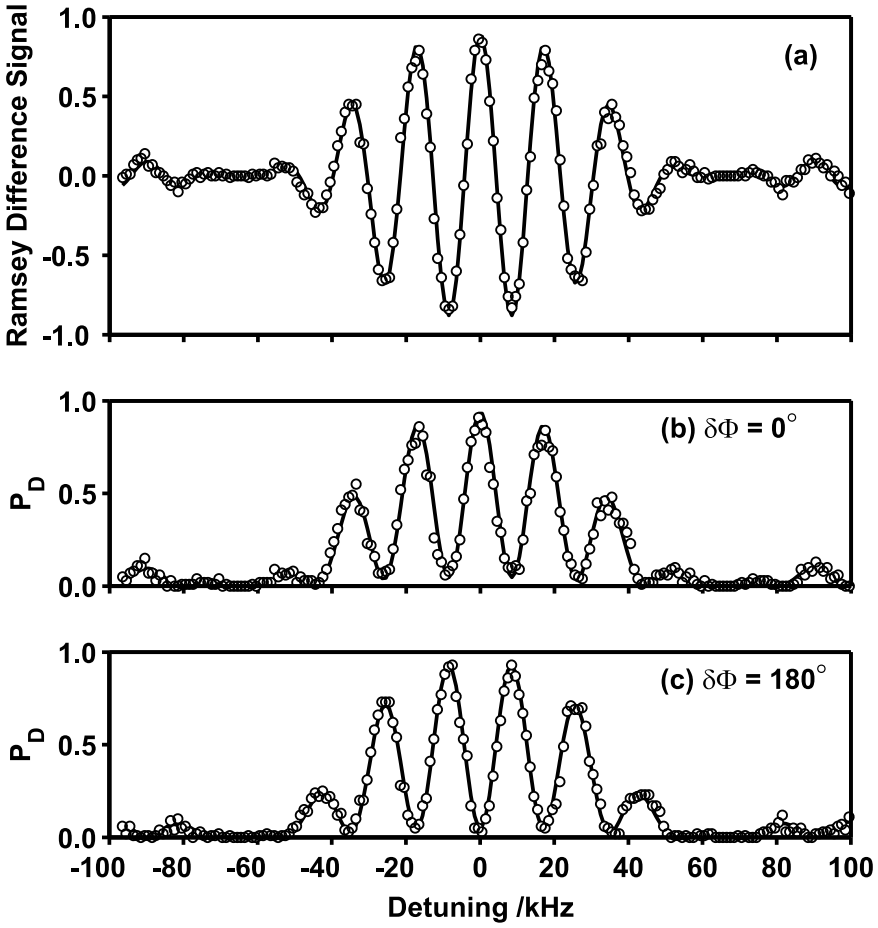

Figure 7.6: (a) Ramsey fringe pattern observed when measuring the change in excitation probability on switching the Ramsey pulse relative phase shift $\delta\phi$ between 0° and 180° (phase modulation technique RS1). Each point results from a total of 200 interrogations, 100 of each phase. (b) Data for Ramsey measurement with $\delta\phi = 0°$ phase only, extracted from data of (a). (c) Data for Ramsey measurement with $\delta\phi = 180°$ phase only, extracted from data of (a). The solid curves are calculated using the optical Bloch equations and fitted to the data.

simply by introducing the necessary phase shift to the laser field. As has been demonstrated in section 7.4.2 this may be achieved by simply altering the phase of the RF drive of an AOM in the beam path.

In an optical frequency standard, a local oscillator is stabilised to a high-Q atomic transition. To date, the various standards using a trapped ion as the atomic reference have used a frequency modulation scheme [116, 6, 7, 131], where the transition is interrogated both below and above resonance. The asymmetry in the excitation probability determines the required correction to the laser frequency to tune it to line centre.

Phase modulation technique RS1 offers a significant advantages over the measurement of the asymmetry in excitation probability above and below resonance. This phase modulation technique yields an anti-symmetric discriminant with a zero-crossing at line center. This technique is therefore highly relevant for laser stabilization to a narrow optical transition. This Ramsey signal is also advantagous in that the frequency of the line center is independent of drifts in signal amplitude. Such drifts, due to deviations from the $\pi/2$-pulse condition, will only affect the gradient of the signal at line center. It is useful to note that as long as the relative phase shifts remain identical in magnitude, but of opposite sign, the zero-crossing of figure 7.5 will remain at line center. Therefore a small offset $\delta\theta$ in the phase, such that $\delta\phi_x = -\delta\phi_y = (90^\circ + \delta\theta)$, also only result in a small change of the fringe pattern's gradient at line center.

This laser stabilization technique, is discussed further and demonstrated in chapter 8. This same phase-modulated Ramsey technique will also be of benefit to neutral atom optical frequency standards when the atomic sample

is appropriately confined, allowing a two-pulse Ramsey experiment [126].

7.6 Summary and conclusion

This chapter has presented the demonstration of optical Ramsey spectroscopy of a single Zeeman component of the $^2S_{1/2} - {}^2D_{5/2}$ quadrupole transition in a Doppler cooled $^{88}Sr^+$ ion. High contrast Ramsey fringes have been observed with visibilities of up to $\sim$90%. Increasing the period of free precession between Ramsey interrogation pulses results in a decrease in fringe contrast that is attributed to the finite coherence time of the probe laser.

Introducing a controlled phase difference between Ramsey interrogation pulses is observed to alter the Ramsey fringe pattern in a predictable manner. Varying the optical phase by an arbitrary amount is of use in compensating unwanted atomic phase shifts during a sequence of coherent pulses to manipulate an atomic state, as in quantum information processing studies.

In addition to conventional Ramsey spectroscopy, the phase modulation techniques proposed by Ramsey and Silsbee have been demonstrated. In the first, phase modulation technique RS1, the change in transition probability on reversing a 90° is measured. This produces an anti-symmetric Ramsey fringe pattern and would make an ideal discriminant for the stabilisation of a local oscillator to a narrow atomic reference transition in a trapped ion. In the second method, phase modulation technique RS2, the change in transition probability on switching the relative phase difference $\delta\phi$ from 0° to 180° is measured. This results in a symmetric fringe pattern with a a maximum at line centre.

A theoretical model for describing the interrogation of a Doppler cooled trapped ion has been presented. All observed fringe patterns are found to agree well with those predicted.

Chapter 8

Stabilisation of the probe laser to the quadrupole transition

8.1 Introduction

In an optical atomic frequency standard, a local oscillator is stabilised to a high Q-factor reference transition. A number of suitable reference transitions are being investigated in laser-cooled samples of neutral atoms such as ^{40}Ca [113, 114, 115, 116, 117] and cold trapped ions such as, $^{88}Sr^{+}$ [6, 7], $^{171}Yb^{+}$ [131, 10], $^{199}Hg^{+}$ [5], $^{115}In^{+}$ [9]. For such an optical atomic frequency standard, the local oscillator stabilised to the reference transition is a high stability laser source.

In work using laser cooled ^{40}Ca atoms, Ramsey's method of separated field has been used. However, reported absolute measurements of optical clock transitions in single ions of $^{199}Hg^{+}$ [5], $^{88}Sr^{+}$ [6, 7], $^{171}Yb^{+}$ [131, 10] and $^{115}In^{+}$ [132] have not so far taken advantage of the superior signal to

noise ratio afforded by Ramsey's technique. Instead, these measurements interrogated the clock transition using a single pulse excitation scheme. The majority of these experiments [116, 6, 7, 131] stabilized the laser to the line centre by comparing alternate measurements of a relatively low excitation rate on either side of the line.

This chapter describes the stabilisation of the probe laser to the $^2S_{1/2}$ $(m_j = -1/2)$ – $^2D_{5/2}$ $(m_j = -1/2)$ Zeeman component of the quadrupole transition. Ramsey's method of separated oscillatory fields using phase modulation technique RS1 (see chapter 7), in which the change in transition probability on reversing a 90° phase shift between interrogation fields is measured, provides the discriminant for feedback to the probe laser frequency.

8.2 Stabilisation of the probe laser to the $^2S_{1/2}$ $(m_j = -1/2)$ – $^2D_{5/2}$ $(m_j = -1/2)$ transition

As with the demonstrations of Ramsey's method of separated oscillatory fields of chapter 7, the probe laser intensity was reduced to ∼75 μW. The experimental sequence of figure 7.2 was again used and for the work described in this chapter, a free precession period, T of 40 μs was employed. A pulse duration of $\tau = 18$ μs was found to maximise the observed fringe contrast of Ramsey spectra of the $^2S_{1/2}$ $(m_j = -1/2)$ – $^2D_{5/2}$ $(m_j = -1/2)$ transition.

Spectra of the $^2S_{1/2}$ $(m_j = -1/2)$ – $^2D_{5/2}$ $(m_j = -1/2)$ transition where then obtained using phase modulation technique RS1 in which the change in transition probability on reversing a 90° phase shift between the Ramsey

interrogation pulses is measured. As in section 7.4.3 the ion was interrogated with the relative phase difference $\delta\phi$ of $\delta\phi_x = +90°$ and $\delta\phi_y = -90°$ in the sequence ($\delta\phi_x$, $\delta\phi_y$, $\delta\phi_y$, $\delta\phi_x$, $\delta\phi_y$, $\delta\phi_x$, $\delta\phi_x$, $\delta\phi_y$). The difference signal is given by the difference between the number of times the ion is excited to the $^2D_{5/2}$ state when $\delta\phi = +90°$ and when $\delta\phi = -90°$. This interrogation scheme results in an anti-symmetric fringe pattern of figure 8.1 which has a zero crossing at the resonance frequency. The fringe pattern was obtained using free precession period of 40 μs and an interrogation pulse duration of 18 μs. Each data point in this figure corresponds to the result of 25 sets of the sequence of 8 interrogations — a total of 100 interrogations of the ion with each relative phase difference.

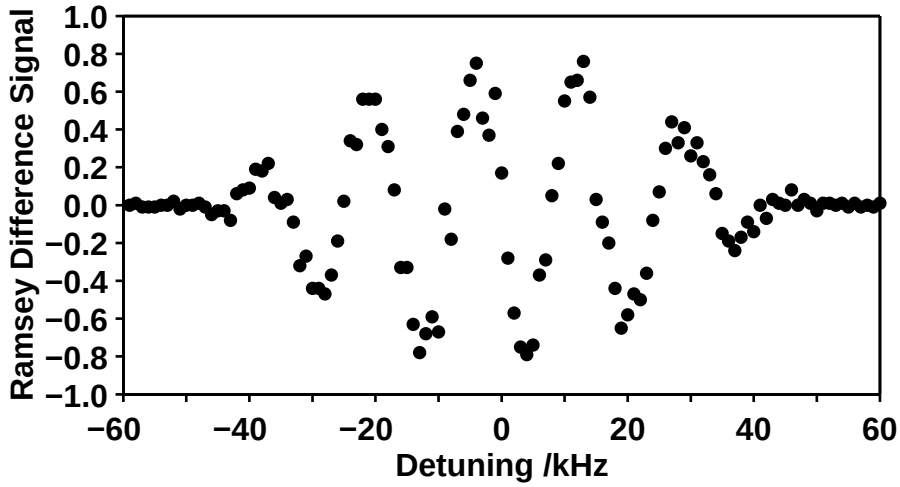

Figure 8.1: Ramsey spectra of the $^2S_{1/2}$ ($m_j = -1/2$) – $^2D_{5/2}$ ($m_j = -1/2$) transition recorded using phase modulation technique RS1. A pulse duration of $\tau = 18$ μs and pulse separation of $T = 40$ μs was used. Each data point is the difference in excitation probability measured over 100 interrogations with a $+90°$ phase shift and 100 interrogations with a $-90°$ phase shift.

With the zero-crossing corresponding to line-centre identified, the central

fringes around the resonance frequency were recorded again using 200 interrogations of each phase difference at each point (again with, $T = 40$ μs and $\tau = 18$ μs). The resulting Ramsey difference signal is shown in figure 8.2. For this pulse duration and separation, the difference signal remains positive up to 7.5 kHz below line-centre and negative up to 7.5 kHz above line-centre. The capture range of a feedback loop using this discriminant will therefore be ± 7.5 kHz. The slope of the discriminant at line centre is ~ 0.3 kHz^{-1}.

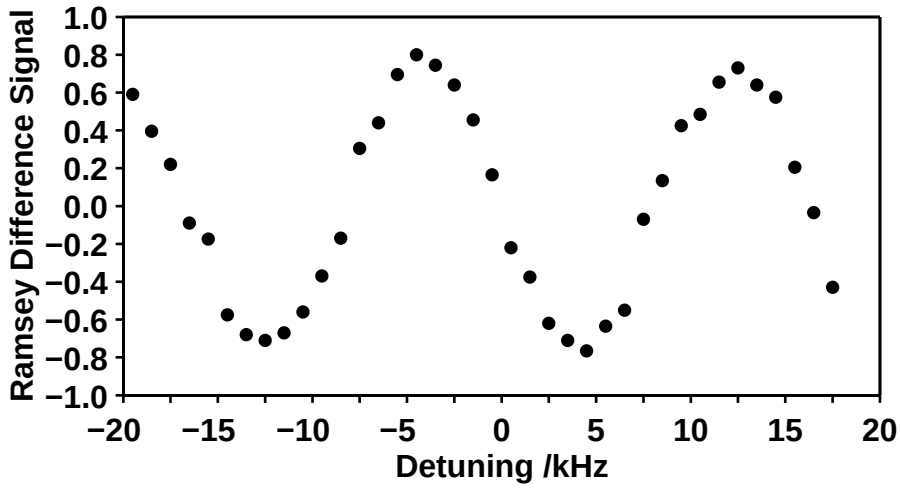

Figure 8.2: Spectra recorded using phase modulation technique RS1 showing the central fringes and zero-crossing at line centre of the $^2S_{1/2}$ ($m_j = -1/2$) – $^2D_{5/2}$ ($m_j = -1/2$) transition. A total of 400 interrogations (200 of each phase) where taken at each point.

The Ramsey difference signal was then used as the discriminant for stabilising the probe laser frequency to the $^2S_{1/2}$ ($m_j = -1/2$) – $^2D_{5/2}$ ($m_j = -1/2$) transition. The stabilisation servo loop is implemented in software and provides proportional feedback. This feedback is applied to the active tuning element of the slave laser, namely the offset lock RF synthesizer (see section 3.8). To start, the probe laser was intentionally detuned by ~ 7.5 kHz

below line centre and the feedback loop was engaged. The resulting time evolution of the correction to the offset lock frequency required to tune the laser to line centre is shown in figure 8.3a. The ion was probed at each point using 50 sets of eight phase-modulated interrogations to measure an error signal and determine the correction to be applied to probe laser frequency. The proportional gain of the servo was set to 3,000 Hz per unit error signal. The error signal during the period the lock was engaged is shown in figure 8.3b. As the lock is engaged, the laser actively tunes towards, and locks to, line centre. Since the feedback is proportional, the point at which the correction frequency step is largest corresponds to the point at which the error signal is largest.

The correction to the offset lock frequency required to keep the probe laser tuned to line centre continues exhibits a slow drift after the lock has engaged. This relative frequency drift between the probe laser and the $^2S_{1/2}$ ($m_j = -1/2$) – $^2D_{5/2}$ ($m_j = -1/2$) transition is likely to be due to offset drifts in the master laser lock to the ULE cavity which is of relatively low finesse.

8.3 Discussion

This section compares the Ramsey interrogation scheme with the 'traditional' single pulse interrogation schemes which have been previously used to generate frequency discriminants in work using trapped ions [116, 6, 7, 131]. In the case of the Ramsey scheme employing phase modulation technique RS1, the discriminant is found by detecting an imbalance in the number of

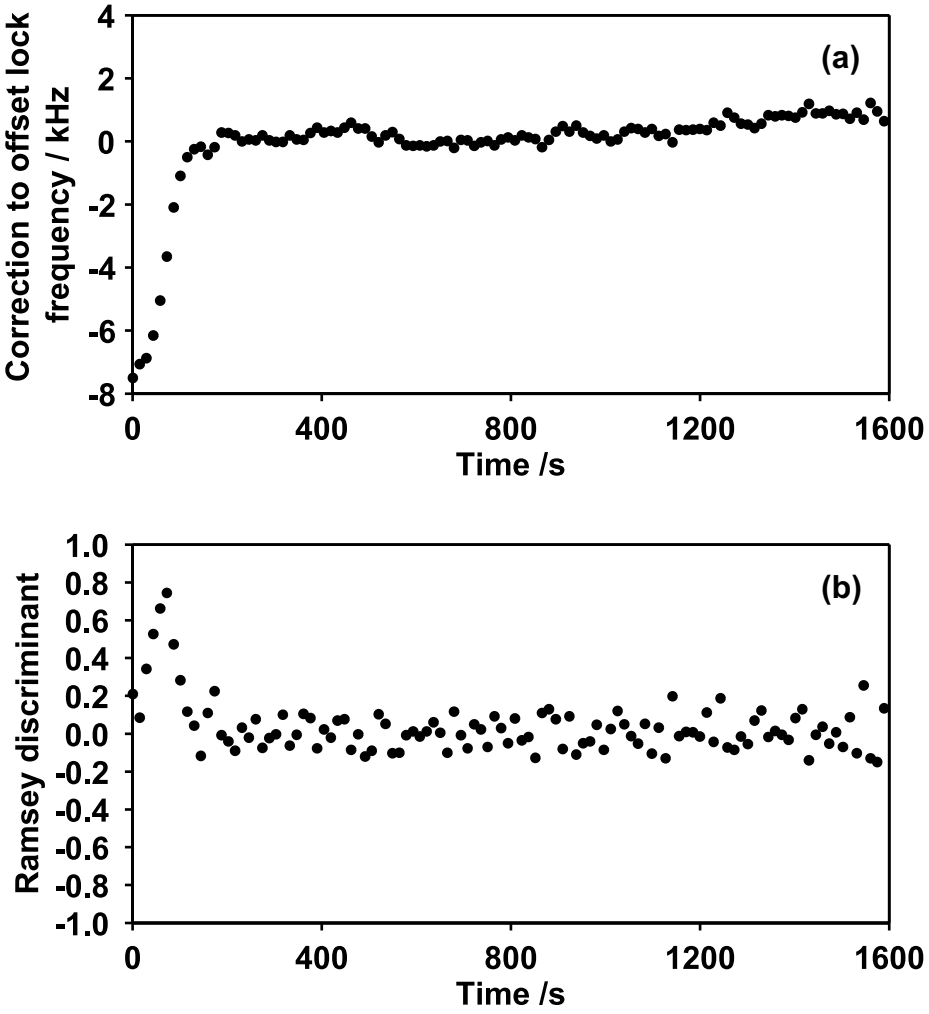

Figure 8.3: Laser stabilisation using phase modulation technique RS1 discriminant. The probe laser is detuned half a fringe below line centre when the laser lock is engaged. The laser lock is engaged at 0 s and has settled to line centre of the transition by ∼200 s. The correction to the offset lock frequency and the error signal given are shown in (a) and (b) respectively.

transitions observed when using phase differences of $+90^\circ$ and -90° between the Ramsey pulses. In contrast, in the single pulse interrogation scheme, the imbalance in the number of transitions observed at detunings of $\pm\Delta\omega$ gives the frequency discriminant.

A common measure of the performance of a stabilised laser is its Allan variance (two-sample variance). If the laser frequency is measured over consecutive intervals of time τ, and the fractional frequency difference between the nth measurement and the $(n+1)$th measurement is Δy_n, the Allan variance is given by

$$\sigma_y^2(\tau) = \frac{1}{2}\sum_{n}^{N-2}\frac{(\Delta y_n)^2}{N-2}. \tag{8.1}$$

where N is the total number frequency measurements made. In the case of random and uncorrelated frequency fluctuations of the laser, the Allan variance is then simply the relative frequency variance over the set of measurements. The Allan deviation (i.e. square root of the Allan variance) is given by averaged relative frequency fluctuations

$$\sigma_y(\tau) = \left\langle \frac{\Delta f_{\mathrm{rms}}}{f_0} \right\rangle \tag{8.2}$$

where Δf_{rms} is the root mean square frequency fluctuation and f_0 is the laser frequency.

The r.m.s. frequency fluctations of the stabilised laser is calculated according to the procedure outlined by Riis and Sinclair [133] as follows. For the sake of generality, the following notation is adopted. The excitation probability at each detuning $\pm\Delta\omega$ in the single pulse scheme and each phase difference of $\pm 90^\circ$ in the Ramsey scheme is denoted by $P_{\pm}(\omega)$. A single

'measurement' is composed of a pair interrogations, one at each frequency or phase corresponding to points $P_{\pm}(\omega)$.

The discriminant signal S, obtained by making N_T measurements in a total time T, is

$$S(\omega) = \frac{N_T}{T} P_+(\omega) - \frac{N_T}{T} P_-(\omega). \tag{8.3}$$

where S has units of s^{-1}. If each interrogation takes a time ΔT, and the dead time between interrogations is assumed to be negigible, N_T measurements takes a time $2N_T\Delta T$ and it follows that

$$S(\omega) = \frac{P_+(\omega) - P_-(\omega)}{2\Delta T}. \tag{8.4}$$

The gradient of the signal at line centre is thus given by

$$D = 2\pi \frac{\mathrm{d}S}{\mathrm{d}\omega}\bigg|_{\omega=\omega_0} \tag{8.5}$$

where the 2π is required to express the gradient in 'real' frequency rather than angular frequency units.

Each measurement consists of $2N_T$ interrogations of the ion, with excitation probability P. The statistical noise is due solely to the quantum projection noise [104] and is described by binomial statistics. The standard deviation in measuring the discriminant σ_S is therefore

$$\sigma_S = \frac{\sqrt{2N_T P(1-P)}}{T} = \frac{1}{\sqrt{T}} \sqrt{\frac{P(1-P)}{\Delta T}}. \tag{8.6}$$

The r.m.s. frequency fluctuations of the laser may now be found be projecting

this measurement noise in the discriminant onto the frequency axis using the slope of the discriminant

$$\Delta f_{\mathrm{rms}} = \frac{\sigma_S}{D} = \frac{1}{\sqrt{T}} \left(\sqrt{\frac{P(1-P)}{\Delta T}} \Big/ 2\pi \frac{\mathrm{d}S}{\mathrm{d}\omega}\Big|_{\omega=\omega_0} \right) \tag{8.7}$$

giving the Allan deviation

$$\sigma_y(T) = \frac{1}{f_0\sqrt{T}} \left(\sqrt{\frac{P(1-P)}{\Delta T}} \Big/ 2\pi \frac{\mathrm{d}S}{\mathrm{d}\omega}\Big|_{\omega=\omega_0} \right) \tag{8.8}$$

of the stabilised laser.

To do:

AC-Stark shift must be considered.

Ultimately achievable stability for reasonable experimental parameters - application to $\delta m = 0$ transition in, for example, $^{87}\mathrm{Sr}^+$.

8.4 Summary and conclusion

A dispersion-like fringe pattern has been obtained using Ramsey's method of separated oscillatory fields with phase modulation RS1. This signal contains a zero-crossing at line centre and is therefore an ideal laser stabilisation discriminant. Using a proportional feedback servo, the probe laser has been stabilised to the narrow $^2\mathrm{S}_{1/2}$ ($m_j = -1/2$) – $^2\mathrm{D}_{5/2}$ ($m_j = -1/2$) transition. This method is of use in optical frequency standards, where a local oscillator must be stabilised to a narrow optical resonance. ??Quote realistic state-of-the-art $^{87}\mathrm{Sr}^+$ stability using this method??

Chapter 9

Resolved Sideband Cooling

9.1 Introduction

An ion cooled to the zero-point energy of its trapping potential, while itself of fundamental interest as a non-classical motional state, is a prerequisite for wide range of experiments. With an atom cooled to the ground-state of the trap, the Jaynes-Cummings interaction [134] may be realised in the strong coupling regime. This interaction may also be exploited to generate other nonclassical states of motion, such as squeezed states [135, 136, 137]. If the collective motion of a number of ions is cooled to the ground state of the trapping potential, it is possible to create 'EPR'-like [138, 139] states in which the ions have correlated internal states [46]. Such a 'spin-squeezed' system should allow a reduction of the quantum projection noise in spectroscopic measurements [140, 141].

In Cirac and Zoller's proposal for an ion trap quantum computer [16], information is encoded in the internal energy states of the ion, while quan-

tum gates are realised by coupling the ions through their collective motional state. As a result, this scheme requires the ground state cooling of the centre-of-mass motion. Single ions cooled to the ground state of their trapping potentials have been used to demonstrate a logic gate [38] and the Deutsch-Josza algorithm [40] and more recently two-ion systems have been used to demonstrate the Cirac-Zoller C-NOT gate [45] and a two-qubit phase gates [142].

Ground state cooling may be achieved by the technique of resolved sideband cooling [67, 143, 144]. If the linewidth of an optical transition in the ion is smaller than the vibrational frequency of the trap ($\Gamma \ll \omega_{\mathrm{sec}}$), the ion is in the so-called strong binding regime and the transition is split into a well resolved carrier and sidebands spaced at the secular frequency. By driving the lower (red) sideband of the transition, the ion's motional energy is reduced by one vibrational quantum (see figure 2.4). For an ion in the Lamb-Dicke regime, the subsequent spontaneous emission occurs predominantly on the carrier without a change in motional quantum number. Each absorption-emission cycle therefore reduces the kinetic energy of the ion by one vibrational quantum. As this process is repeated, the ion is transferred down the ladder of motional states, as shown in figure 9.1. Since the laser-ion coupling strength on the red sideband is proportional to $\sqrt{n}$ to first order (see section 2.4.2) the red sideband vanishes as the ion is cooled to the motional ground state of the trap and the ion becomes decoupled from the laser.

The strong binding regime is difficult to achieve experimentally as typical secular frequencies are of the order of 1 MHz — smaller than the typical linewidths of allowed electric-dipole optical transitions. While traps with

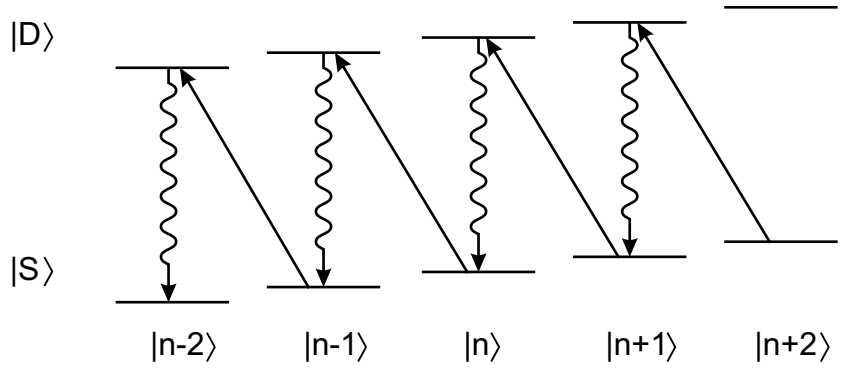

Figure 9.1: Absorption and emission processes in resolved sideband cooling on the quadrupole transition. Absorption on the red sideband and emission on the carrier leads to a reduction in the ion's motional quantum number by one phonon.

much higher secular frequencies [54] have been developed in the hope of allowing resolved sideband cooling on electric-dipole transitions, sideband cooling on such strong transitions has not been reported in the literature. Resolved sideband cooling to the motional ground state has instead been achieved using weakly allowed optical transitions, such as quadrupole transitions in $^{198}Hg^{+}$ [32] and $^{40}Ca^{+}$. [33], the narrow intercombination line in $^{115}In^{+}$ [34] and two-photon Raman transition in $^{9}Be^{+}$ [35]. In the case of $^{88}Sr^{+}$, the $^{2}S_{1/2} - {}^{2}D_{5/2}$ quadrupole transition at 674 nm with a linewidth of 0.4 Hz satisfies the condition $\Gamma \ll \omega_{\mathrm{sec}}$ of the strong binding regime.

Resolved sideband cooling on the bare quadrupole transition will be hampered by the long natural lifetime of the excited state. The 390.3 ms lifetime of the $^{2}D_{5/2}$ state in $^{88}Sr^{+}$ (see chapter 5) would limit the rate of spontaneous emission to one photon in 390.3 ms, giving a maximum cooling rate of 2.6 vibrational quanta per second. In fact, since reported external heating rates in RF traps are of the order of 5 quanta/s [33, 32], cooling on the

bare quadrupole transition may not be possible at all. In order to realise an acceptable cooling rate, the effective lifetime of $^2D_{5/2}$ state is be shortened by coupling it to the short-lived $^2P_{3/2}$ state using a 'quencher' laser. The ion is cooled using a similar scheme to that used in $^{40}Ca^+$ [33] which has an analogous electronic structure to $^{88}Sr^+$. After resolved sideband cooling, the ion's motional state is determined from the asymmetry in first upper and lower motional sidebands.

This chapter is organised as follows. Section 9.2 outlines a simple theoretical model of sideband cooling, the cooling scheme used in $^{88}Sr^+$ and a method for determining the motional state after cooling. Section 9.3 describes the first demonstration of resolved sideband cooling of a $^{88}Sr^+$ ion. Spectra identifying the various motional sidebands are presented, the AC-Stark shift in the quadrupole transition due to the presence of the 'quencher' radiation is characterised, and the vibrational quantum number after sideband cooling of the axial motional mode is measured. This result is discussed in section 9.4.

9.2 Theory

9.2.1 Simple model of sideband cooling

The dependencies of the cooling rate on the sideband cooling laser and quencher laser intensities and detunings have been investigated theoretically [145]. These numerical models are beyond the scope of this thesis. Instead, the simple model of Leibfried *et al.* [31] which outlines the salient

features of the system is used.

The $^{88}Sr^{+}$ ion is treated as a three level 'cascade' system (see figure 9.2). The $^2S_{1/2}$ – $^2P_{3/2}$ and $^2P_{3/2}$ – $^2D_{5/2}$ transitions have linewidths Γ_{PS} and Γ_{PD} respectively. The sideband cooling laser is detuned from the $^2S_{1/2}$ – $^2D_{5/2}$ transition by δ_{SD} and quencher laser detuned from the $^2P_{3/2}$ – $^2D_{5/2}$ transition by δ_{PD}. The quencher laser has a coupling strength of Ω_{PD} with the $^2P_{3/2}$ – $^2D_{5/2}$ transition. In the limit that the saturation parameter

$$s_{PD} = \frac{\Omega_{PD}^2/2}{\delta_{PD}^2 + (\Gamma_{PS}^2 + \Gamma_{PD}^2)/4} \tag{9.1}$$

for the $^2P_{3/2}$ – $^2D_{5/2}$ transition is small ($S_{PD} \ll 1$) and $|\delta_{SD}| \ll \Gamma_{PS} + \Gamma_{PD}$ the $^2P_{3/2}$ state is hardly occupied and may be adiabatically eliminated to give the effective decay rate of the $^2D_{5/2}$ state [145]

$$\Gamma' = \frac{s_{PD}}{2}\Gamma_{PD}. \tag{9.2}$$

The cooling rate is then given by the product of the decay rate of the excited level and its occupation probability [31],

$$R = \Gamma' \frac{\eta\sqrt{n}\Omega_0}{2(\eta\sqrt{n}\Omega_0)^2 + \Gamma'^2}. \tag{9.3}$$

where $\eta\sqrt{n}\Omega_0$ is the laser-ion coupling strength on the red sideband given by equation 2.26.

From equations 9.2 and 9.3, it is clear that the cooling rate is dependent on both the saturation parameter of the laser on the quencher transition and the ion's vibrational quantum number. It follows that the optimum $^2D_{5/2}$

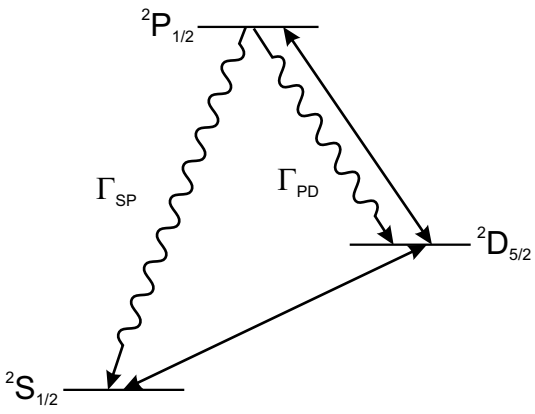

Figure 9.2: Three level 'cascade' system of $^{88}Sr^+$

state effective decay rate of

$$\Gamma'_{opt} = \sqrt{2} \times (\eta\sqrt{n}\Omega_0) \tag{9.4}$$

yields the highest cooling rate

$$R_{max} = \frac{\Gamma'_{opt}}{4} = \frac{\eta\sqrt{n}\Omega_0}{2\sqrt{2}} \tag{9.5}$$

for an ion with vibrational quantum number n.

9.2.2 Sideband cooling scheme for $^{88}Sr^+$

A good approximation to the three-level atom of section 9.2.1 may be realised by using an identical sideband cooling scheme to that employed in work using $^{40}Ca^+$ [33]. In this scheme, a magnetic field is applied to split the Zeeman components of the quadrupole transition and the ion is optically pumped into

the $^2S_{1/2}$ ($m_j = -1/2$) state. The ion is then sideband cooled on the lower motional sideband of the $^2S_{1/2}$ ($m_j = -1/2$) – $^2D_{5/2}$ ($m_j = -5/2$) transition. A quencher laser is used shorten the lifetime of the $^2D_{5/2}$ state. Due to the $\Delta m = 0, \pm 1$ selection rule for dipole transitions, the quencher laser couples the $^2D_{5/2}$ ($m_j = -5/2$) state only to the $^2P_{3/2}$ ($m_j = -3/2$) state. This state then decays with a high branching ratio (16:1) back to the $^2S_{1/2}$ ($m_j = -1/2$) state. Thus a number of cooling steps may be completed before the ion is lost from the cooling cycle. The $^2S_{1/2}$ ($m_j = -1/2$) $\rightarrow$ $^2D_{5/2}$ ($m_j = -5/2$) $\rightarrow$ $^2P_{3/2}$ ($m_j = -3/2$) $\rightarrow$ $^2S_{1/2}$ ($m_j = -1/2$) cooling cycle is shown in figure 9.3.

While the $^2S_{1/2}$ ($m_j = -1/2$) $\rightarrow$ $^2D_{5/2}$ ($m_j = -5/2$) $\rightarrow$ $^2P_{3/2}$ ($m_j = -3/2$) $\rightarrow$ $^2S_{1/2}$ ($m_j = -1/2$) cooling cycle at first glance seems equally well suited for sideband cooling, it is not used for the following reason. The $^2S_{1/2}$ ($m_j = +1/2$) – $^2D_{5/2}$ ($m_j = +5/2$) is the highest frequency Zeeman component, which means that its lower motional sidebands may accidentally coincide with upper motional sidebands of other Zeeman transition. Since the $^2S_{1/2}$ ($m_j = -1/2$) – $^2D_{5/2}$ ($m_j = -5/2$) component is the lowest frequency Zeeman component, such an occurrence is impossible.

9.2.3 Sideband cooling rate in $^{88}Sr^+$

It is instructive to consider how the simple model of equations 9.2 and 9.3 influence the choice of laser parameters when sideband cooling $^{88}Sr^+$.

The coupling strength Ω_0 on the $^2S_{1/2}$ ($m_j = -1/2$) – $^2D_{5/2}$ ($m_j = -5/2$)

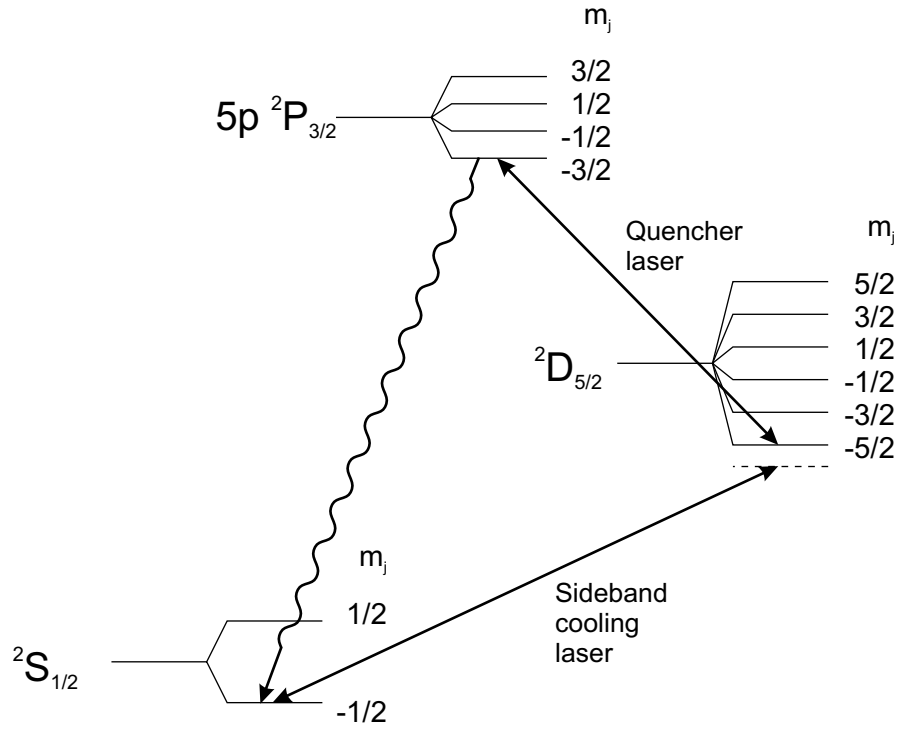

Figure 9.3: Resolved sideband cooling cycle. The ion is sideband cooled on the lower motional sideband of the $^2\mathrm{S}_{1/2}$ ($m_j = -1/2$) – $^2\mathrm{D}_{5/2}$ ($m_j = -5/2$) transition. The quencher laser couples the $^2\mathrm{D}_{5/2}$ ($m_j = -5/2$) to the $^2\mathrm{P}_{3/2}$ ($m_j = -3/2$) state which quickly decays back to the $^2\mathrm{S}_{1/2}$ ($m_j = -1/2$) ground state forming a closed cooling cycle.

transition is given by [83]

$$\Omega_0 = \frac{e|\mathbf{E}|}{\hbar}\sqrt{\frac{5A_{SD}}{8|\mathbf{k}|^3 c\alpha}}g(\mathbf{k},\mathbf{E}) \tag{9.6}$$

where $\mathbf{E}$ and $\mathbf{k}$ are the electric field vector and wave-vector of the sideband cooling laser, A_{SD} is the spontaneous decay rate, α is the fine structure constant. The factor $g(\mathbf{k},\mathbf{E})$ accounts for the experimental geometry of the laser polarisation and direction. For the case in this work (see chapter 3) that the sideband is driven by vertically polarised light at an angle of 30° to the magnetic field, it is found that $g(\mathbf{k},\mathbf{E}) = 0.177$. Using an incident power of 1.4 mW in a 30 μm diameter beam waist gives the electric field strength $|\mathbf{E}| = 2.73 \times 10^5\ Vm^{-1}$ at the centre of the Gaussian beam. The coupling on the $^2\mathrm{S}_{1/2}$ ($m_j = -1/2$) – $^2\mathrm{D}_{5/2}$ ($m_j = -5/2$) carrier transition is therefore $\Omega_0/2\pi = 35$ kHz. For this sideband cooling beam geometry and a typical (axial) secular frequency of 3.8 MHz, the Lamb-Dicke parameter is calculated from equation 2.22 to be $\eta = 0.018$.

Now, using equations 9.2 and 9.3, it is possible to calculate the sideband cooling rate as a function of both n and s_{PD} (see figure 9.4). This calculation illustrates that as the ion is cooled, the saturation parameter required to maximise the sideband cooling rate is also reduced. This highlights the necessity of having a well Doppler cooled atom for as a prerequisite the successful implementation of sideband cooling. Numerically solving equation 9.3 for cooling on the axial mode ($\omega_z/2\pi$ =3.8 MHz) for an ion initially in the $n = 10$ motional state and an effective decay rate Γ' chosen to maximise the sideband cooling rate for $n = 10$, shows that the ion may be cooled to 99.9%

ground state occupation within 10 ms (see figure 9.5).

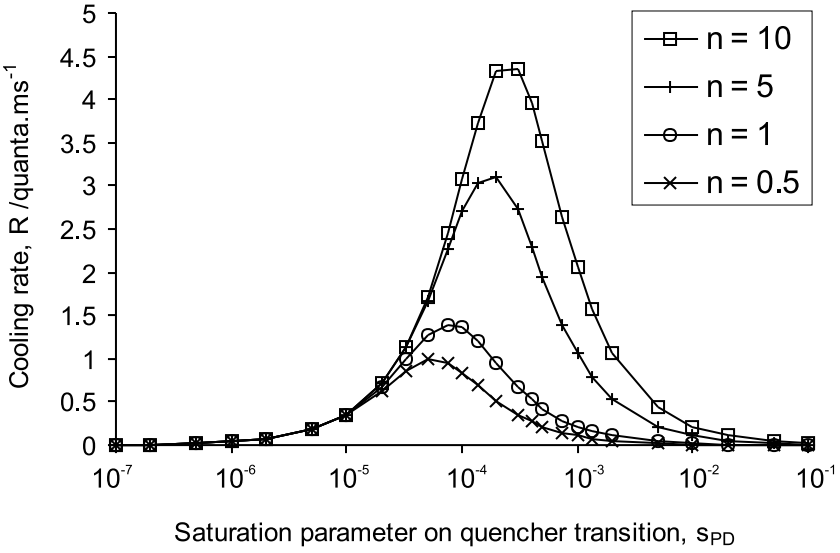

Figure 9.4: Resolved sideband cooling rate as a function of s_{PD} the saturation parameter on the quencher transition for an ion with vibrational quantum number $n = 0.5$, 1, 5 and 10.

Discrepancies between this simple model and attainable cooling rates may arise from the fact that this model does not consider heating due to collisions, ambient electrical noise, etc. or off-resonant heating mechanisms (for instance, off-resonant driving of the carrier or blue sideband), or the saturation of the red sideband by the cooling beam. It is these sources of heating which limit the final harmonic oscillator level achievable.

9.2.4 Motional state determination

While the mean motional state, $\bar{n}$ of the ion may be determined from the apparent damping of coherent oscillations (see chapter 6), the simplest and

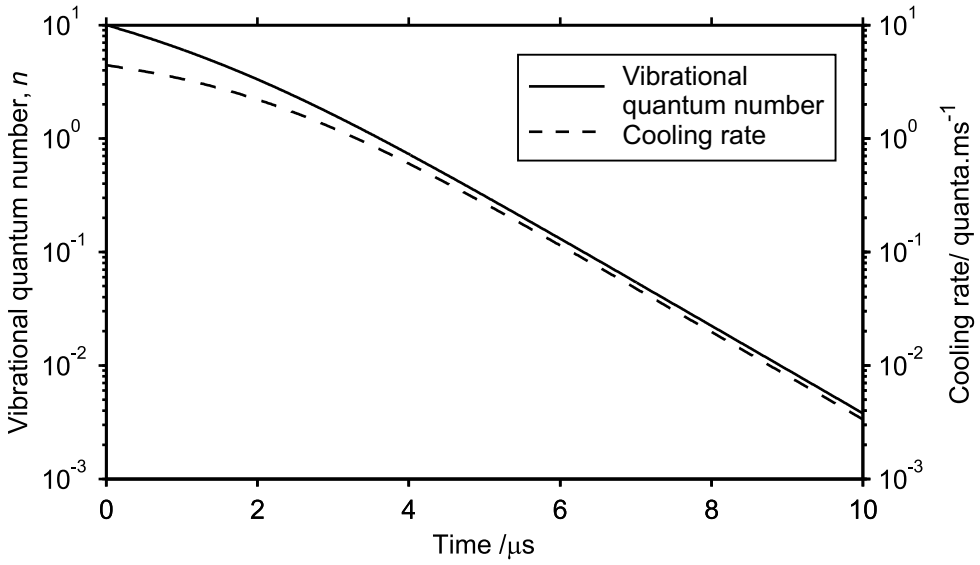

Figure 9.5: Calculated time evolution of vibrational quantum number and sideband cooling rate of an ion with initial vibrational quantum number $n = 10$ with quencher transition saturation parameter optimised for $n = 10$.

most robust method for determining $\bar{n}$ for low vibrational quantum numbers is to compare the excitation probability on the red and blue sidebands [32]. If it is assumed that the ion is prepared in a thermal distribution after sideband cooling and that decoherence may be neglected, from equations 2.28 and 2.28, it may be seen that the excitation probability on the blue sideband for an interrogation pulse of duration t is

$$P_{bsb} = \sum_{n=0}^{\infty} \frac{1}{2} \frac{\bar{n}^n}{(1+\bar{n})^{n+1}} \cos^2(\Omega_{n,n+1} t). \tag{9.7}$$

Similarly, the excitation on the red sideband is,

$$P_{rsb} = \sum_{n=1}^{\infty} \frac{1}{2} \frac{\bar{n}^n}{(1+\bar{n})^{1+n}} \cos^2(\Omega_{n,n-1} t) \tag{9.8}$$

which may be written as

$$P_{rsb} = \sum_{n=0}^{\infty} \frac{1}{2} \frac{\bar{n}^{n+1}}{(1+\bar{n})^{n+2}} \cos^2(\Omega_{n+1,n} t) \tag{9.9}$$

$$= \frac{\bar{n}}{1+\bar{n}} P_{bsb} \tag{9.10}$$

since, from equation 2.23, $\Omega_{n+1,n} = \Omega_{n,n+1}$. This means that the ratio of absorption probabilities is simply

$$R = \frac{P_{rsb}}{P_{bsb}} = \frac{\bar{n}}{1+\bar{n}} \tag{9.11}$$

and the mean vibrational quantum number of the thermal state is

$$\bar{n} = \frac{R}{1+R} \tag{9.12}$$

independent of the pulse duration t used. It should be noted that if the ion does not have a substantial ground state occupation probability, the asymmetry in excitation probability on the sidebands will be small and the measured mean vibrational quantum number will have a large uncertainty.

9.3 Sideband cooling of the axial mode

9.3.1 Motional sideband spectra

For resolved sideband cooling, it is necessary to resolve the $^2S_{1/2}$ ($m_j = -1/2$) – $^2D_{5/2}$ ($m_j = -5/2$) carrier and sideband transitions from those of the other Zeeman components of the quadrupole transition originating from

the $^2S_{1/2}$ ($m_j = -1/2$) state. This is achieved by applying a magnetic bias field of 3.4 G to the ion. Spectra of carrier and lower axial and radial motional sidebands of this transition obtained using the intense probe beam at a power of 1.38 mW are shown in figure 9.6. It was possible to resolve the two lower radial sidebands, which were split by 60 kHz.

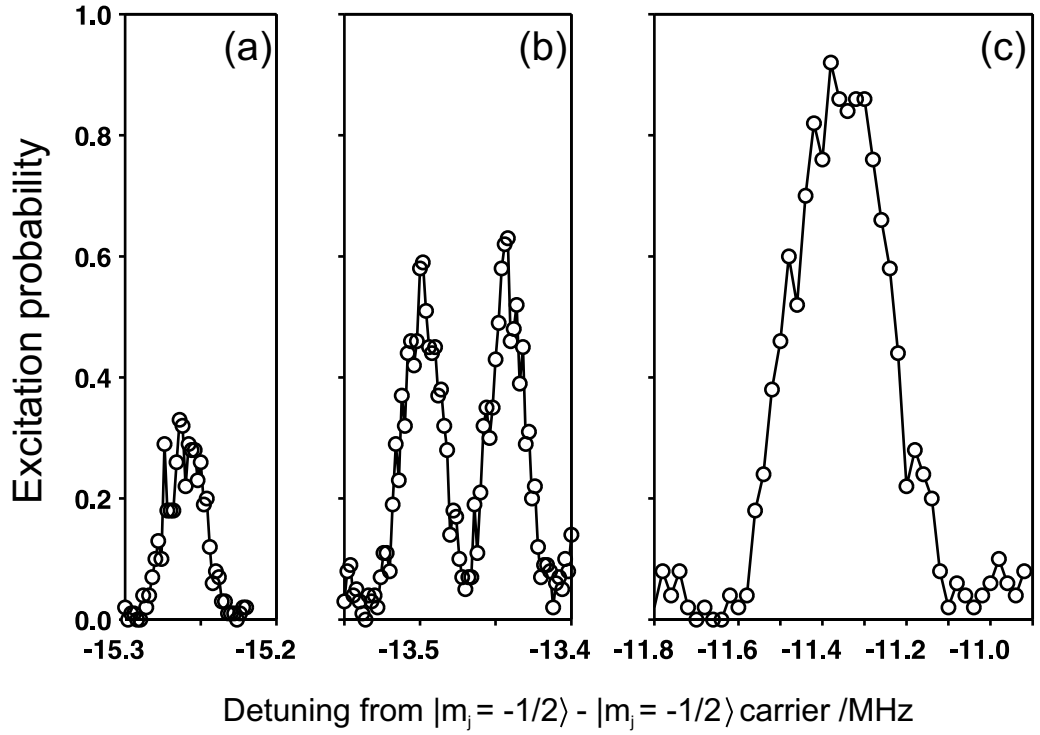

Figure 9.6: Spectra of the (a) lower axial sideband, (b) lower radial sidebands and (c) carrier component of the $^2S_{1/2}$ ($m_j = -1/2$) – $^2D_{5/2}$ ($m_j = -5/2$) transition. Spectra were obtained using the intense probe beam at a power of 1.38 mW. The data shown in (a) and (b) were obtained using 100 interrogations per point and an interrogation pulse duration of 30 μs, while 50 interrogations per point and an interrogation pulse duration of 3 μs were used in (c).

While the asymmetry in the upper and lower sidebands of this transition may be used to determine the motional state, the sidebands of the $^2S_{1/2}$

$(m_j = -1/2)$ – $^2D_{5/2}$ $(m_j = -1/2)$ transition are preferred. This is due to the fact that the geometrical factor $g(\mathbf{k}, \mathbf{E})$ [83] is 2.45 times larger for the latter transition in the experimental setup of this work. The carrier and motional sidebands are shown in figure 9.7. These spectra where obtained using the weak probe laser at a power of 560 μW for the sidebands and a reduced power of 13 μW for the carrier to avoid saturation.

9.3.2 AC-Stark shift measurement

During the sideband cooling process, the intense probe laser is tuned to a lower motional sideband and the quencher laser used to reduce the lifetime of the $^2D_{5/2}$ state. The presence of the quencher radiation will lead to an AC-Stark shift in the $^2D_{5/2}$ state, and a shift in the frequency of the motional sidebands.

The AC-Stark shift was characterised by recording the quencher induced frequency shift of a motional sideband transition as the quencher laser frequency is varied. The centre frequency of the sideband is determined using the same method of pulsed spectroscopy as that described in section 4.6. The only difference in the experimental sequence used, is that quencher radiation is incident on the ion during the intense probe interrogation pulse. If the quencher light is present after the end of the intense probe interrogation pulse, it will return an ion shelved in the $^2D_{5/2}$ state back to the ground state. If this occurs before the detection period (see figure 4.6) when the ion's electronic state is determined using the electron shelving method, no signal would be detected, even if the atom had been excited to the $^2D_{5/2}$

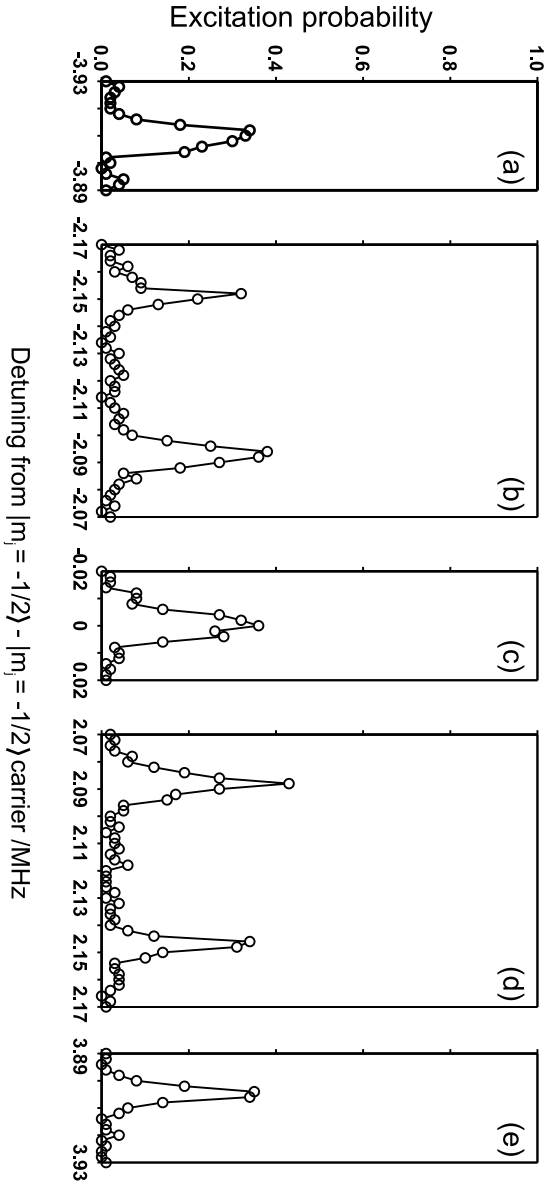

Figure 9.7: Spectra of the $^2S_{1/2}$ ($m_j = -1/2$) – $^2D_{5/2}$ ($m_j = -1/2$) transition's carrier and sidebands. Shown are (a) lower axial sideband, (b) lower radial sidebands and (c) carrier component, (d) upper radial sidebands and (e) upper axial sideband. Spectra were obtained using the weak probe beam at a power of 560 μW, except in the case of the carrier component in (c) when a reduced power of 13 μW was used to avoid saturation.

state. To avoid this, the quencher radiation was switched off at the same time as the interrogation pulse.

The centre frequency of one of the lower radial sidebands was measured as the quencher laser was scanned across the $^2D_{5/2}$ –$^2P_{3/2}$ transition. When the laser was far detuned a large excitation probably was observed. However, as the quencher detuning was reduced, the number of interrogations which resulted in the excitation of the ion to the $^2D_{5/2}$ state fell.

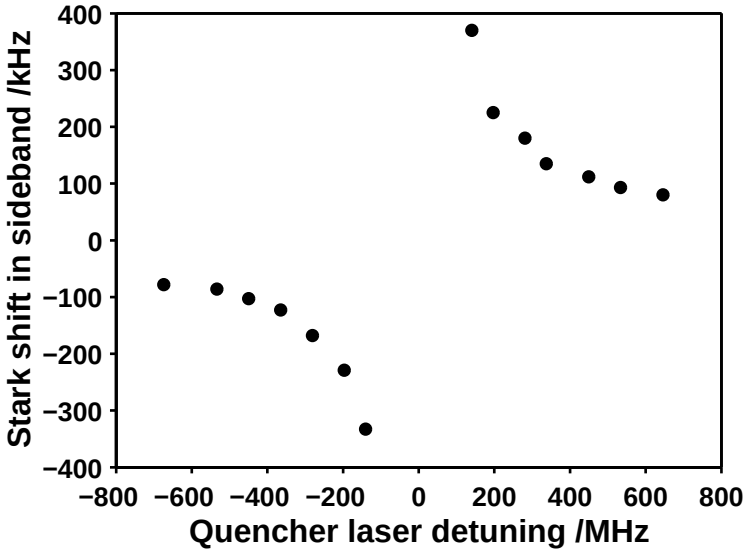

Figure 9.8: AC-Stark shift of lower radial sideband of the $^2S_{1/2}$ ($m_j = -1/2$) – $^2D_{5/2}$ ($m_j = -5/2$) transition when using a quencher beam power of 30 μW.

9.3.3 Cooling of the axial mode of motion

For sideband cooling, the standard experimental sequence described in section 4.6 was preceded by a sideband cooling step as shown in figure 9.9. The ion is first optically pumped into the $^2S_{1/2}$ ($m_j = -1/2$) state. The ion is

then subjected to a sideband cooling pulse of radiation on the lower axial sideband of the $^2S_{1/2}$ ($m_j = -1/2$) –$^2D_{5/2}$ ($m_j = -5/2$) transition. The quencher laser is also incident on this time and is present for a further 200 μs after the end of the sideband cooling pulse. This is to ensure that the ion is returned to the $^2S_{1/2}$ state after sideband cooling. The ion is then interrogated on the $^2S_{1/2}$ ($m_j = -1/2$) –$^2D_{5/2}$ ($m_j = -1/2$) upper and lower axial sidebands to determine its motional state.

A 3.4 G bias field was applied to resolve the lower axial sideband of the $^2S_{1/2}$ ($m_j = -1/2$) – $^2D_{5/2}$ ($m_j = -5/2$) transition used for sideband cooling and the upper and lower axial sidebands of the $^2S_{1/2}$ ($m_j = -1/2$) – $^2D_{5/2}$ ($m_j = -1/2$) used for subsequent motional state determination, from all other transitions. These sidebands will be referred to as the cooling sideband and the detection sidebands respectively.

For sideband cooling, a quencher power of 70 μW was used, and the quencher laser was detuned between 400 and 600 MHz below the $^2D_{5/2}$ – $^2P_{3/2}$ transition. Initially, the sideband cooling experimental sequence was repeated as the intense probe sideband cooling laser was scanned across the frequency interval in which the cooling sideband was expected to be Stark shifted. During this experimental sequence, the weak probe laser frequency was tuned to line centre of the lower axial sideband. By minimising the excitation probability on the lower detection sideband, the sideband cooling rate was optimised. With a sideband cooling pulse of 5 ms duration at a power of 1.38 mW, the optimal quencher laser detuning was found to be $\sim$530 MHz and the cooling sideband Stark shift was -730 kHz.

The absorption spectra of the detection sidebands after sideband cooling

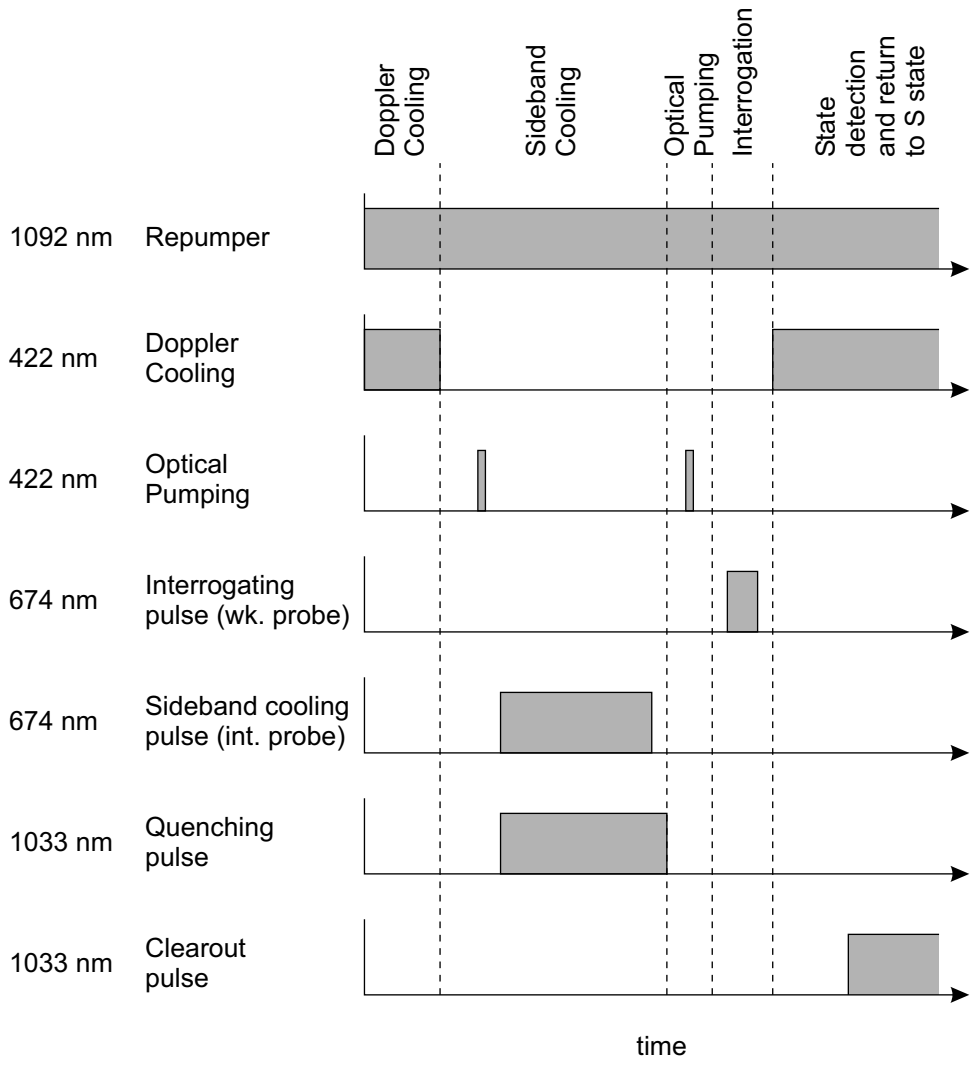

Figure 9.9: Experimental pulse sequence used for sideband cooling.

were obtained using the weak probe laser (see figure 9.10). Also shown are the spectra, when the intense probe beam is blocked, and there is no sideband cooling. These spectra are the result of 200 interrogations per data point at intervals of 1 kHz. The weak probe beam power was 560 μW and interrogation pulse duration was 400 μs.

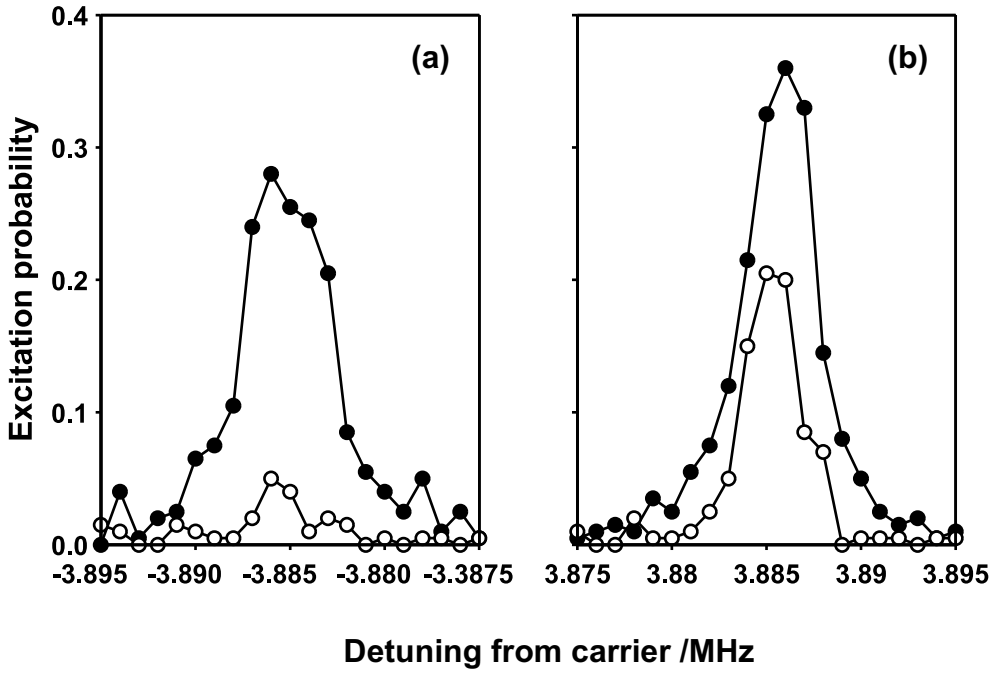

Figure 9.10: Absorption spectra on both upper (b) and lower (a) axial sidebands of the $^2S_{1/2}$ ($m_j = -1/2$) – $^2D_{5/2}$ ($m_j = -1/2$) transition, before (open circles) and after (filled circles) resolved sideband cooling. A mean axial vibrational quantum number after sideband cooling of $\bar{n}_z = 0.3 \pm 0.1$ is inferred from the asymmetry in excitation probabilities on the sidebands.

The asymmetry in the excitation probabilities on the upper and lower sideband indicates that the ion has been sideband cooled to a mean axial motional quantum number of $\bar{n}_z = 0.3 \pm 0.1$. This should be contrasted with the mean axial motional quantum number of $\bar{n}_z = 8$ after Doppler cooling

found in section 2.5. From equation 2.28, it may be seen that $\bar{n}_z = 0.3 \pm 0.1$ is equivalent to a ground state occupation probability of $(77 \pm 6)\%$.

The measured value $\bar{n} = 0.3$ is in good agreement with the value of $n = 0.15$ predicted by the simple model of sections 9.2.1 and 9.2.3 for an ion initially in the pure $n = 8$ motional state and sideband cooled using a 5 ms pulse (in this model the lasers are set to the detunings which produce the optimal cooling rate at $n = 8$).

9.4 Discussion

The mean axial vibrational quantum of $\bar{n}_z = 0.3 \pm 0.1$ is likely to be limited by short duration of the sideband cooling pulse used. However, it is still informative to compare the results of this initial demonstration of sideband cooling of $^{88}Sr^+$ with previous experiments in which ground state cooling has been achieved.

Ground state cooling was first demonstrated by Diedrich *et al.* [32] in 1989 by resolved sideband cooling a single trapped $^{199}Hg^+$ ion. The ion was cooled by driving the lower motional sidebands of the narrow $^2S_{1/2} - {}^2D_{5/2}$ quadrupole transition and the motional ground state was achieved 95% of the time in 2D. In order to achieve this ground state occupation probability, a typical sideband cooling pulse of 200–500 ms was used, far longer than the 5 ms pulse used in this work.

Roos *et al.* have also used resolved sideband cooling on the quadrupole transition in $^{40}Ca^+$. In fact the cooling scheme used in this demonstration of sideband cooling in $^{88}Sr^+$ is identical to that used in the $^{40}Ca^+$ work.

Roos *et al.* were able to cool a single $^{40}Ca^{+}$ ion to the ground state of its trapping potential with a probability of 99.9% on the axial mode (ω_z = 4.51 MHz). This result was achieved with a sideband cooling pulse duration of 6.4 ms and a power 1 mW in a 1 kHz bandwidth and 30 μm spot at the ion. These parameters are comparable to those used here in sideband cooling $^{88}Sr^{+}$ but result in a much higher ground state occupation probability. This may be explained by the more favourable beam and magnetic field geometry employed which results in a larger laser-ion coupling strength in the $^{40}Ca^{+}$ work.

Another demonstration of resolved sideband cooling on a weak optical transition is that of Peik *et al.* using the $5s^2\ ^1S_0$ – $5s5p\ ^3P_1$ intercombination line in $^{115}In^{+}$. This work differs from the other demonstrations of sideband cooling discussed so far in that the intercombination line has a linewidth of 360 kHz which is $\sim 10^5$ larger than the linewidths of the quadrupole transitions above. This allows for a high cooling rate without the need to reduce the lifetime of the upper state via coupling to a quickly decaying state. Indeed, in this work $^{115}In^{+}$ ions were sideband cooled directly by driving higher-order lower sidebands, without the need for a Doppler pre-cooling stage. While the motional sidebands were well resolved from the carrier, they were not well resolved from each other, allowing all three degrees of freedom to be cooled simultaneously. Using the technique of cooling simultaneously on both the first red sideband and also a higher order red sideband, Peik *et al.* report cooling all three motional modes to the ground state with an occupation probability of greater than 50%. This measurement was limited by the fact the sidebands were not resolved, making it difficult to measure

low temperatures from their strengths.

Cooling to the zero point of motion in 3D has also been achieved by Monroe *et al.* by sideband cooling of a $^{9}Be^{+}$ using stimulated Raman transitions ion [35]. In this experiment, the ion was cooled by driving the lower sidebands of the Raman transition between hyperfine levels. The ion was prepared in the ground state 98% of the time when cooled on one motional mode only, and 92% of the time when cooled on all three motional modes. This method is also particularly fast with the sideband cooling process taking $sim100\ \mu$s. An important difference to note between this work in $^{9}Be^{+}$, and the other experiments discussed here is the very low vibrational quantum numbers (as low as $(n_x, n_y, n_z) = (0.47, 0.30, 0.18)$) achieved after the Doppler precooling stage. This is due to the very high secular frequencies of the trap of 10 – 30 MHz. However, an anomalous heating rate of 1000 phonons/s was reported in this trap, which is almost 3 orders of magnitude large than heating rates in measured in the $^{199}Hg^{+}$ and $^{40}Ca^{+}$ work discussed above.

An ion may be also cooled to the ground state of the trap by laser cooling with electromagnetically induced transparency [146]. In this method, quantum interference in a driven Λ-shaped atomic system is used to suppress the carrier transition. The dipole transition may then be driven with absorption only occurring on the remaining 'lower sideband' transition. Ground state cooling of $^{40}Ca^{+}$ has been achieved using this technique with 90% probability when cooling a single motional mode, and 74% and 58% respectively in two modes cooled simultaneously [36].

The resolved sideband cooling technique demonstrated in this chapter has been used to prepare the ion in the ground state of the axial vibrational

mode with a probability of 77%. This ground state occupation probability is comparable with previously published work using ground state cooling schemes.

9.5 Summary and conclusion

This chapter has presented the first demonstration of resolved sideband cooling of a $^{88}Sr^{+}$ ion. The ion has been sideband cooled on the lower axial motional sideband of the $^{2}S_{1/2}$ ($m_j = -1/2$) – $^{2}D_{5/2}$ mj-5/2 component of the quadrupole transition. To realise an efficient cooling cycle, the $^{2}D_{5/2}$ state lifetime has been reduced by coupling it to the $^{2}P_{3/2}$ state using a quencher laser. Measurement of the asymmetry between upper and lower axial sidebands of the $^{2}S_{1/2}$ ($m_j = -1/2$) – $^{2}D_{5/2}$ mj-1/2 component of the quadrupole transition after sideband cooling have shown that the ion has been cooled to a mean axial vibrational quantum number $\bar{n}_z = 0.3 \pm 0.1$. This is equivalent to a ground state occupation probability of $(77 \pm 6)\%$.

Chapter 10

Conclusions and Outlook

10.1 Summary

This thesis has described a series of experiments performed using a single $^{88}Sr^{+}$ ion confined in an endcap trap. The aim of this work has been to gain an understanding of the experimental techniques required to perform studies of quantum information processing using trapped ions. A further long-term goal of this project is to investigate cavity QED effects on the quadrupole transition by placing a high finesse cavity around the ion.

Over the course of this work, a number of improvements have been made to the experimental apparatus from the initial setup [56]. This apparatus had a number of limitations, most notably, the trap suffered from an anomalous heating mechanism which meant that the ion was not well Doppler cooled. The trap was therefore unsuitable for coherent excitation studies and resolved sideband cooling experiments. The anomalous heating was thought to be casued by build up of impurites on the trap electrodes from the ^{88}Sr atomic

sources. Following similar observations in a $^{137}Ba^{+}$ microtrap, and the design of a new atomic ^{137}Ba source to alleviate this problem by DeVoe *et al.* [55], an analogous 'oven and hot plate' source for ^{88}Sr was constructed by A. G. Sinclair, based on the SrO + Ta reaction. It is believed that this will sputter fewer impurities on to the trap structure than the $SrAl_4$ + Ni system used previously.

A second slave laser at 674 nm was constructed to provide the high intensity required for coherent excitation excitation and sideband cooling on the quadrupole transtion. The medium term-stability of the probe laser system was limited by drifts in the offset of the master laser Pound-Drever-Hall error signal. This offset was the result of the large residual amplitude modulation caused by producing the Pound-Drever-Hall sidebands by modulating the master laser diode drive current. The residual amplitude modulation has since been reduced by generating the Pound-Drever-Hall sidebands using an electro-optic modulator instead. The long term stability of the probe laser has also been improved by employing an AC detection method in the first stage of the ULE reference cavity temperature control system.

In order to generate the ever more complex pulse sequences needed for the experiments described in this thesis, a new experimental control system has been been constructed and a control and data acquisition program written in LabVIEW. This has also allowed the use of the clearout laser to quickly return the ion to the ground state after the ion has been shelved in the $^2D_{5/2}$ state. Rather than being forced to wait $\sim$400 ms for the ion to decay, it is typically returned to the ground state within 5 ms. This has yielded a $\sim$ 10-fold increase in the number of interrogations which may be performed

in a given time when coherently driving the quadrupole transition.

As preliminary work towards investigations of cavity-QED with trapped ions, the lifetime of the 4d $^2D_{5/2}$ state has been measured using Dehmelt's electron shelving technique. A total of 160,000 shelved periods were observed, 63,000 in May 2000 and 97 in July 2002. Three different statistical methods have been used to analyse this data and a comparison of these methods has been made. Both systematic and statistical sources of error have been evaluated. This precision measurement yields a $^2D_{5/2}$ state lifetime of 390.3 ms, an order of magnitude more accurate than the previous best measurement [94, 79, 95, 86].

The $^2S_{1/2}$ ($m_j = -1/2$) – $^2D_{5/2}$ ($m_j = -1/2$) transition has been coherently driven in the Doppler cooled ion. Rabi oscillations with a decaying contrast have been observed on the carrier, and radial and axial sidebands of this transition. The apparent damping of the Rabi oscillations is caused the differing Rabi frequencies between the laser and each motional state. The contrast of Rabi oscillation observed on the sidebands is seen to decay in fewer oscillation periods than those observed on the carrier transition. This is due to the fact that the Rabi frequency of the laser coupled with a sideband transition have a stronger dependance on the ion's vibrational quantum number than that for the carrier transition.

Time-domain Ramsey spectroscopy of the $^2S_{1/2}$ ($m_j = -1/2$) – $^2D_{5/2}$ ($m_j = -1/2$) transition has been performed and Ramsey fringes with a contrast of up to $\sim 90\%$ have been observed. Due to the finite coherence time of the probe laser, the observed fringe contrast decreases as the period of free precession between the two Ramsey interrogation pulses is increased. Varying

the relative phase difference between the Ramsey interrogation pulses alters the excitation probability in a predictable manner. By varying the laser's relative phase, it will be possible to compensate for unwanted atomic phase shifts incurred when manipulating atomics states with coherent pulses (for instance in quantum information processing studies).

The two phase modulation techniques of Ramsey and Silsbee [127] have been demonstrated for the first time in the optical domain. A symmetric fringe pattern is observed when measuring the change in transition probability on introducing a 180° relative phase shift between Ramsey interrogation pulses. In contrast, an anti-symmetric fringe pattern is observed when measuring the change in transition probability on the reversal of a 90° relative phase shift. This second fringe pattern with its zero-crossing at line centre will make an ideal discriminant for stabilising a laser to a narrow atomic reference transition in an optical frequency standard.

The anti-symmetric Ramsey fringe pattern has been used as the frequency discriminant for stabilisation of the probe laser to the $^2\mathrm{S}_{1/2}$ ($m_j = -1/2$) – $^2\mathrm{D}_{5/2}$ ($m_j = -1/2$) transition. A proportional feedback loop was used.

Resolved sideband cooling has been demonstrated on the lower axial sideband of the $^2\mathrm{S}_{1/2}$ ($m_j = -1/2$) – $^2\mathrm{D}_{5/2}$ ($m_j = -5/2$) transition. The ion was cooled to a mean axial vibrational quantum number of $\bar{n}_z = 0.3 \pm 0.1$, equivalent to an axial harmonic oscillator ground state occupation probability of $(77 \pm 6)\%$.

10.2 Future Work

The first step towards quantum information processing using trapped ions is the complete control of the quantum state of a single trapped ion. Although, the ion's electronic state may already be manipulated with a high fidelity and the cooling of one motional mode to the ground state most of the time has been demonstrated, to achieve the desired level of control over both internal and external states of the ion, the following further work must be carried out.

Firstly, the sideband cooling process requires optimisation. An investigation of the time evolution of the ion's motional state during sideband cooling must be performed and the experimental cooling limit found. The cooling of a single motional mode to the ground state is a necessity for its use as a *qubit* for the demonstration of a quantum gate using a single ion [38]. However, while necessary this condition may not sufficent, and it may be that cooling of all three motional modes to the ground state is required in order to implement such a quantum gate [16]. Since the main practical difficulty in performing quantum infomation processing using trapped ions will be the intrinsic trap heating rate which will lead to decoherence of these fragile motional quantum states must be measured [33].

In the work demonstrated so far, coherent manipulations have been on the carrier transition and may be used to prepare the ion in an arbitrary internal electronic state without affecting the ion's external motional state. In order to coherently manipulate the ion's motional state, it will be necessary to coherently drive the sideband transitions in a ion cooled to the motional

ground state. The observation of high contrast Rabi oscillations on the motional sideband transitions is an important step towards demonstrating the potential of this experimental system for quantum information studies.

The coupling strength on the sideband transitions, is much smaller that that on the carrier (see equations 2.26 and 2.27). A higher spectral intensity of light at 674 nm would therefore be highly desirable. This may be achieved by reducing the probe laser linewidth still further. In practice this will require further isolation of the ULE reference cavity from the ambient noise of the laboratory. For instance mounting the reference cavity on a low spring contant platform and housing the cavity in a quiet-house will reduce the vibrational and accoustic noise. In addition to porviding a higher spectral intensity, reducing the linewidth will also increase the laser coherence time, alowing an increased period in which coherent operations may be performed.

Increasing the available absolute intensity at 674 nm is also desirable, as this will allow a greater sideband cooling rate to be realised. Work has already been performed by S.-K. Choi on an injection locked broad area laser diode system [147] capable of providing up to 60 mW of 674 nm light at the trap. For sideband cooling, the drift rate of the quencher laser also needs reducing. This may easily be achieved by improving the temparature stabbilisation of both the laser diode housing and the laser's reference cavity.

A major limitation to the work at present is the electron bombardment method used to ionise neutral strontium atoms to load the trap. Since the filaments are not directional, stray charges are deposited over the insulating surface of the trap structure causing large stray electric fields at the ion which must be compensated to reduce the its micromotion. A greater problem is

that this charge dissipates over a the course of a day, and the minimisation must therefore be repeatedly minimised over this time. This problem may be avoided by using the method of photoionisation as has been demonstrated recently in $^{40}Ca^{+}$ experiments [148, 149, 150]. It would appear that there are two viable methods of photoionisation for ^{88}Sr. The first is analogous to that used by Kjærgaard *et al.*and would require a 293 nm laser source, while the second is analogous to the method used by Gulde *et al.* [149] and more recently Lucas *et al.* [150] and would require sources at 461 nm and 405 nm.

Although the new ^{88}Sr source removes the possibility of impurities such as aluminium and nickel from being sputtered onto the trap electrodes, over time they will become coated with strontium. It is at the moment unknown wether this will lead to an increase in the trap's heating rate. This potential problem may also be avoided by using the photoionisation technique which, with its much higher efficiency, is able to load traps using 10^{-5} of the atomic flux needed for electron bomabardment loading. It is also important to note that the method of photoionisation allows isotepe selective deterministic loading of an ion trap, widely regarded as a key technology for pursuing quantum information studies using ion strings.

In the long term, it is hoped that this single ion trap will be used for investigations of cavity QED by placing a high finesse cavity around the trap within the vacuum chamber. It is also anticipated that quantum information processing studiess will require the construction of a linear ion trap for use with strings of trapped ions.

Bibliography

[1] S. Ghezali, Ph. Laurent, S. N. Lea, and A. Clairon. An experimental study of the spin-exchange frequency shift in a laser-cooled cesium fountain frequency standard. *Europhys. Lett.*, 36:25–30, 1996.

[2] S. Weyers, U. H ubner, R. Schr oder, Chr. Tamm, and A. Bauch. Uncertainty evaluation of the atomic caesium fountain csf1 of the ptb. *Metrologia*, 38:343–352, 2001.

[3] S. R. Jefferts, J. Shirley, T. E. Parker, T. P. Heavner, D. M. Meekhof, C. Nelson, F. Levi, G. Costanzo, A. De Marchi, R. Drullinger, L. Hollberg, W. D. Lee, and F. L. Walls. Accuracy evaluation of nist-f1. *Metrologia*, 39:321–336, 2002.

[4] K. Gibble and S. Chu. Laser-cooled Cs frequency standard and a measurement of the frequency shift due to ultracold collisions. *Phys. Rev. Lett.*, 70:1771–1774, 1993.

[5] R. J. Rafac, B. C. Young, J. A. Beall, W. M. Itano, D. J. Wineland, and J. C. Bergquist. Sub-dekahertz ultraviolet spectroscopy of $^{199}Hg^{+}$. *Phys. Rev. Lett.*, 85:2462–2465, 2000.

[6] J. E. Bernard, A. A. Madej, L. Marmet, B. G. Whitford, K. J. Siemsen, and S. Cundy. Cs-based frequency measurement of a single, trapped ion transition in the visible region of the spectrum. *Phys. Rev. Lett.*, 82(16):3228–3231, 1999.

[7] H. S. Margolis, G. Huang, G. P. Barwood, S. N. Lea, H. A. Klein, W. R. C. Rowley, P. Gill, and R. S. Windeler. Absolute frequency measurement of the 674-nm $^{88}Sr^{+}$ clock transition using a femtosecond optical frequency comb. *Phys. Rev. A*, 67:032501, 2003.

[8] Chr. Tamm, D. Engelke, and V. B uhner. Spectroscopy of the electric-quadrupole transition $^{2}S_{1/2}(f = 0)-^{2}D_{3/2}(f = 2)$ in trapped $^{171}Yb^{+}$. *Phys. Rev. A*, 61:053405, 2000.

[9] Th. Becker, J. von Zanthier, A. Yu. Nevsky, Ch. Schwedes, M. N. Skvortsov, H. Walther, and E. Peik. High-resolution spectroscopy of a single In^{+} ion: Progress towards an optical frequency standard. *Phys. Rev. A*, 63:051802(R), 2001.

[10] P. J. Blythe, S. A. Webster, H. S. Margolis, S. N. Lea, G. Huang, S. K. Choi, W. R. C. Rowley, P. Gill, and R. S. Windeler. Subkilohertz absolute-frequency measurement of the 467-nm electric octupole transition in $^{171}Yb^{+}$. *Phys. Rev. A*, 67:020501(R), 2003.

[11] P. Gill, G. P. Barwood, H. A. Klein, G. Huang, S. A. Webster, P. J. Blythe, K. Hosaka, S. N. Lea, and H. S. Margolis. Trapped ion frequency standards. *Meas. Sci. Technol.*, 14:1174–1186, 2003.

[12] P. W. Shor. Polynomial-time algorithms for prime factorization and discrete logarithms on a quantum computer. In *Proc. 35th Annual Symp. on Foundations of Computer Science*. IEEE Computer Society Press, 1994.

[13] L.K. Grover. Quantum mechanics helps in searching for a needle in a haystack. *Phys. Rev. Lett.*, 79:325–328, 1997.

[14] R. Feynman. Simulating physics with computers. *International Journal of Theoretical Physics*, 21:467–488, 1982.

[15] D. P. DiVincenzo. The physical implementation of quantum computation. *Fortschr. Phys.*, 48:771–783, 2000.

[16] J. I. Cirac and P. Zoller. Quantum computations with cold trapped ions. *Phys. Rev. Lett.*, 74(20):4091–4094, 1995.

[17] A. Sørenson and A Mølmer. Quantum computation with ions in thermal motion. *Phys. Rev. Lett.*, 82:1971–1974, 1999.

[18] J. I. Cirac and P Zoller. A scalable quantum computer with ions in an array ofmicrotraps. *Nature*, 404:579–581, 2000.

[19] D. Kielpinski, C. Monroe, and D. J. Wineland. Architecture for a large-scale ion-trap quantum computer. *Nature*, 417:709–711, 2002.

[20] G. K. Brennen, C. M. Caves, P. S. Jessen, and I. H. Deutsch. Quantum logic gates in optical lattices. *Phys. Rev. Lett.*, 82:1060–1063, 1999.

[21] D. Jaksch, H. J. Briegel, J. I. Cirac, C. W. Gardiner, and P. Zoller. Entanglement of atoms via cold controlled collisions. *Phys. Rev. Lett.*, 82:1975–1978, 1999.

[22] E. Knill, R. Laflamme, and G. J. Milburn. A scheme for efficient quantum computation with linear optics. *Nature*, 409:46–52, 2000.

[23] P. Domokos, J. M. Raimond, M. Brune, and S. Haroche. Simple cavity-QED two-bit universal quantum logic gate: the principle and expected performances. *Phys. Rev. A*, 52:3554–3560, 1995.

[24] N. A. Gershenfeld and I. L. Chuand. Bulk spin-resonance quantum computation. *Science*, 275:350–356, 1997.

[25] D. G. Cory and T. F. Fahmys, A. F and. Havel. Ensemble quantum computing by NMR spectroscopy. *Proc. Natl. Acad. Sci. USA*, 94:1634–1639, 1997.

[26] D. Loss and D. P. DiVincenzo. Quantum computation with quantum dots. *Phys. Rev. A*, 57:120–126, 1998.

[27] Y. Makhlin, G. Sch on, and A. Shnirman. Josephson-junction qubits with controlled couplings. *Nature*, 398:305–307, 1999.

[28] B. E. Kane. A silicon-based nuclear spin quantum computer. *Nature*, 393:133–137, 1998.

[29] A. Steane. Quantum computing. *Rep. Prog. Phys.*, 61:117–173, 1997.

[30] T. Sleator and H. Weinfurter. Realizable universal quantum logic gates. *Phys. Rev. Lett.*, 74:4087–4090, 1995.

[31] D. Leibfreid, R. Blatt, C. Monroe, and D. Wineland. Quantum dynamics of single trapped ions. *Rev. Mod. Phys.*, 75:281–323, 2003.

[32] F. Diedrich, J. C. Bergquist, W. M. Itano, and D. J. Wineland. Laser cooling to the zero point energy of motion. *Phys. Rev. Lett.*, 62:403–406, 1989.

[33] Ch. Roos, Th. Zeiger, H. Rohde, H. C. Nägerl, J. Eschner, D. Leibfried, F. Schmidt-Kaler, and R. Blatt. Quantum state engineering on an optical transition and decoherence in a Paul trap. *Phys. Rev. Lett.*, 83:4713–4716, 1999.

[34] E. Peik, J. Abel, Th. Becker, J. von Zanthier, and H. Walther. Sideband cooling of ions in radio-frequency traps. *Phys. Rev. A*, 60:439–449, 1999.

[35] C. Monroe, D. M. Meekhof, S. R. King, B. E.and Jefferts, W. M. Itano, Wineland. D. J., and P. Gould. Resolved-sideband Raman cooling of a bound atom to the 3D zero-point energy. *Phys. Rev. Lett.*, 75:4011–4014, 1995.

[36] C. F. Roos, D. Leibfried, A. Mundt, F. Schmidt-Kaler, J Eschner, and R. Blatt. Experimental demonstration of ground state laser cooling with electromagnetically induced transparency. *Phys. Rev. Lett.*, 85:5547–5550, 2000.

[37] D. M. Meekhof, C. Monroe, B. E. King, W. M. Itano, and D. J. Wineland. Generation of nonclassical motional states of a trapped atom. *Phys. Rev. Lett.*, 76:1796–1799, 1996.

[38] C. Monroe, D. M. Meekhof, B. E. King, W. M. Itano, and D. J. Wineland. Demonstration of a fundamental quantum logic gate. *Phys. Rev. Lett.*, 75:4714–4717, 1995.

[39] C. Monroe, D. M. Meekhof, B. E. King, and D. J. Wineland. A "Schrödinger cat" superposition state of an atom. *Science*, 272:1131–1136, 1996.

[40] S. Gulde, M Riebe, G. P. T. Lancaster, C. Becher, J. Eschner, H. H affner, F. Schmidt-Kaler, I. L. Chuang, and R. Blatt. Implementation of the Deutsch-Jozsa algorithm on an ion-trap quantum computer. *Nature*, 421:48–50, 2003.

[41] C. J. Myatt, B. E. King, Q. A. Turchette, C. A. Sackett, D. Kielpinski, W. M. Itano, C. Monroe, and D. J. Wineland. Decoherence of quantum superpositions through coupling to engineered reservoirs. *Nature*, 403:269–273, 2000.

[42] F. Schmidt-Kaler, C. Roos, H. C. N agerl, H. Rohde, S. Gulde, A. Mundt, M. Lederbauer, G. Thalhammer, T. Zeiger, P. Barton, L. Hornekaer, G. Reymond, D. Leibfried, J. Eschner, and R. Blatt. Ground state cooling, quantum state engineering and study of decoherence of ions in Paul traps. *J. Mod. Opt.*, 47:2573, 2000.

[43] H. Rohde, S. T. Gulde, C. F. Roos, P. A. Barton, D. Leibfried, J. Eschner, F. Schmidt-Kaler, and R. Blatt. Sympathetic ground-state cooling and coherent manipulation with two-ion crystals. *J. Opt. B*, 3:S34–S41, 2000.

[44] B. E. King, C. S. Wood, C. J. Myatt, Q. A. Turchette, D. Leibfried, W. M. Itano, C. Monroe, and D. J. Wineland. Cooling the collective motion of trapped ions to initialize a quantum register. *Phys. Rev. Lett.*, 81:1525–1528, 1998.

[45] F. Schmidt-Kaler, H. H affner, M Riebe, S. Gulde, G. P. T. Lancaster, T. Deuschle, C. Becher, C. F. Roos, J. Eschner, and R. Blatt. Realization of the Cirac-Zoller controlled-NOT quantum gate. *Nature*, 422:408–411, 2003.

[46] C. A. Sackett, D. Kielpinski, B. E. King, C. Langer, V. Meyer, C. J. Myatt, M. Rowe, Q. A. Turchette, W. M. Itano, D. J. Wineland, and C. Monroe. Experimental entanglement of four particles. *Nature*, 404:256–259, 2000.

[47] H. Dehmelt. Proposed $10^{14}\delta\nu < \nu$ laser fluorescence spectroscopy on Tl^+ mono-ion oscillator II (spontaneous quantum jumps). *Bull. Am. Phys. Soc.*, 20:60, 1975.

[48] T.J. Quinn. Practical realization of the definition of the metre, including recommended radiations of other optical frequency standards (2001). *Metrologia*, 40(2):103–111, 2003.

[49] C. E. Moore. *Atomic energy levels*, volume 2. National Bureau of Standards (US), 1952.

[50] A. Gallagher. Oscillator strengths of Ca II, Sr II, and Ba II. *Phys. Rev.*, 157:24–30, 1967.

[51] W Paul. Electromagnetic traps for charged and neutral particles. *Rev. Mod. Phys.*, 62:531–540, 1990.

[52] W. Paul and H. Steinwedel. Translated: 'Quadrupole mass filter'. *Z. Naturforsch*, A8:448, 1953.

[53] G. Janik, W. Nagourney, and H. Dehmelt. Doppler-free optical spectroscopy on the Ba^+ mono-ion oscillator. *J. Opt. Soc. Am. B*, 2(8):1251–1257, 1985.

[54] S.R. Jefferts, C. Monroe, E. W. Bell, and D.J. Wineland. A coaxial-resonator driven rf (Paul) ion trap for strong confinement. *Phys. Rev. A*, 51:3112–3116, 1995.

[55] R. G. DeVoe and C. Kurtsiefer. Experimental study of anomalous heating and trap instabilities in a microscopic ^{137}Ba ion trap. *Phys. Rev. A*, 65:063407, 2002.

[56] A. G. Sinclair, M. A. Wilson, and P. Gill. Improved three-dimensional control of a single strontium ion in an endcap trap. *Opt. Commun.*, 190:193–203, 2001.

[57] G. Zs. K. Horvath, R. C. Thompson, and P. L. Knight. Fundamental physics with trapped ions. *Contem. Phys.*, 38:25–48, 1997.

[58] R. Blatt, P. Gill, and R. C. Thompson. Current perspectives on the physics of trapped ions. *J. Mod. Opt.*, 39:193–220, 1992.

[59] R. Alheit, C. Hennig, R. Morgenstern, F. Vedel, and G. Werth. Observation of instabilities in a Paul trap with higher-order anharmonicities. *Appl. Phys. B.*, 61:227–283, 1995.

[60] R. Loudon. *The quantum theory of light*. Oxford Univeraity Press, 3rd edition, 2000.

[61] R. W. Boyd. *Nonlinear Optics*. Academic Press, 2nd edition, 2002.

[62] R. H. Dicke. The effect of collisions upon the Doppler width of spectral lines. *Phys. Rev.*, 89:472–473, 1953.

[63] D. J. Wineland, C. Monroe, W. M. Itano, D. Leibfried, B. E. King, and D. M. Meekhof. Experimental issues in coherent quantum-state manipulation of trapped atomic ions. *J. Res. Natl. Inst. Stand. Technol.*, 103:259–328, 1998.

[64] C. A. Blockley, D. F. Walls, and H. Risken. Quantum collapses and revivals in a quantised trap. *Europhys. Lett*, 17:509–514, 1992.

[65] G. B. Arfken and H. J. Weber. *Mathematical methods for physicists*. Academic Press, 4th edition, 1997.

[66] T. W. Hänsch and A. L. Schawlow. Cooling of gases by laser radiation. *Opt. Commun.*, 13:68–69, 1975.

[67] D. J. Wineland and H. Dehmelt. Proposed $10^{14}\delta\nu < \nu$ laser fluorescence spectroscopy on Tl^+ mono-ion oscillator III (side band cooling). *Bull. Am. Phys. Soc.*, 20:637, 1975.

[68] W. M. Itano and D. J. Wineland. Laser cooling of ions stored in harmonic and Penning traps. *Phys. Rev. A*, 25:35–54, 1982.

[69] R. Blatt, G. Lafyatis, W. D. Phillips, S. Stenholm, and D. J. Wineland. Cooling in traps. *Physica Scripta*, T22:216–223, 1988.

[70] C. A. Schrama, E. Peik, W. W. Smith, and H. Walther. Novel miniature ion traps. *Opt. Commun.*, 101:32–36, 1993.

[71] D. J. Berkeland, J. D. Miller, J. C. Bergquist, W. M. Itano, and D. J. Wineland. Minimization of ion micromotion in a paul trap. *J. Appl. Phys.*, 83(10):5025–5033, 1998.

[72] W. W. Macalpine and R. O. Schildknecht. Coaxial resonators with helical inner conductor. *Proc. IRE*, pages 2099–2105, 1959.

[73] R. W. P. Drever, J. L. Hall, F. V. Kowalski, J. Hough, G. M. Ford, A. J. Munley, and H. Ward. Laser phase and frequency stabilization using an optical resonator. *Appl. Phys. B*, 31:97, 1983.

[74] T. W. Hänsch and B. Couillaud. Laser frequency stabilization by polarization spectroscopy of a reflecting reference cavity. *Opt. Commun.*, 35(3):441–444, 1980.

[75] M. J. Snadden, R. B. M. Clarke, and E. Riis. Injection-locking technique for heterodyne optical phase locking of a diode laser. *Opt. Lett.*, 22(12):892–894, 1997.

[76] L. Hilico, D. Touahri, F. Nez, and A. Clairon. Narrow-line, low-amplitude noise semiconductor laser oscillator in the 780 nm range. *Rev. Sci. Instrum.*, 65(12):3628–3633, 1994.

[77] W. M. Itano. External-field shifts of the $^{199}hg^{+}$ optical frequency standard. *NIST Journal of Research*, 105:829–837, 2001.

[78] J. Höffges, H.W. Baldauf, W. Lange, and H. Walther. Heterodyne measurement of the resonance fluorescence of a single ion. *J. Mod. Opt.*, 44(10):1999–2010, 1997.

[79] A. A. Madej and J. D. Sankey. Single, trapped Sr^{+} atom: laser cooling and quantum jumps by means of the $4d^2D_{5/2}$–$5s^2S_{1/2}$ transition. *Opt. Lett.*, 15(11):634–636, 1990.

[80] G.P. Barwood, P. Gill, G. Huang, H. A. Klein, and W. R. C. Rowley. Sub-kHz "clock" transition linewidths in a cold trapped $^{88}Sr^{+}$ ion in low manetic fields using 1092-nm polarisation switching. *Opt. Commun.*, 151:50–55, 1998.

[81] G. K. Woodgate. *Elementary Atomic Structure*. Oxford University Press, Oxford, 2nd edition, 1992.

[82] D. J. Berkeland and M. G. Boshier. Destabilisation of dark states and optical spectroscopy in Zeeman-degenerate atomic systems. *Phys. Rev. A*, 65:033413, 2002.

[83] D. F. V. James. Quantum dynamics of cold trapped ions with application to quantum computation. *Appl. Phys. B*, 66:181–190, 1998.

[84] H. C. N agerl, C. Roos, D. Leibfried, H. Rohde, G. Thalhammer, J. Eschner, F. Schmidt-Kaler, and R. Blatt. Investigating a qubit candidate: Spectroscopy on the $s_{1/2}$ to $d_{5/2}$ transition of a trapped calcium ion in a linear Paul trap. *Phys. Rev. A*, 61:023405, 2000.

[85] W. Nagourney, J. Sandberg, and H. Dehmelt. Shelved optical electron amplifier: Observation of quantum jumps. *Phys. Rev. Lett.*, 56(26):2797–2799, 1986.

[86] E. Biémont, J. Lidberg, S. Mannervik, L.-O. Norlin, P. Royen, A. Schmitt, W. Shi, and X. Tordoir. Lifetimes of metastable states in Sr II. *Eur. Phys J. D*, 11:355–365, 2000.

[87] F. Schmidt-Kaler, S. Gulde, M. Riebe, T. Deuschle, A. Kreuter, G. Lancaster, C. Becher, J. Eschner, H. H:affner, and R. Blatt. The coherence of qubits based on single Ca^+ ions. *J. Phys. B: At. Mol. Opt. Phys.*, 36:623–636, 2003.

[88] A.B. Mundt, A. Kreuter, D. Becher, C. andLeibfried, F. Eschner, J.and Schmidt-Kaler, and R. Blatt. Coupling a single atomic quantum bit to a high finesse optical cavity. *Phys. Rev. Lett.*, 89:103001, 2002.

[89] C. J. Zeippen. M1 and E2 transition probablities between the $3p^6 4s$ $^2S_{1/2}$ and the $3p^6 3d$ $^2D_{3/2}$, $^2D_{5/2}$ levels in K-like elements with Z = 19 to 24. *Astron. Astrophys.*, 229:248–252, 1990.

[90] M. A. Bautista, T. R. Gull, K. Ishibashi, H. Hartman, and K. Davidson. Excitation of SrII lines in Eta Carinae. *Mon. Not. R. Astron. Soc.*, 331:875–879, 2002.

[91] B Warner. Atomic oscillator strengths—III Alkali-like spectra. *Mon. Not. R. astr. Soc.*, 139:115–128, 1968.

[92] C. Guet and W. R. Johnson. Relativistic many-body calculations of transition rates for Ca^+, Sr^+, and Ba^+. *Phys. Rev. A*, 44(3):1531–1535, 1991.

[93] M. Poirier. A semi-empirical model for computing radial matrix elements in one-electron atoms and ions. *Z. Phys. D*, 25:117–125, 1993.

[94] Ch. Gerz, Th. Hilberath, and G. Werth. Lifetime of the $4D_{3/2}$ and $4D_{5/2}$ metastable states in Sr II. *Z. Phys. D*, 5:97–99, 1987.

[95] G. P. Barwood, C. S. Edwards, P. Gill, H. A. Klein, and W. R. C. Rowley. Laser cooling and probing of a trapped strontium ion using all-solid-state lasers. In L. Bloomfield, T. Gallagher, and D. Larson, editors, *AIP Conference Proceedings of Eleventh International Conference on Laser Spectroscopy*, pages 35–37, 1993.

[96] W. H. Press, B. P. Flannery, S. A. Teukolsky, and W. T. Vetterling. *Numerical Recipes The Art of Scientific Computing*. Cambridge University Press, 1986.

[97] Y. Pawitan. *In all likelihood: statistical modelling and inference using likelihood*. Oxford University Press, 2001.

[98] National Instruments Corporation.

[99] P. A. Barton, C. J. S. Donald, D. M. Lucas, D. A. Stevens, A. M. Steane, and D. Stacey. Measurement of the lifetime of the 3d $^2D_{5/2}$ state in $^{40}Ca^+$. *Phys. Rev. A*, 62:032503, 2000.

[100] L. Reekie, R. J. Mears, S. B. Poole, and D. N. Payne. *J. Lightwave Technol.*, 4:956, 1986.

[101] A. A. Madej. private communication.

[102] G. P. Barwood. private communication.

[103] S. Mannervik. private communication.

[104] W. M. Itano, J. C. Bergquist, J. J. Bollinger, J. M. Gilligan, D. J. Heinzen, F. L. Moore, M. G. Raizen, and D. J. Wineland. Quantum projection noise: Population fluctuations in two-level systems. *Phys. Rev. Lett.*, 47:3554–3570, 1993.

[105] N. F. Ramsey. A molecular beam resonance method with separated oscillating fields. *Phys. Rev.*, 78:695–699, 1950.

[106] N. F. Ramsey. Experiments with separated oscillatory fields and hydrogen masers. *Rev. Mod. Phys.*, 62:541–552, 1990.

[107] L Essen and J.V.L. Parry. *Nature*, 176:380, 1955.

[108] M. A. Kasevich, E. Riis, S. Chu, and R. G. DeVoe. rf spectroscopy in an atomic fountain. *Phys. Rev. Lett.*, 63:612–615, 1989.

[109] C. Fertig and K. Gibble. Measurement and cancellation of the cold collision frequency shift in an ^{87}Rb fountain clock. *Phys. Rev. Lett.*, 85:1622–1625, 2000.

[110] J.C. Bergquist, S.A. Lee, and J.L. Hall. Saturated absorption with spatially separated laser fields: Observation of optical "Ramsey" fringes. *Phys. Rev. Lett.*, 38:159–162, 1977.

[111] M. M. Salour and C. Cohen-Tannoudji. Observation of Ramsey's interference fringes in the profile of Doppler-free two-photon resonances. *Phys. Rev. Lett.*, 38:757–760, 1977.

[112] F. Riehle, Th. Kisters, A. Witte, and J. Helmcke. Optical ramsey spectroscopy in a rotating: Sagnac effect in a matter-wave interferometer. *Phys. Rev. Lett.*, 67:177–180, 1991.

[113] C. W. Oates, E. A. Curtis, and L. Hollberg. *Opt. Lett.*, 25:1603, 2000.

[114] K. R. Vogel, S. A. Diddams, C. W. Oates, E. A. Curtis, R. J. Rafac, W. M. Itano, J. C. Bergquist, R. W. Fox, W. D. Lee, J. S. Wells, and L. Hollberg. *Opt. Lett.*, 26:102, 2001.

[115] J. Stenger, T. Binnewies, G. Wilpers, F. Riehle, H. R. Telle, J. K. Ranka, R. S. Windeler, and A. J. Stenz. Phase-coherent frequency measurement of the Ca intercombination line at 657 nm with a Kerr-lens mode-locked femtosecond laser. *Phys. Rev. A*, 63:021802(R), 2001.

[116] Th. Udem, S. A. Diddams, K. R. Vogel, C. W. Oates, E. A. Curtis, W. D. Lee, W. M. Itano, R. E. Drullinger, J. C. Bergquist, and L. Holl-

berg. Absolute frequency measurements of the hg^+ and ca optical clock transitions with a femtosecond laser. *Phys. Rev. Lett.*, 86(22):4996–4999, 2001.

[117] G. Wilpers, T. Binnewies, C. Degenhardt, U. Sterr, J. Helmke, and F. Riehle. Optical clock with ultracold neutral atoms. *Phys. Rev. Lett.*, 89:230801, 2002.

[118] L. Marmet and A. A. Madej. Optical Ramsey spectroscopy and coherent measurements of the clock transition in a single trapped Sr ion. *Can. J. Phys.*, 78:495–507, 2000.

[119] H. H affner, S. Gulde, M. Riebe, G. Lancaster, C. Becher, J. Eschner, F. Schmidt-Kaler, and R. Blatt. Precision measurement and compensation of optical stark shifts for an ion-trap quantum processor. *Phys. Rev. Lett.*, 90:143602, 2003.

[120] Ye. V. Baklanov, V. P. Chebotayev, and B. Ya. Dubetsky. *Appl. Phys.*, 11:201, 1976.

[121] A. Huber, B. Gross, M. Weitz, and T. W. H ansch. Two-photon optical Ramsey spectroscopy of the 1S–2S transition in atomic hydrogen. *Phys. Rev. A*, 58:R2631–R2634, 1998.

[122] Ch. J. Bordé. *Phys. Lett. A*, 140:10, 1989.

[123] H. Katori, T. Ido, Y. Isoya, and M. Kuwata-Gonokami. Magneto-optical trapping and cooling of strontium atoms down to the photon recoil temperature. *Phys. Rev. Lett.*, 82:1116–1119, 1999.

[124] T. Binnewies, G. Wilpers, U. Sterr, F. Riehle, J. Helmcke, T.E. Mehlstäubler, E.M. Rasel, and W. Ertmer. Doppler cooling and trapping on forbidden transitions. *Phys. Rev. Lett.*, 87:123002, 2001.

[125] E.A. Curtis, C.W. Oates, and L. Hollberg. *J. Opt. Soc. Am. B.*, 20:977, 2003.

[126] T. Ido and H. Katori. Recoil-free spectroscopy of neutral Sr atoms in the Lamb-Dicke regime. *Phys. Rev. Lett.*, 91:053001, 2003.

[127] N. F. Ramsey and H. B. Silsbee. Phase shifts in the molecular beam method of separated oscillating fields. *Phys. Rev.*, 84:506–507, 1951.

[128] M. J. Ehrlich, L. C. Philips, and J. W. Wagner. Voltage-controlled acousto-optic phase shifter. *Rev. Sci. Instrum.*, 59:2390, 1988.

[129] G. Santarelli, P. Laurent, P. Lemonde, A. Clairon, A.G. Mann, S. Chang, A.N. Luiten, and C. Salamon. Quantum projection noise in an atomic fountain: A high stability cesium frequency standard. *Phys. Rev. Lett.*, 82:4619–4622, 1999.

[130] D. Cho, K. Sangster, and E.A. Hinds. Tenfold improvement on limits on T violation in thalium fluoride. *Phys. Rev. Lett.*, 63:2559–2562, 1989.

[131] J. Stenger, C. Tamm, N. Haverkamp, S. Weyers, and H. Telle. Absolute frequency measurement of the 435.5-nm $^{171}Yb^{+}$-clock transition with a Kerr-lens mode-locked femtosecond laser. *Opt. Lett.*, 26:1589–1591, 2001.

[132] J. von Zanthier, T. Becker, M. Eichenseer, A. Y. Nevsky, C. Schwedes, E. Peik, H. Walther, R. Holzwarth, J. Reichert, Th. Udem, T. W. Hnsch, P. V. Pokasov, M. N. Skvortsov, and S. N. Bagayev. *Opt. Lett.*, 25:1729, 2000.

[133] E. Riis and A. G. Sinclair. private communication.

[134] E. T. Jaynes and F. W. Cummings. Comparison of quantum and semiclassical radiation theories with application to the beam maser. *Proc. IEEE*, 51:89–109, 1963.

[135] J. I. Cirac, A. S. Parkins, R. Blatt, and P. Zoller. "dark" squeezed states of motion of a trapped ion. *Phys. Rev. Lett.*, 70:556–559, 1993.

[136] J. I. Cirac, R. Blatt, A. S. Parkins, and P. Zoller. Preparation of foch states by observation of quantum jumps in an ion trap. *Phys. Rev. Lett.*, 70:762–765, 1993.

[137] H. Zeng and F. Lin. Nonclassical vibrational states in a quantized trap. *Phys. Rev. A*, 48:1393–2397, 1993.

[138] B. Einstein, A.and Podolsky and N. Rosen. Squeezed atomic states and projection noise in spectroscopy. *Phy. Rev.*, 47:777–780, 1935.

[139] D. M. Greenberger, M. A. Horne, and A. Zeilinger. *Physics Today*, 46:22, 1993.

[140] D. J. Wineland, J. J. Bollinger, W. M. Itano, and D. J. Heinzen. Squeezed atomic states and projection noise in spectroscopy. *Phys. Rev. A*, 50:67–88, 1994.

[141] J. J . Bollinger, W. M. Itano, D. J. Wineland, and D. J. Heinzen. Optimal frequency measurements with maximally correlated states. *Phys. Rev. A*, 54:R4649–R4652, 1996.

[142] D. Leibfried, B. DeMarco, V. Meyer, D. Lucas, M. Barrett, J. Britton, W. M. Itano, B. Jelenkovic, C. Langer, T. Rosenband, and D. J. Wineland. Experimental demonstration of a robust, high-fidelity geometric two ion-qubit phase gate. *Nature*, 422:412–414, 2003.

[143] D. J. Wineland and W. M. Itano. Laser cooling of atoms. *Phys. Rev. A*, 20(4):1521–1540, 1979.

[144] D. J. Wineland, W. M. Itano, J. C. Bergquist, and R. G. Hulet. Laser-cooling limits and single ion spectroscopy. *Phys. Rev. A*, 36:2220–2232, 1987.

[145] J. I. Marzoli, I. Cirac, R. Blatt, and P. Zoller. Laser cooling of trapped three-level ions: Designing two-level systems for sideband cooling. *Phys. Rev. A*, 49:2771–2779, 1994.

[146] G. Morigi, J. Eschner, and C. H. Keitel. Ground state laser cooling using electromagnetically induced transparency. *Phys. Rev. Lett.*, 85:4458–4461, 2000.

[147] M. Praeger, V. Vuletic, T. Fischer, T. W. H ansch, and C. Zimmermann. A broad emitter diode laser system for lithium spectroscopy. *Appl. Phys. B*, 67:163–166, 1998.

[148] N. N. Kjærgaard, L. Hornekær, A. M. Thommesen, Z. Videsen, and M. Drewsen. Isotope selective loading of an ion trap using resonance-enhanced two-photon ionization. *Appl. Phys. B*, 71:207–210, 2001.

[149] S. Gulde, D. Rotter, P. Barton, F. Schmidt-Kaler, R. Blatt, and W. Hogervorst. Simple and efficient photo-ionization loading of ions for precision ion-trapping experiments. *Appl. Phys. B*, 73:861–863, 2001.

[150] D. M. Lucas, A. Ramos, J. P. Home, M. J. McDonnell, S. Nakayama, J.-P. Stacey, S. C. Webster, D. N. Stacey, and A. M. Steane. Isotope-selective photoionization for calcium ion trapping. *Phys. Rev. A*, 69:012711, 2004.